IMPROVING UNCONVENTIONAL RESERVOIR CHARACTERIZATION AND SIMULATION USING CONTROLLED-SOURCE ELECTROMAGNETIC METHODS

A Dissertation

by

MARCUS SCOTT ELLIOTT

Submitted to the Graduate and Professional School of
Texas A&M University
in partial fulfillment of the requirements for the degree of

DOCTOR OF PHILOSOPHY

Chair of Committee,	John E. Killough
Committee Members,	Mark Everett
	Eduardo Gildin
	Hadi Nasrabadi
Head of Department,	Akhil Datta-Gupta

August 2023

Major Subject: Petroleum Engineering

ABSTRACT

Controlled-source electromagnetic (CSEM) methods are inexpensive geophysical techniques that can be combined with petrophysical and petroleum engineering methods to improve our understanding of subsurface formation characterization and fluid monitoring. This dissertation investigates two forms of CSEM methods, electromagnetic (EM) induction logging and terrestrial CSEM, and their applications to petroleum engineering. Induction logging is a standard formation evaluation tool for characterization of electrical properties in the near-wellbore region. Terrestrial CSEM methods are better suited for far-field diagnostics away from a wellbore and have been established for a range of industry applications including CO_2 storage, geothermal exploration, terrestrial hydrocarbon exploration, buried pipeline, and hydraulic fracturing fluid flowback. In these applications, the EM response of a conductive wellbore casing must be accurately modeled and included in response simulations.

This dissertation (a) provided a new approach for combining EM induction logging (via anomalous diffusion simulation) with nuclear magnetic resonance (NMR) fracture-pore diffusional coupling to improve micro-fracture density estimation; (b) developed a method for assisting hydraulic fracture placement for natural fracture corridor geologic targeting; (c) simulated induction log response effects for hydraulic and natural fracture interactions; (d) developed a 2-D integral equation (IE) forward modeling code for simulating the EM response of conductive wellbore casing; and (e)

described an approach for modeling the EM response of conductive wellbore casing using a newly developed hybrid finite-element integral (FE-IE) equation method.

The methods used in this research include numerical NMR fracture-pore diffusional coupling simulation in multiple-porosity systems, 3-D FE numerical simulation of EM induction logging (via anomalous diffusion simulation), 2-D IE simulation of the EM response of conductive wellbore casing, and hybrid IE-FE simulation of the EM response for idealized fluid-bearing zones in an oil-field scenario. Results show that combining simulated EM anomalous diffusion with NMR can aid in distinguishing between micro-fracture fracture dimensions and density to improve fractured zone characterization, simulated EM anomalous diffusion may improve well production through better geologic targeting for natural fracture corridor depletion, and the hybrid IE-FE method improves FE solution stability while greatly reducing FE computation time by removing the need for an ultra-fine FE mesh around the wellbore.

DEDICATION

To my family for their endless support and patience

ACKNOWLEDGEMENTS

As I complete my studies at Texas A&M University, I would like to express my gratitude to everyone who encouraged and helped me along the way.

I would like to thank my committee chair, Dr. John Killough, my co-advisor, Dr. Mark Everett, and my committee members, Dr. Eduardo Gildin and Dr. Hadi Nasrabadi, for their guidance and support throughout the course of this research.

Special thanks go to my adviser Dr. John Killough for accepting me into his reservoir simulation group. He offered me a lot of inspiration and support in finding a direction for my research. I learned a lot from his vast knowledge of reservoir simulation and enjoyed working as his teaching assistant.

My deepest gratitude goes to my co-adviser Dr. Mark Everett. I appreciate the many hours he spent with me discussing research. Without his support and guidance this work would not have been possible.

I also want to sincerely thank Dr. Eduardo Gildin and Dr. Hadi Nasrabadi for taking the time to review my dissertation and provide valuable feedback. Additionally, I would like to show appreciation to Dr. Gildin for his mentorship during my time in the Academy for Future Faculty program.

I would like to thank Dr. Zoya Heidari and the Heidari Multi-scale Formation Evaluation Group for their support in the earlier stages of my research. I especially want to thank my colleague Lu Chi for the many research discussions we had while preparing a conference paper together.

My sincere thanks goes to the department faculty and staff at Texas A&M University for their kindness, guidance, and support. Thanks go to Dr. Mike King for his guidance and mentorship during my time teaching in the petroleum engineering department. I would also like to thank Dr. Bryan Maggard for our many technical conversations over the years. Special thanks to Ms. Eleanor Schuler for her time and help in assisting my graduation procedure.

I would like to thank all my friends and colleagues at Texas A&M University for making my time here a pleasant experience. I have learned a lot over the years from working with Killough Reservoir Simulation Research Group and the Everett Electromagnetics Research Group. Additionally, I would like to express my gratitude to all the students I have shared an office with. They have made my time here productive and enjoyable.

Finally, I would like to thank my family for their unconditional love and support over the years, especially my wife Amelia for her kindness and patience during my many long nights of studying, my two children William and Julia for their moral support, and my parents Robert and Sue for their encouragement and unwavering support.

CONTRIBUTORS AND FUNDING SOURCES

Contributors

This work was supported by a dissertation committee consisting of Professor John Killough [advisor], Professor Eduardo Gildin, and Professor Hadi Nasrabadi of the Department of Petroleum Engineering and Professor Mark Everett [co-advisor] of the Department of Geology and Geophysics.

The nuclear magnetic resonance (NMR) applied in Chapter 2 was developed by Dr. Lu Chi. Dr. Chi was a member of the Heidari Multi-scale Formation Evaluation Group in the Department of Petroleum Engineering at Texas A&M University.

All other work conducted for this dissertation was completed by the student independently.

Funding Sources

Graduate study was supported by a teaching assistant position provided through the Harold Vance Department of Petroleum Engineering at Texas A&M University, a graduate teaching fellowship provided through the Dwight Look College of Engineering at Texas A&M University, and a fellowship from Chevron Corporation provided through the Harold Vance Department of Petroleum Engineering Department at Texas A&M University.

NOMENCLATURE

a	:	radius of the mandrel (m)
a_n	:	cylindrical interfaces (m)
A	:	magnetic vector potential (A)
A_s	:	secondary magnetic vector potential (A)
$A_p(r)$	:	Hankel transform (V)
B	:	magnetic flux density (T)
C_{sh}	:	volumetric concentration of shale (unitless)
d	:	diameter of the pores (μm)
D	:	diffusion coefficient of pore fluids (m^2/sec) used in Chapter 2; or burial depth (skin depths) used in Chapter 4 and Appendix C
D_t	:	fractional diffusion operator (unitless)
$Dt^{1-\beta}$	:	fractional derivative (unitless)
E	:	electric field (A)
E_y^i	:	incident electric field (A)
E_y^S	:	scattered electric field (A)
f	:	frequency (Hz)
F	:	Lorenz force (N) used in Chapter 1; or electrical formation factor (unitless) used in Chapter 2
$g(\rho,z)$	:	geometric factor (unitless)
G	:	spatial gradient of the internal magnetic field (Hz/mm) used in Chapter 2, or conductive half-space Green's function (unitless) used in Appendix C

H	:	magnetic field strength (A/m) used in Appendix C; or inhomogeneity height in the integral equation method (skin depths) used in Chapter 4 and Appendix C
H_x	:	total horizontal magnetic field response (A/m)
H_x^S	:	scattered horizontal magnetic field response (A/m)
H_z	:	total vertical magnetic field response (A/m)
H_x^P	:	primary portion of the horizontal magnetic field response (A/m)
H_z^P	:	primary portion of the vertical magnetic field response (A/m)
H_z^S	:	scattered vertical magnetic field response (A/m)
I	:	current in the transmitter coil (A) used in Chapter 1; or infinite line source current (A) used in Chapter 4
$\mathrm{Imag}(B_z)$	:	imaginary (out-of-phase) component the magnetic field (k/s^2)
J	:	current density (A/m^2)
J_i	:	impressed electric current (A/m^2)
J_s	:	source current density (A/m^2)
J_1	:	Bessel function of order one (unitless)
K	:	sensitivity factor derived from geometry and logging tool parameters (unitless) used in Chapter 1; or a complex dense matrix in the integral equation method (unitless) used in Chapter 4 and Appendix C; or electrical conductivity contrast between inhomogeneity and surrounding host formation (unitless) used in Appendix C
K_1	:	modified Bessel function of order zero (unitless)
K_2	:	modified Bessel function of order one (unitless)
L	:	intercoil spacing (m) used in Chapter 1; or planar fracture length (μm) used in Chapter 2
M_0	:	magnetic permeability (Hz/m)
M_i	:	impressed magnetic current (Hz/m)

P	:	geometrical factor described by a generic integral (unitless)
q	:	mobile charge carrier (C)
r_w	:	connate water resistivity (ohm·m)
r_{wb}	:	clay bound water resistivity (ohm·m)
R_a	:	apparent resistivity (ohm·m)
X_a	:	distance between inhomogeneity center and infinite-line source (skin depths)
S_{wt}	:	total water saturation (unitless)
S/V	:	surface-to-volume ratio of the pore space (1/m)
$T^{1-\beta}$	:	power law probability density function (unitless)
T	:	inhomogeneity width in the integral equation method (skin depths)
TE	:	inter-echo spacing time (μsec)
T_1	:	longitudinal relaxation time (msec)
T_2	:	transverse relaxation time (msec)
T_{2p}	:	relaxation time associated with inter-granular pores (msec)
T_{2B}	:	bulk relaxation time (msec)
T_{2D}	:	diffusion-induced relaxation time (msec)
T_{2S}	:	surface relaxation time (msec)
U	:	electric potential (V)
v	:	velocity of the moving mobile charge carrier (m/s)
V_R	:	voltage induced by the receiver coil (V)
w	:	aperture of planar fractures (μm)
$\hat{y}$	:	admittivity (S/m)

$\hat{y}_*$: normal values of admittivity (S/m)

z : vertical position on the cylindrical solution domain (m)

$\hat{z}$: impedivity (ohm·m)

$\hat{z}_*$: normal values of impedivity (ohm·m)

β : waiting time distribution in the continuous-time random walk model (unitless)

γ : gyromagnetic ratio of a proton ($rad \cdot sec^{-1} \cdot T^{-1}$)

Γ : gamma function serving as a normalizing constant (unitless)

δ : skin depth (m)

δ_2 : skin depth in the inhomogeneity body (m)

ε : permittivity (F/m)

ε_0 : permittivity of free space (F/m)

μ : magnetic permeability (H/m) used in Chapter 1; or inductivity (H) used in Appendix C

μ_0 : magnetic permeability of free space (H/m)

ρ : surface relaxivity (μm/sec)

ρ_2 : surface relaxivity (μm/sec)

σ : formation electrical conductivity (S/m)

σE : ohmic conduction term (A ·S /m)

$\sigma(r)$: spatially varying electrical conductivity of the geological formation (S/m)

σ_a : apparent conductivity (S/m)

σ_g : apparent conductivity seen by the induction logging tool (S/m)

σ_0 : known background electrical conductivity (S/m)

σ_1 : electrical conductivity of the inhomogeneity (S/m)

σ_2 : electrical conductivity of the host formation (S/m)

σ_β : generalized conductivity, ($A^2s^3kg^{-1}m^{-3}s^{-\beta}$)

ϕ_{frac} : porosity associated to fractures (%)

ϕ_{pore} : inter-granular porosity (%)

$\phi_{F,coupled}$: coupled micro-fractures (%)

$\phi_{F,iso}$: isolated micro-fractures (%)

ϕ_t : total resistivity using NMR measurement (ohm·m)

ϕ_{tot} : total porosity of rock (%)

Φ : reduced scaler potential (A/m · rad/sec)

ω : angular frequency (rad/sec)

ABBREVIATIONS

Bi-CG	:	bi-conjugate gradient
BICSTAB	:	stabilized bi-conjugate gradient
cEDFM	:	compartmental embedded discrete fracture model
CPMG	:	Carr-Purcell-Meiboom-Gill
CG	:	conjugate gradient
CGS	:	conjugate gradients squared
CSEM	:	controlled-source electromagnetic
CTRW	:	continuous-time random walk
EDFM	:	embedded discrete fracture model
EM	:	electromagnetic
FD	:	finite-difference
FE	:	finite-element
FEM	:	finite-element method
FV	:	finite-volume
GMRES	:	generalized minimal residual
Hi-FEM	:	hierarchical finite-element method
IE	:	integral equation
LWD	:	logging-while-drilling
LU	:	lower-upper
MLSI	:	moving least-squares interpolant

MoM	:	method-of-moments
MT	:	magnetotelluric
NMR	:	nuclear magnetic resonance
RX	:	receiver
SNR	:	signal-to-noise ratio
SRV	:	stimulated reservoir volume
SVD	:	singular value decomposition
T_1	:	longitudinal relaxation time
T_2	:	transverse relaxation time
TX	:	transmitter
QMR	:	quasi-minimal residual
QR	:	matrix decomposition into an orthogonal matrix “Q” and upper triangular matrix “R”
1-D	:	one-dimensional
2-D	:	two-dimensional
2.5-D	:	two-dimensional primary excitation imposed on a three-dimensional structure
3-D	:	three-dimensional

TABLE OF CONTENTS

Page

Page

Page

LIST OF FIGURES

Page

Page

Page

Page

Page

LIST OF TABLES

Page

CHAPTER I

INTRODUCTION

This chapter reviews background information for the electromagnetic (EM) and nuclear methods I have used in the research, and the scope, objectives, and organization of this dissertation. Controlled-source electromagnetic (CSEM) methods are inexpensive geophysical techniques that can be combined with petrophysical and petroleum engineering methods to improve our understanding of subsurface formation characterization and fluid monitoring. I investigate two forms of CSEM methods: EM induction logging and terrestrial CSEM.

Induction logging is a standard formation evaluation tool for characterization of electrical properties in the near-wellbore region. The tool relies on a purely inductive loop source to energize and thereafter measure the electrical conductivity of the surrounding formation. As a benefit of measuring electrical conductivity, induction logging simulation can provide high-grading of natural fracture corridors and reliable fracture geometry characterization.

Surface-based (terrestrial) CSEM methods are better suited for far-field diagnostics away from a wellbore. In these methods, the presence of a grounded wire dipole deployed at the surface acts as the source as opposed to the purely inductive loop source used in induction logging. Ground coupling of the dipole is achieved through direct electrical contact with the surface via electrodes, as opposed to magnetic flux linkage per the inductive methods. Surface-based CSEM methods have been established

for a range of industry applications including CO_2 storage and geothermal exploration (Castillo-Reyes et. al., 2022), terrestrial hydrocarbon exploration (Streich 2016), buried pipeline integrity (Couchman and Everett, 2022), and hydraulic fracturing fluid flowback (Jones et. al. 2019). In these applications, the EM response of a conductive wellbore casing must be accurately modeled and included in response simulations.

This dissertation provides a new approach for combining EM induction logging (via anomalous diffusion simulation) with nuclear magnetic resonance (NMR) fracture-pore diffusional coupling to improve micro-fracture density estimation. The combination produces a new method for characterizing natural fracture corridors. The dissertation also describes an approach for modeling the EM response of conductive wellbore casing using a newly developed hybrid finite-element integral (FE-IE) equation method.

1.1 Background

1.1.1 Finite-Element Method

Solving Maxwell's diffusion equations in the subsurface is challenging due to the complex nature of inhomogeneous electrically conducting media. A common approach to solving the equations is to use numerical techniques such as the finite-element (FE) or finite-difference (FD) method. Both FE and FD methods provide similar solution accuracy, memory storage requirements, and computational speed. However, the FE method permits an unstructured mesh allowing for local refinement around a wellbore casing or other strong contrasts in electrical conductivity. Both FE and FD approaches operate by discretizing the subsurface into a mesh whose degrees of freedom are defined

by connected nodes, edges, and/or elements. A system of linear equations describing Maxwell's diffusion equations can then be solved to determine the degrees of freedom. This dissertation uses the FE method for controlled-source electromagnetic (CSEM) induction using Coulomb-gauged secondary potentials. An abbreviated version of the mathematical development for the Coulomb-gauged potential formulation of Maxwell's equations in the inductive regime is included in Appendix B. A more in-depth review can be found in Badea et al. 2001.

A typical FE analysis comprises pre-processing, processing, and post-processing. During the pre-processing phase, the initial parameters are selected and the FE mesh is generated. Processing involves numerical analysis to solve the governing linear system, and post-processing is where the final results are assembled and visualized.

The pre-processing phase involves choosing boundary conditions, defining material properties, selecting element type, and generating a mesh. The governing equations are discretized; they describe the partial differential equations being solved, in our case Maxwell's equations. Additional input parameters defining material properties (such as the electrical conductivity of air, fluids, structures, and formation layers) are also included in the pre-processing phase. There are several different element types that can be used depending on the dimensionality of the problem. Some common 3-D elements include tetrahedral, cubic, and cylindrical. A FE mesh is then built by discretizing the subsurface into individual elements and connecting their vertices along edges and facets. An example of horizontal mesh slices of a tetrahedral mesh, displaying triangular facets, is shown in Figure 1.1.

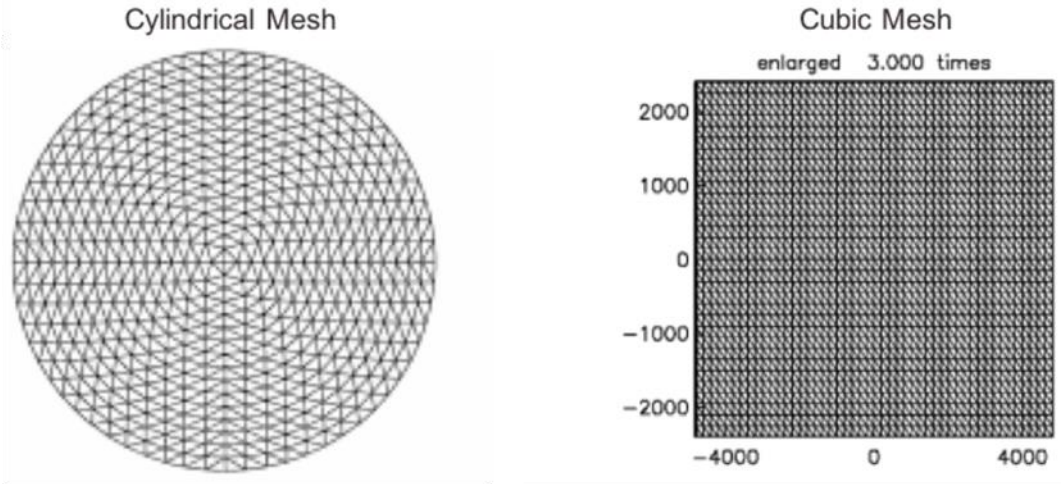

Figure 1.1 – Horizontal slices through cylindrical and rectangular meshes generated in the FEM program. Reprinted from Couchman, 2022.

A formulation that uses special "edge elements" is advantageous insofar as these elements produce divergence-free solutions without nonphysical, or spurious modes. Other special elements may be represented as a set of infinitesimally thin edges, each connecting two nodes within the grid (Weiss, 2017). The elements used in this dissertation are node-based, where the Coulomb-gauge condition is enforced to ensure that there are no spurious modes (Paulsen and Lynch, 1991).

The processing phase of the FE solution assembles and solves the linear matrix system. The latter is assembled from the coupled system of governing differential equations. The degrees of freedom, in this case the secondary nodal potentials, are expanded into piecewise linear representations. From there a linear system of equation in the form, $\Lambda u=b$, can be obtained using the Galerkin method. The linear system equation

is then solved numerically. This research iteratively solves the FE matrix with a quasi-minimal residual (QMR) algorithm.

The post-processing phase of the FE solution involves constructing and visualizing the results. The computed results (secondary potentials) and their spatial derivatives are interpolated using a moving least-squares (MLSI) interpolant (Tabbara et al. 1994) to derive electric or magnetic field responses. The frequency-domain electric field is used as an input if it is desired to compute a step-off or transient response in the time domain. Electric and magnetic field patterns can then be visualized throughout the modeling domain as contour maps of response amplitudes and/or phases.

1.1.2 Seatem: Finite-Element Simulator

The in-house software *seatem* is a node-based FE simulator developed in FORTRAN. *Seatem* solves the governing diffusive Maxwell equations formulated in terms of secondary Coulomb-gauge electromagnetic potentials. The versions of *seatem* used in this research are adaptations of the original program development described in Badea et. al (2001) with later modifications by Stalnaker et. al (2006). An abbreviated version of the mathematical development of *seatem* is included in Appendix B. *Seatem* consists of four modules: a mesh generator, a module for assembling and solving the FE matrix, a module for post-processing the FE solution, and a module for visualizing EM field patterns. An illustration of the *seatem* workflow is given in Figure 1.2.

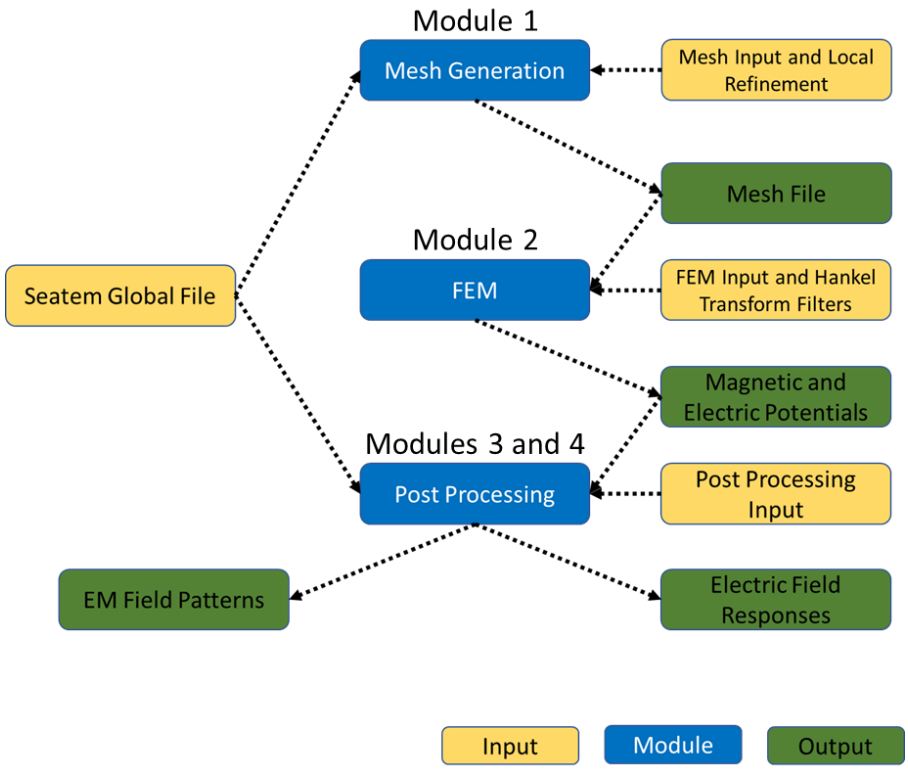

Figure 1.2 – Workflow for the in-house FE simulator *seatem*.

The first module reads the parameter and mesh input files and generates the mesh on which the CSEM response is computed. Specifically, module 1 reads in a specified model geometry and outputs a file containing an unstructured mesh. Local mesh refinement is available through a process that subdivides selected mesh elements by a designated number of "split points" (Figure 1.3). The teterahedra designated for refinement are subdivided into 2, 4, or 8 subtetrahedra (Figure 1.4). Increasing the number of nested refinements increases the density of the nodes within the refined portion of the mesh. The latter is typically located near strong gradients in electrical

conductivity. Local mesh refinement typically improves solution accuracy, at the cost of increasing computational time and memory.

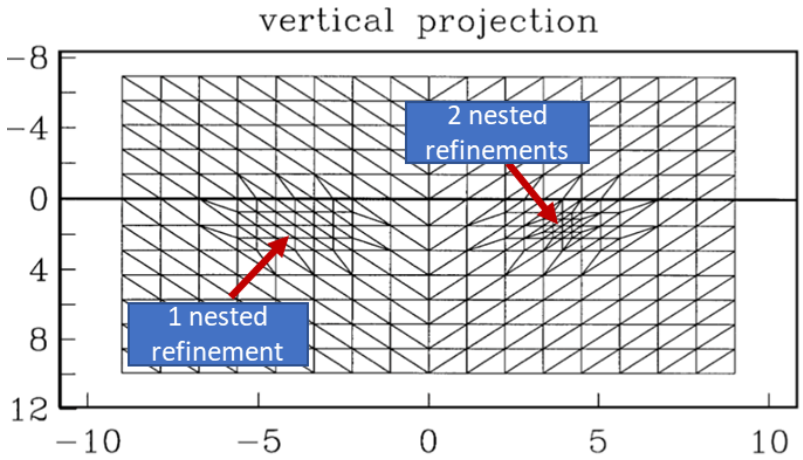

Figure 1.3 – Tetrahedral mesh design with nested refinements. Modified from Badea et. al, 2001.

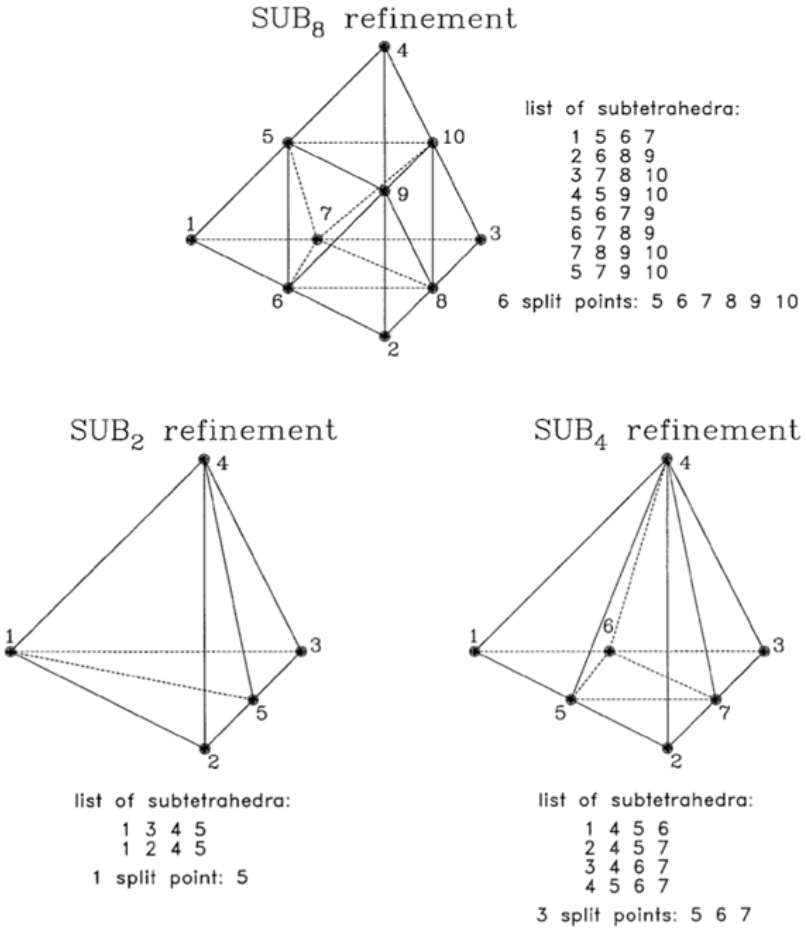

Figure 1.4 – Subdivision of tetrahedral mesh by number of split points. Reprinted from Badea et. al, 2001.

The second module of *seatem* assembles the FE matrix and populates it with inner products involving the conductivity of each mesh element and the tetrahedral basis functions. Next, the secondary Coulomb-gauged electromagnetic potentials are calculated, assuming they are driven by a right-hand-side "source" vector containing analytically derived primary potentials. Formulating the secondary potentials in the

Coulomb gauge (Equation 1.1) avoids the curl-curl term (Equation 1.2), leading to better matrix conditioning as the curl-curl term places a small value on the matrix diagonal.

$$\nabla \cdot \mathrm{A} = 0 \tag{1.1}$$

$$\nabla \mathrm{X} \nabla \mathrm{X} \mathrm{A} = -\nabla^2 \mathrm{A} \tag{1.2}$$

In the above equations, A is the magnetic vector potential.

The matrix conditioning is further improved using a Jacobi preconditioner that adds additional weight to the main diagonal. A quasi-minimal residual method iteratively solves the sparse, banded system. The solver outputs the secondary vector-magnetic and scalar-electric potentials at each vertex of the 3-D mesh. The use of primary potentials removes singularities and large solution gradients at or near the EM source, i.e the grounded electric dipole. Primary, secondary, and total (addition of primary and secondary) field potentials are interpolated onto surface nodes, where measurements in field applications are made.

The third and fourth modules provide post-processing of the FE solution. Module 3 reads the potentials computed in the second module and derives the electric and magnetic field responses. The module also interpolates the latter at surface nodes yielding responses that would be measured by ideal noise-free receivers. Module 4 acquires the total potentials on all subsurface nodes from Module 2 and constructs electric and magnetic field patterns, in the form of contour maps, throughout the modeling domain.

1.1.3 Induction Logging

Induction logging is a low-frequency controlled-source electromagnetic (CSEM) technique deployed as either a wireline or logging-while-drilling (LWD) method. An induction logging tool avoids direct electrical contact with the borehole wall by using sets of coils that enclose an insulating cylindrical mandrel. In the case of a simple two-coil system, shown in Figure 1.5, alternating current flows through the lower TX (transmitter) coil, and induces a horizontal electric current (the "ground loop") in the geologic formation around it. The field of the ground loop creates time-varying magnetic flux that passes through the upper RX (receiver) loop and is registered as a voltage.

.

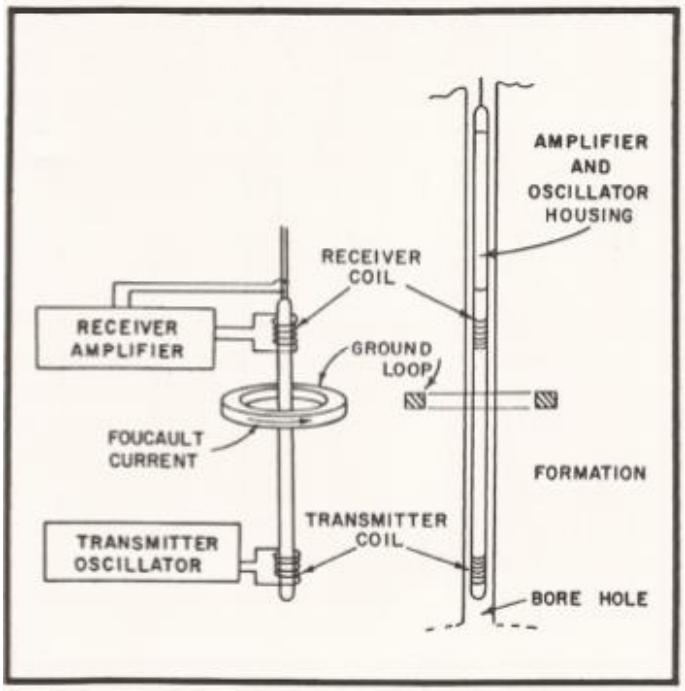

Figure 1.5 – Basic two-coil induction system. Reprinted from Schlumberger, 1969.

The ground loop is formed by eddy currents carried by migrating ions such as Na^+ and Cl^- in the pore fluid electrolyte. Spatial changes in formation conductivity are caused by formation heterogeneity or fluid distribution. A Lorentz force is experienced by the drifting charge carriers in the medium. Bound charges confined to the single atoms and mobile charges trapped at material interfaces also experience a Lorenz force but these have little to no impact on the low-frequency EM induction response. It is the drift of the mobile charges that generates the measured electromagnetic response (Everett, 2013). The Lorentz force is

$$F = q(E + v \times B) \tag{1.3}$$

where q is the charge of the mobile carrier, v is its velocity, E is electric field, and B is magnetic field.

The superposition of the primary and secondary EM magnetic flux produces the total voltage that is induced in the RX coil. The out-of-phase component of the secondary voltage generates a signal that is proportional to the apparent conductivity of the surrounding formation.

Use of the induction method in well logging was first proposed by Doll (1949). Doll suggested that one could measure the mutual coupling between two coaxial loops placed in a wellbore. Doll developed the following general equation in 2-D cylindrical coordinates (ρ, z) for the apparent conductivity registered by the induction logging tool:

$$\sigma_g = \int_{-\infty}^{\infty} dz \int_0^{\infty} g(\rho, z)\sigma(\rho, z)\, d\rho \tag{1.4}$$

where σ_g is the apparent conductivity, $g(\rho,z)$ is a geometric factor depending on the placement of the coils, and $\sigma(\rho,z)$ is the formation conductivity.

Among the assumptions of Doll's method are that the induced ground loops are not magnetically flux-linked and propagation effects are neglected. Wait (1984) improved upon Doll's method to include these effects and described the apparent conductivity equation for a multilayer case with concentric layers about the borehole. Wait found the following expression for apparent conductivity:

$$\sigma_a = \sigma_0 + \sum_{n=1,2,\ldots}^{n} (\sigma_n - \sigma_{n-1}) P\left(\frac{L}{a_n}\right) \tag{1.5}$$

with

$$P(y) = \frac{y}{\pi} \int_0^{\infty} x\{x[K_0^2(x) - K_1^2(x)] + 2K_0(x)K_1(x)\} \cos(xy) dx \tag{1.6}$$

where L is the intercoil spacing, a_n are the cylindrical interfaces, P is a geometrical factor (Kaufman 1965), and K_0 and K_1 are modified Bessel functions.

The approach used in this dissertation is adapted from the method outlined in Bray (2013). Apparent conductivity is based on the following equations (Moran and Kunz, 1962):

$$\sigma_a = \frac{V_R}{K} \tag{1.7}$$

$$V_R = \omega A \, \mathrm{Imag}\{B_z\} \tag{1.8}$$

$$K = \frac{\omega^2 \mu^2 \pi a^4}{4L} I \tag{1.9}$$

where V_R is the voltage induced by the receiver coil, K is a sensitivity factor derived from TX-RX coil geometry and logging tool parameters, ω is the operating frequency, A is the area bounding the flux of the magnetic field, Imag(B_z) is the imaginary or out-of-phase component of the magnetic field at the RX locations, μ is the magnetic permeability (norminally that of free space), a is the radius of the mandrel, L is the transmitter-receiver offset, and I is the current in the transmitter coil.

1.1.4 Nuclear Magnetic Resonance (NMR)

Nuclear magnetic resonance (NMR) logging is an unconventional logging technique that measures the formation relaxation and diffusion properties. It is sensitive to various parameters including; pore size, permeability, fluid viscosity, hydrogen content, saturations, and clay surface area. NMR measurements may be used on any nucleus that has an odd number of neutrons, protons, or combinations. Nuclei typically contain both a magnetic moment and an angular momentum with the magnetic axis in alignment with the spin axis. Protons are of particular interest to the oil and gas industry due to the abundance of hydrocarbons and water which contain a large magnetic moment with a strong and measurable signal.

NMR logging operates by generating a magnetic field that aligns randomly oriented protons to that applied field. After equilibrium is achieved, an oscillating magnetic field is then created causing the protons to be tipped. Removing the oscillating magnetic field sends protons back to their original direction. The amplitude from realigning the spin magnetization with a resonant electromagnetic radiation pulse (spin-echo) over time is then measured by the NMR logging tool. These measurements are affected by the following parameters: diffusivity (extent of the random movement of molecules in the fluid), hydrogen index (density of hydrogen atoms in the fluid), T_1 (longitudinal relaxation time describing the rate at which tipped protons relax longitudinally in the fluid), and T_2 (spin-spin relaxation time describing the rate at which tipped protons relax transversely in the fluid).

There are three main relaxation mechanisms that create NMR longitudinal and transverse relaxation: bulk relaxation, surface relaxation, and diffusive relaxation. Bulk relaxation is a fluid independent property that results from fluctuations in local magnetic fields occurring from the random motion of neighboring spins, while surface relaxation occurs due to Brownian motion of diffusing particles (Talabi, 2008). Both bulk and surface relaxation appear in longitudinal and transverse directions. The fluids on the surface have a rapid relaxation rate compared to the bulk fluids within the pore space. Diffusive relaxation occurs only in the transverse direction. It is measured using a pulse sequence such as Carr-Purcell-Meiboom-Gill (CPMG).

NMR T_2 and its distribution are the most widely used interpretation methods for NMR relaxometry (Chi and Heidari 2014). Coates et al. (1999) gives equation (1.10) for the T_2 relaxation time of hydrogen nuclei in porous media fluids.

$$\frac{1}{T_2} = \frac{1}{T_{2B}} + \frac{1}{T_{2S}} + \frac{1}{T_{2D}} = \frac{1}{T_{2B}} + \rho_2 \left(\frac{S}{V}\right)_{pore} + \frac{D(\gamma \cdot G \cdot TE)^2}{12} \tag{1.10}$$

Where T_2 is the spin-spin relaxation time, T_{2B} is the bulk relaxation time, T_{2S} is the surface relaxation time, T_{2D} is the diffusion-induced relaxation time, ρ_2 is the surface relaxivity, S/V is the surface-to-volume ratio of the pore space, D is the diffusion coefficient of pore fluids, γ is the gyromagnetic ratio of a proton, G is the internal magnetic field gradient, and TE is the inter-echo spacing time.

An inversion technique can be applied to the raw data from the echo-train resulting in a T_2 distribution plot which represents pore size distribution under restricted conditions. These conditions include short inter-echo spacing in the CPMG pulse sequence, assumption of a fully-water saturated pore space, and uniform surface relaxivity across all pore space. Within these restrictions, surface relaxation methods control the relaxation process and are directly proportional to pore size Chi and Heidari (2014) Equation (1.11). Chi and Heidari also describe surface-to-volume ratios of spherical pores and planar fractures Equations (1.12) and (1.13).

$$\frac{1}{T_{2S}} \propto \left(\frac{S}{V}\right)_{pore} \propto \left(\frac{1}{d}\right)_{pore} \tag{1.11}$$

$$\left(\frac{S}{V}\right)_{sphere} = \left(\frac{6}{d}\right)_{sphere} \quad (1.12)$$

$$\left(\frac{S}{V}\right)_{plane} = \left(\frac{2}{w}\right)_{plane} \quad (1.13)$$

where d is the diameter of the pores and w is the thickness of planar fractures.

1.1.5 Skin Depth

Electromagnetic signal penetration depth in the CSEM method is limited by the conversion efficiency of the transmitted electromagnetic energy to kinetic energy of the subsurface mobile charge carriers. Higher electrical conductivity therefore leads to greater energy conversion, and consequently a smaller depth of penetration. The latter can be increased by lowering the operating frequency, at cost of degrading spatial resolution. One can determine an optimal frequency range and signal processing workflow to maximize signal-to-noise ratio (SNR). The CSEM method depth if investigation is based on "skin depth" that is controlled by formation electrical conductivity and transmitted frequency. We can calculate skin depth using Equation 1.14 developed by Moran and Kunz (1962):

$$\delta = \sqrt{\frac{2}{\mu\sigma\omega}} \quad (1.14)$$

where $\mu = 4\pi \text{ x } 10 - 7 \text{ H/m}$ denotes the magnetic permeability of free space, σ is the formation electrical conductivity, $\omega = 2\pi f$ denotes the transmitted frequency, with f in Hz.

To illustrate the effect of lowering frequency on skin depth, we calculated skin depth in a frequency range of 1-1000 Hz for brine and various common formation types. A representative brine electrical conductivity is 2 S/m, while those of four common formations are: an organic-rich shale (10^{-13} S/m), a sandstone (10^{-3} S/m), a shale formation (10^{-2} S/m), and a limestone (10^{4} S/m). Results are shown in Figure 1.6.

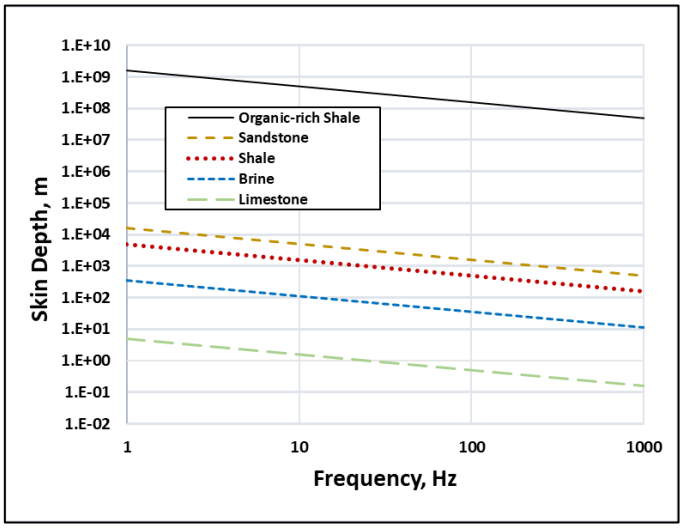

Figure 1.6 – Skin depth calculations for various frequencies in common formation types.

There is a power law relation between penetration depth, in terms of skin depths, and frequency. Higher frequencies reduce penetration depth thereby requiring an increased number of skin depths to probe to that depth. An example of the relationship is shown in Figure 1.7. We selected a formation with an average electrical conductivity of 10^{-3} S/m for common unconventional shale oil-field depths ranging from 5000 ft to 12500 ft.

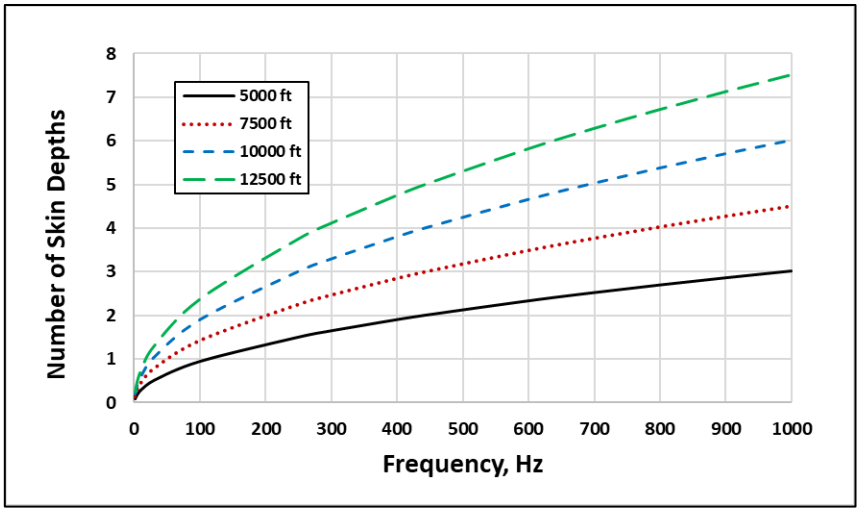

Figure 1.7 – Power law relationship between skin depth and frequency for various depths.

To maintain a strong SNR, the TX operating frequency and formation conductivity should combine to yield a depth of investigation $d \sim 1.5\delta - 2.0\delta$ (e.g. Grant and West 1965). I selected operating frequencies that probe to two skin depths based on the aforementioned power law. For a 10^{-3} S/m formation at 5000 ft depth the operating frequency should be ~250-450 Hz.

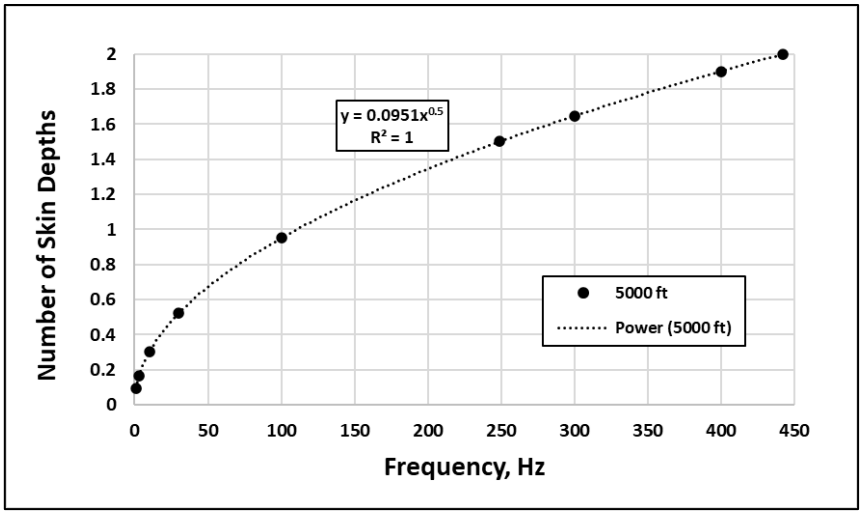

Figure 1.8 – Range of operating frequencies for maintaining a strong signal-to-noise ratio (SNR).

1.2 Research Objectives

The overall objectives of this research are to further develop electromagnetic and NMR geophysical techniques for; improving natural fracture characterization, increasing hydrocarbon production through natural fracture corridor depletion, accurately monitoring hydraulic fracturing fluid flow, and improving fracture model stimulated reservoir volume (SRV) estimation to increase unconventional reservoir simulation accuracy. Details on the milestones achieved during this research are described in the chapter outline below.

1.3 Chapter Overview

The dissertation is organized as follows:

In Chapter 2, I use controlled-source electromagnetic (CSEM) simulation to improve micro-fracture density estimation in the near-wellbore region. Chapter 2 uses a modified version of an in-house electromagnetic (EM) finite-element (FE) simulator, *seatem*. The modifications extend the capabilities of *seatem* for use as an induction logging simulator with a cylindrical mesh in the near-wellbore region transitioning to a Cartesian mesh in the far-field. An added term for quantifying the effects of anomalous EM diffusion in fractured media is also included. Simulated geologic roughness values derived from *seatem*-computed CSEM responses are combined with nuclear magnetic resonance (NMR) T_2 relaxometry simulations to improve micro-fracture density estimation in fractured carbonate and organic shale formations.

In Chapter 3, I use CSEM simulations to improve natural fracture detection and characterization in the near-wellbore region. Chapter 3 uses the modified version of *seatem* described in the previous paragraph. Simulated geologic roughness values computed by *seatem* are combined with surface gas readings and regional geomechanics to high-grade natural fracture corridors and model the EM response in the presence of interactions between hydraulic and natural fractures. This process can assist in hydraulic fracture placement for geologic targeting to improve natural fracture corridor depletion.

In Chapter 4, I describe an Integral Equation (IE) based wellbore preconditioner for 3-D EM response modeling. I precondition an FE solver, in this case *seatem*, with an integral equation (IE) primary solution that captures the CSEM response of a realistic-

sized steel wellbore casing. The version of *seatem* uses a rectangular mesh and is applied to the surface-based CSEM method. The novel hybrid IE-FE approach solves the primary field solution using a newly developed 2-D integral-equation code, and then interpolates the IE-computed solution onto the nodes of a FE mesh using an interpolation routine. Using *seatem*, I solve for secondary electric and magnetic field solutions. The hybrid FE-IE method is tested in a simple oil-field scenario with an idealized fluid-bearing zone to demonstrate the improvements to FE solution stability and computation time gained by this method.

In Chapter 5, I outline plans and give suggestions for future research.

In Chapter 6, I summarize the conclusions and contributions of this work.

CHAPTER II

ASSESSMENT OF MICRO-FRACTURE DENSITY USING COMBINED INTERPRETATION OF NMR RELAXOMETRY AND ELECTROMAGNETIC LOGS*

Assessment of micro-fracture density in hydrocarbon-bearing reservoirs is of special interest for designing production plans and selecting zones for fracture treatment. Controlled-source electromagnetic (CSEM) methods, such as induction logging, can be combined with NMR (nuclear magnetic resonance) to improve the accuracy of micro-fracture density estimation. NMR T_2 (spin-spin relaxation time) distribution has been traditionally considered insensitive to the presence of fractures. However, Lu and Heidari (2014) documented a measurable NMR sensitivity to the existence of micro-fractures using a new concept of fracture-pore diffusional coupling. The quantification of micro-fracture density in multiple porosity systems is a challenging issue, and distinguishing fractures from pore space is not possible from NMR T_2 measurement alone. However, the inclusion of additional borehole measurements, such as induction logs, enables evaluation of micro-fracture density. In this chapter, we introduce a new method to evaluate the porosity associated to micro-fractures and intra-/inter-granular pores in complex formations using combined interpretation of NMR and electromagnetic

---

* Part of this chapter is reprinted with permission from "Assessment of Micro-Fracture Density using combined Interpretation of NMR Relaxometry and Electromagnetic Logs" by Chi et al., 2014. URTeC 1922804. Copyright [2014] by Unconventional Resources Technology Conference (URTeC).

(EM) measurements.

We used a previously-introduced NMR analytical model for fracture-pore coupling to account for micro-fractures in the rock. This model was verified by Dr. Lu through NMR numerical simulations (using a random walk algorithm) from previous work. Next, we simulated EM responses in the fluid-bearing fractured media using our in-house finite-element simulator, *seatem*. *Seatem* solves the diffusive Maxwell equations and describes spatial heterogeneity through representation of anomalous diffusion of quasi-free charges generating electromagnetic eddy currents in the fracture network. Finally, these simulations were jointly interpreted to solve for micro-fracture density and intra-/inter-granular porosity.

We applied the described technique on synthetic cases devised from pore-scale images of carbonate and organic shale formations. The estimated micro-fracture density was in satisfactory agreement with the actual value. The results showed that assessment of fracture content is possible by combining the NMR analytical model of fracture-pore diffusional coupling, and EM simulations. Our introduced method for quantifying micro-fracture density can improve reservoir characterization contributing to operational decisions regarding number and location of fracture treatments for enhanced production from tight carbonate and organic-shale formations.

2.1 Introduction

Unconventional reservoirs contain vast hydrocarbon accumulations needed to meet future energy requirements. These formations are identifiable by their low

permeabilities and/or low porosities. Due to their unique geologic properties, substantial stimulation of the rock matrix in the form of hydraulic or acid fracturing is required to make these formation types economically viable for production. However, to facilitate efficient completion plans, a comprehensive characterization of the fracture network is required. One of the primary difficulties we face is an inability to accurately quantify fracture density. We can resolve this matter through joint interpretation of NMR and EM measurements.

NMR borehole measurements, although extensively applied to measure the formation porosity and pore size distribution, have been conventionally considered as insensitive to the existence of fractures. However, the concept of NMR fracture-pore diffusional coupling effect has shown that existence of micro-fractures can significantly influence the NMR T_2 distribution in multiple-porosity systems. We adapted an existing theoretical model of pore-to-pore diffusional coupling (Ramakrishnan, et al., 1999), to explain the NMR T_2 peak shifting phenomena observed between micro-fractures and inter-granular pores. We quantified the impact of micro-fractures and channel-like inclusions on NMR measurements in sandstone, carbonate, and synthetic organic shale rock samples by numerical simulations, and showed that the pore size or pore volume fraction can be significantly underestimated by NMR due to fracture-pore diffusional coupling (Chi and Heidari, 2014).

Induction logging takes place as either a wireline or logging-while-drilling method. Sets of coils encircle an insulating mandrel. In the case of a two-coil system, alternating current flows through the bottom, or TX (transmitter) coil, and induces a

horizontal EM field into the geologic formation around it. This field creates a magnetic flux link between the TX loop and the top RX (receiver) loop (Figure 2.1).

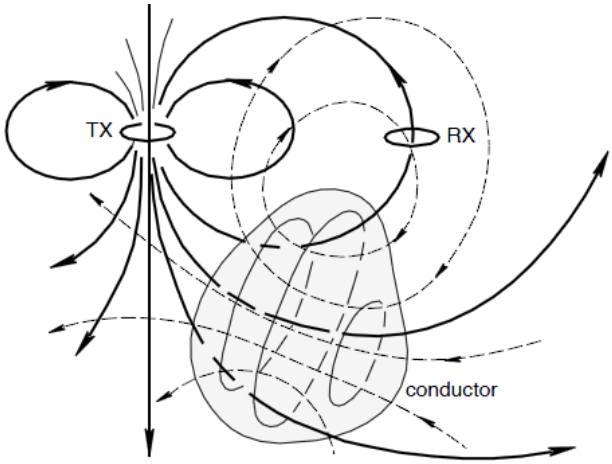

Figure 2.1 – A conceptual diagram showing the primary and secondary magnetic fields interacting with a conductive target in a CSEM survey. Reprinted from Grant and West, 1965.

A secondary magnetic field is then formed from eddy currents primarily comprised by the migration of ions, such as Na^+ and Cl^-, in the pore fluid electrolyte. This phenomenon is created by changes in formation conductivity, caused by formation heterogeneity or fluid distribution. The combination of the primary and secondary EM fields then produces a voltage that is induced in the RX coil. The in-phase and out-of-phase components of the voltage are next measured to generate a signal that is proportional to the apparent conductivity of the surrounding formation. The following sections describe the method, the results of joint interpretation of NMR and EM measurements in synthetic cases, and the conclusions.

2.2 Method

We estimate micro-fracture density by combining NMR and EM measurements. First, we interpret the core and log data for apparent formation resistivity, R_a, and total porosity, ϕ_{tot}. Then, using a version of *seatem* designed for induction logging simulation, we model the roughness of the geology via a beta value describing the effect of anomalous EM diffusion in a fracture network. This value is then used to estimate porosity associated to micro-fractures, ϕ_{frac}, and to determine pore/fracture distribution from our NMR T_2 distribution. Next, through NMR analytical model of fracture-pore diffusional coupling, we can more accurately estimate porosity associated to fractures, ϕ_{frac}, and pore space porosity, ϕ_{pore}. Figure 2.2 shows a flowchart illustrating this approach. A more detailed description of each step is presented in the following sections.

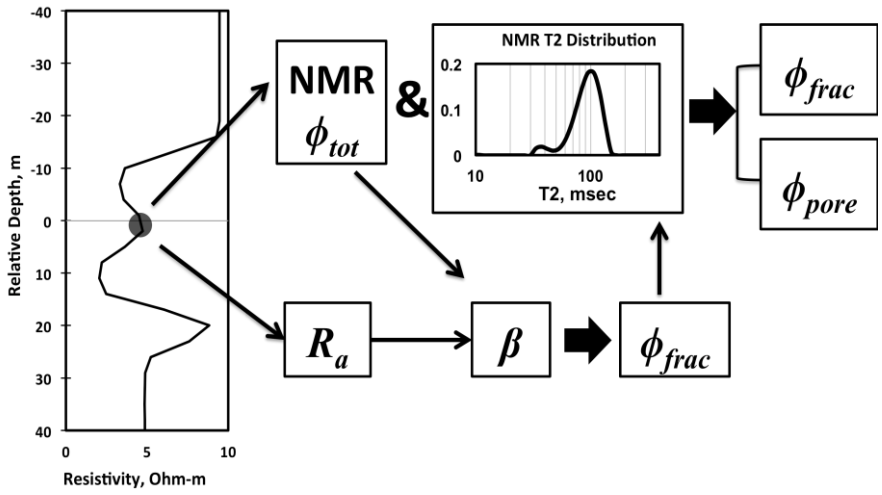

Figure 2.2 – Steps for estimating micro-fracture density through combination of NMR and EM measurements. Reprinted with permission from Chi et. al, 2014.

2.2.1 NMR Pore-Scale Simulations and T_2 Inversion

The NMR magnetization decay is simulated using a random-walk algorithm (Øren and Bakke, 2002; Ramakrishnan et al., 1998) via a C++ program adapted from the work of Talabi et al. (2009). The input file for the simulator is a digital rock matrix including 0's and 1's (0 represents pore pixel and 1 represents grain pixel), converted from the pore-scale images of rock samples. The base micro-CT images of the carbonate rock examples were provided by a project funded by Qatar National Research Fund (QNRF, Gupta et al., 2011). The pore-scale images of the organic shale rock example are synthetically generated.

In all the NMR simulations, we assume that (a) the pore space is fully saturated with brine water, and (b) there is no diffusion-induced relaxation (i.e. the internal field gradient is zero). For the carbonate and organic shale examples, the surface relaxivity values are assumed to be 10 μm/sec and 15 μm/sec, respectively (Talabi, 2008). The number of walkers assigned in each pore voxel is 4 for carbonate, and 5 for organic shale, respectively. The NMR T_2 distribution is estimated after inversion of the simulated NMR magnetization decay using a curvature smoothing method (Chen et al., 1999; Talabi et al., 2009; Toumelin et al., 2003). The areas under NMR T_2 distribution curves are proportional to their total porosity.

2.2.2 Fracture-Pore Diffusional Coupling in NMR Measurements

The NMR fracture-pore coupling model introduced in our previous work was adapted from the diffusional coupling model proposed by Ramakrishnan et al. (1999).

We adapted the approximate 1-D analytical solutions from Ramakrishnan's work (1999), by replacing their terms for micro- and macro-pores with our definitions of inter-granular pores and micro-fractures, respectively. We defined the micro-fractures that are diffusionally coupled (i.e. connected) with inter-granular pores as "coupled fractures", and those not connected to inter-granular pores as "isolated fractures". In a previous publication, we expressed the relaxation time associated to the coupled fractures, $T_{2F,coupled}$, as Equation 2.1:

$$\frac{1}{T_{2F,coupled}} = \frac{2}{w}\left[\sqrt{\frac{\sigma_{pore} D}{T_{2p} F}} + \rho\left(1 - \phi_{pore}\right)\right] \tag{2.1}$$

where w is the thickness of planar fractures, D is the diffusion coefficient of saturating fluids (brine water) within the rock, ρ is the surface relaxivity of the rock grains, T_{2p} is the relaxation time associated to inter-granular pores, and F and ϕ_{pore} are the formation factor and the inter-granular porosity in the inter-granular pore domain, respectively.

In the analytical model, the amplitude of T_2 modes is proportional to the volume fraction of corresponding pore structures. The T_2 mode amplitude of isolated micro-fractures, $\phi_{F,iso}$, shows the real volume fraction taken by the micro-fractures; while the T_2 mode amplitude of coupled micro-fractures, $\phi_{F,coupled}$, shows the apparent volume fraction measured by NMR, which has been overestimated from the real value due to fracture-pore diffusional coupling. According to the relationship between $\phi_{F,coupled}$ and

$\phi_{F,iso}$ (Ramakrishnan et al., 1999), we estimated the real volume fraction of micro-fracture, $\phi_{F,iso}$, i.e. the micro-fracture density, by Equation 2.2:

$$\phi_{F,iso} \cong \phi_{F,coupled} \frac{(1 + X/2)}{(1 + X)^2} \tag{2.2}$$

where

$$X \cong \frac{T_{2p}/T_{2F,coupled}}{\sqrt{1 - T_{2p}/T_{2F,coupled}}}$$

in which $\phi_{F,coupled}$, T_{2p}, and $T_{2F,coupled}$ were obtained from the measured (or simulated) NMR T_2 distributions.

Furthermore, we can estimate the real porosity of pore space, ϕ_{pore}, by Equation 2.3:

$$\phi_{pore} = \phi_{tot} - \phi_{F,iso} \tag{2.3}$$

where ϕ_{tot} is the total porosity of rock, which can be measured by NMR. Thereafter, we can estimate the thickness of planar fractures, w, based on Equation 2.4:

$$w = 2T_{2F,coupled} \left[\sqrt{\frac{\phi_{pore} D}{T_{2p} F} + \rho\left(1 - \phi_{pore}\right)} \right] \tag{2.4}$$

as long as we know the values of the parameters ρ, D and F. A water diffusion coefficient of D = 2.07×10^{-9} m^2/s was used in this chapter. We assumed the surface relaxivity, ρ, as 10μm/sec and 15 μm/sec for carbonate and organic shale cases, respectively. The electrical formation factor, F, can be expressed as $1/\phi_{pore}^{m}$ according to Archie's law. We then selected the parameter, m, as 2.6 and 1.7 for carbonate and organic shale cases, respectively, and estimated the fracture thickness. We emphasize that the fracture thickness estimation is highly sensitive to the value of electrical formation factor, thus sensitive to the parameter m.

2.2.3 Pore-Scale Numerical Simulations for Rock Electrical Resistivity

To estimate the effective electrical resistivity of the rock samples, we use the finite-difference method to solve the Laplace equation, defined via Equation 2.5:

$$\nabla \cdot (\sigma \cdot \nabla U) = 0 \tag{2.5}$$

where σ is the electric conductivity and U is the electric potential. We input the electric conductivity of each matrix component (e.g. grains, water, …etc), and then apply a constant electric potential difference on the two boundaries of the interested direction. The output from the simulator is the spatial distribution of the electric field, which can be directly used to calculate the electrical resistivity of the rock sample. The calculated electrical resistivity is used as input parameters for the EM simulation as described

below. Our pore scale simulations are used only as a method to represent the apparent resistivity reading given by induction logs.

2.2.4 Numerical Simulations for EM Response

We simulated EM borehole measurements using our previously developed Finite-Element (FE) induction logging simulator written in FORTRAN. *Seatem* solves the governing diffusive Maxwell equations using a node-based FE technique. The equations are formulated in terms of secondary Coulomb-gauged electromagnetic potentials with a well-conditioned FE matrix (achieved using an iterative Quasi Minimum Residual (QMR) solver with a Jacobi matrix preconditioner). We then display the results as 3-D heterogeneous electrical conductivity distributions on a cylindrical mesh. All of the FE calculations employ a singularity removal by solving for secondary potentials while the primary potentials remain analytic.

2.2.5 Geologic Roughness in EM Simulations

In a homogeneous geologic formation the migration of charge carriers move around unrestricted. The introduction of hierarchical structure in conductivity causes variations in spatial heterogeneity leading to an anomalous diffusion response of the EM current. In anomalous diffusion the charge carriers are confined to the fracture network and cannot move into the matrix. Figure 2.3 (Metzler and Klafter, 2000) illustrates an example of classical and anomalous diffusion.

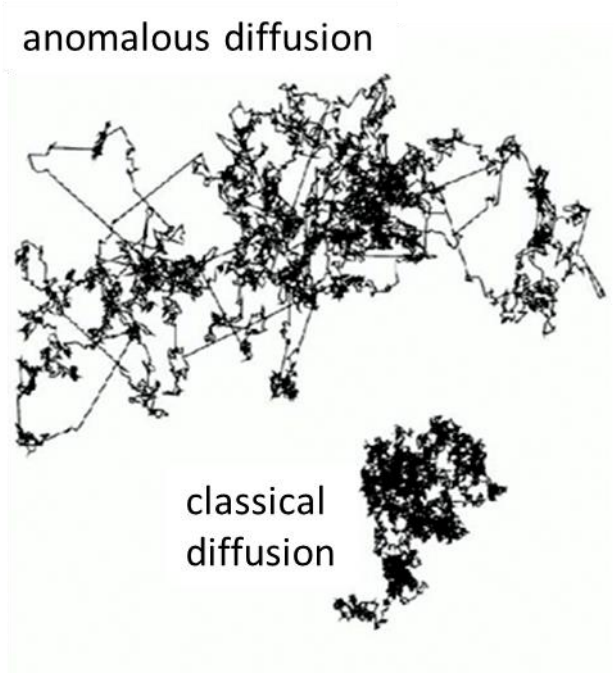

Figure 2.3 – Example of classical and anomalous diffusion. Reprinted from Mezler and Klafter, 2000.

This concept of anomalous diffusion applies to electromagnetic particles when exposed to a time-varying magnetic field. We have an external changing flux, represented by the partial derivative of the magnetic field with respect to time. This changing flux will cause an anomalous diffusion of quasi-free charges, generating electromagnetic eddy currents in the fracture network. We then model this hierarchical behavior using a Continuous Time Random Walk (CTRW) algorithm for the migrating charge within a confined geometry, with non-Gaussian distribution of step lengths or waiting times between steps. Figure 2.4 illustrates how the CTRW can capture anomalous diffusion of quasi-free charges generating EM eddy currents in the fracture network.

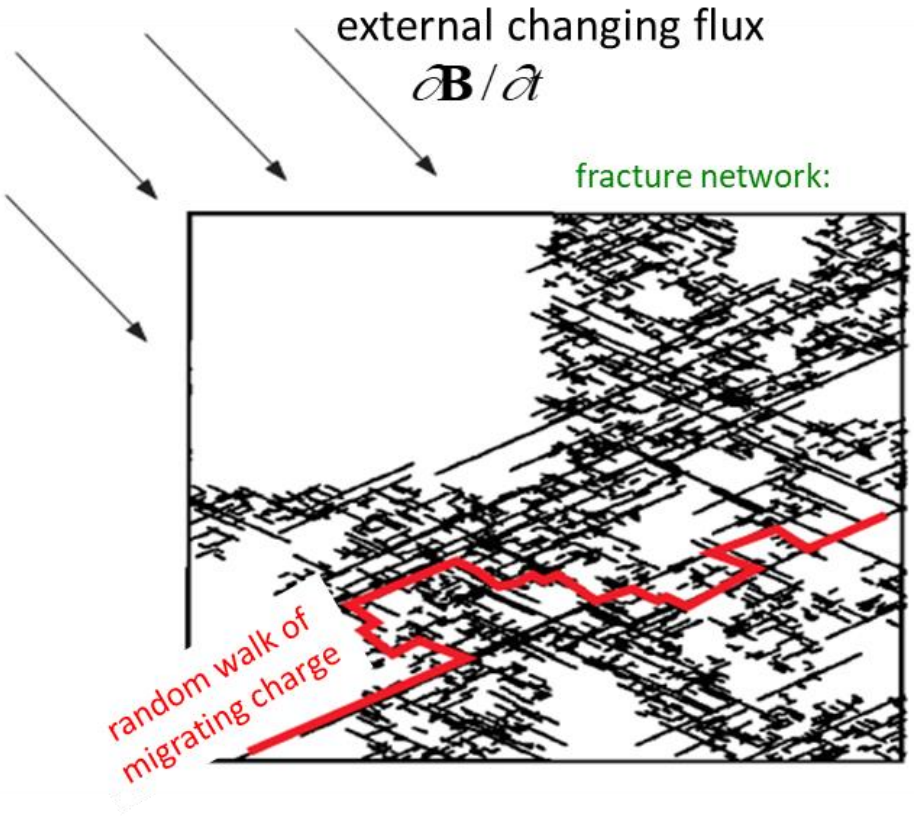

Figure 2.4 – Example of the random walk of migrating charge due to an external changing magnetic flux in a simulated fractal fault network. Modified from Bour and Davy, 1999.

We represent this by applying a spatially uniform roughness parameter, β (Ge, 2014). This parameter represents the waiting time distribution of a charge carrier undertaking a random walk in a fractal geoelectrical network. It is then used to describe the degree of fracturing in the formation. An increasing β parameter indicates an addition in fracturing of the subsurface, while a β value of zero leads to the classical diffusion solution seen for a homogeneous medium. However, as β approaches a value of 1, we observe a subdiffusion response in the EM current. The β parameter is incorporated into the convolutional vector diffusion equation for the electric field E. Everett (2009)

derived a fractional vector diffusion equation from the time-convolutional form of Ohm's law using a Reimann-Liouville fractional derivative. It is displayed below in Equation 2.6:

$$\frac{\partial}{\partial t}\sigma_\beta * E = \frac{\sigma_\beta}{\Gamma(\beta)}\frac{\partial}{\partial t}\int_0^t \frac{dt' E(t)}{(t-t')^{1-\beta}} = \sigma_{\beta 0} D_t^{1-\beta} E(t) \tag{2.6}$$

where σ_β is the generalized conductivity, E is the external electric field, β is the waiting time distribution for the CTRW model (geologic roughness parameter), D_t is the fractional diffusion operator, and Γ is the Gamma function serving as a normalizing constant. Equation 2.7 shows a compact form of the vector diffusion equation for the electric field E:

$$\nabla\times\nabla\times E = -\mu_0\sigma_{\beta 0} D_t^{1-\beta} E(t) - \mu_0 \frac{\partial}{\partial t} J_s \tag{2.7}$$

where J_s indicates the source current density and μ_0 represents magnetic permeability which equals $4\pi \times 10^{-7}$ H/m. A comprehensive derivation of the β parameter and fractional diffusion modeling was given by Ge (2014), Everett (2009), and Weiss et al. (2007). An abbreviated version of the mathematical development for anomalous diffusion is included in Appendix A.

2.2.6 Fracture Detection in Formation

We can detect the existence of micro-fractures in the formation using numerical EM simulations. Our background resistivity value (at $\beta = 0$) can be estimated using conventional resistivity models. In this chapter we used the Dual-Water model, and assumed the following parameters for our carbonate and organic shale cases listed in Table 2.1, where a, m, and n are adjustable model parameters.

Table 2.1 – Parameters used in Dual-Water Model for carbonate and synthetic organic shale cases. Modified from Chi et. al, 2014.

Variable	Carbonate	Synthetic Organic Shale
a	1.3	0.9
m	2.47	1.70
n	2	2
Volumetric Concentration of Shale, Csh	0.045	0.90
Connate Water Resistivity, Rw	0.034	0.034
Clay Bound Water Resistivity, Rwb	3.00	3.00
Total Water Saturation, Swt	100%	100%

We then simulated the effects of increasing fracture density by perturbing our geologic roughness parameter by 0.01 from $\beta = 0$ to $\beta = 0.4$ using conductive fractures filled with brine water. A maximum value of $\beta = 0.4$ was chosen based on minimum resistivity convergence and error analysis from the experimental data. The simulations were performed for two synthetic cases, a carbonate and a synthetic organic shale formation. A detailed explanation of these cases is presented below in Synthetic Example No. 1 and 2. Figure 2.5 below shows results from these cases.

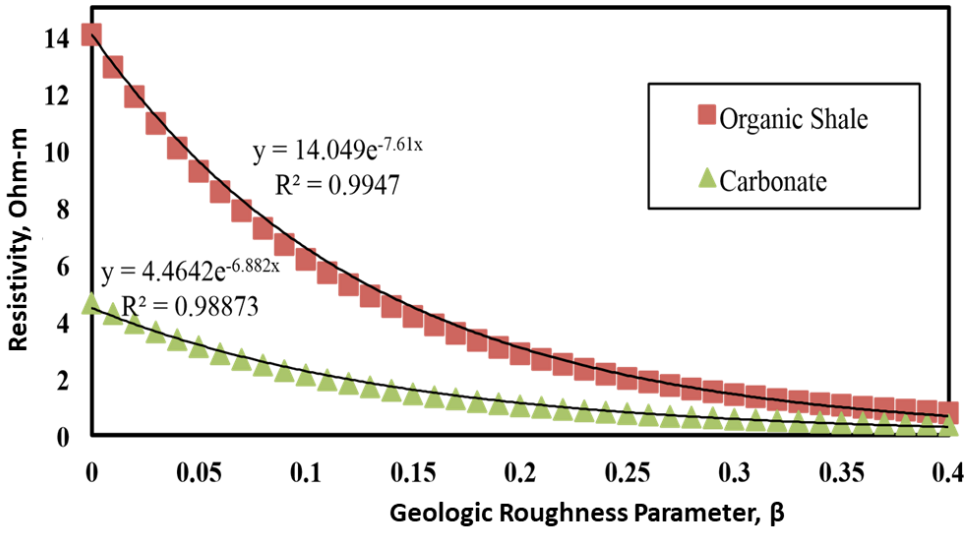

Figure 2.5 – Simulated resistivity for the synthetic cases with a beta value perturbation of 0.01 and an operating frequency of 1000 Hz. Reprinted with permission from Chi et. al, 2014.

We begin to see convergence of minimum resistivity values for both cases at β = 0.4. This phenomenon is generated by dominating conductive mico-fracture density in the formation. Formation resistivities for beta values greater than 4 are almost entirely subject to micro-fracture conductivity instead of conductivity generated by original formation porosity. As fracture density increases from β = 0.01 to β = 0.4 we see an increasing concentration of micro-fractures. However, when beta values are below 0.01 they can be neglected for fracture density analysis, as resistivity from these parameters typically correspond to numerical error.

Next, we derived an empirical relation relating β and total formation porosity to apparent formation resistivity. We estimated the total formation porosity using NMR measurements, and the apparent resistivity using a representation of induction log

response. Our representation of measured apparent resistivity was computed using pore-scale simulations of electrical rock resistivity.

2.2.7 Error Analysis for EM Simulations

We performed an error analysis for EM simulations, convergence, and variation in operating frequency. Errors for EM simulations were less than 3.5% in the Carbonate case and less than 0.04% for the Organic Shale case. Next, we calculated error in the convergence models (Figure 2.6). This resulted in an error of less than 2.1%. Then we computed error for operating frequencies ranging from 100 Hz to 1000 Hz. For these frequencies, we observed an average approximate error of 2.7%.

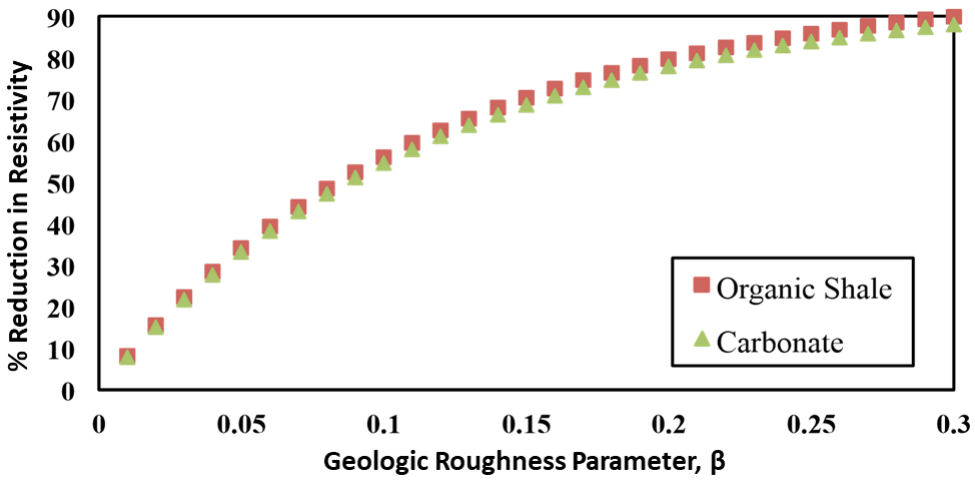

Figure 2.6 – Reduction in resistivity from background resistivity values for synthetic cases with a beta value perturbation of 0.01 and an operating frequency of 1000 Hz. Reprinted with permission from Chi et. al, 2014.

2.3 Synthetic Cases

2.3.1 Carbonate Formation with Different Density of Micro-Fractures

Synthetic Example No. 1 is designed to investigate the reliability of our proposed fracture density estimation method in fractured carbonate formations. The five synthetic carbonate cases in this example contain 2, 4, 6, 8, and 10 planar fractures, respectively. The micro-fractures are square and planar shape, with thickness of 9 μm and length of 270 μm. Figure 2.7 shows the comparison of these three synthetically fractured carbonate cases.

We simulated the apparent resistivity, R_a, for each rock sample using our pore-scale numerical simulator. We can also obtain the total resistivity, ϕ_t, using NMR measurement. Then we insert R_a and ϕ_t into the empirical relationship to estimate β value for each rock sample. The resulting β values displayed a strong relationship to the number of fractures in the formation, as shown in Figure 2.8. We increased the fracture volume percent by adding planar microfractures, with a thickness of 9 μm, from 0 fractures to 10 fractures in increments of 2. The results indicated a proportional increase in percent micro-fracture volume with our waiting time distribution parameter describing geologic roughness. Figure 2.9 below displays this correlation.

Figure 2.10 shows the simulated NMR T_2 distribution for these artificially fractured carbonate rock samples, and the corresponding analytical T_2 modes estimated from the simulated T_2 distribution. We attributed the T_2 peaks at 215~242 msec to the existence of planar fractures, which can be verified by the β factor from EM responses, and by NMR numerical simulations. We then calculated the real micro-fracture density

using Equation 2.2, and further estimated the fracture thickness using Equation 2.4. Table 2.2 lists the pore and fracture T_2 modes obtained from T_2 distributions, the estimated/real micro-fracture density and relative error, the simulated beta values from EM responses, the estimated inter-granular porosity, and the estimated/real micro-fracture thickness and relative error for all five rock samples. We observed that with higher concentration of micro-fractures, the fracture density estimates from NMR analytical model are more accurate.

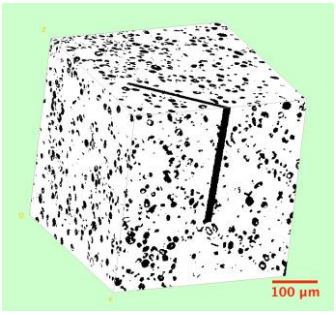

Case A

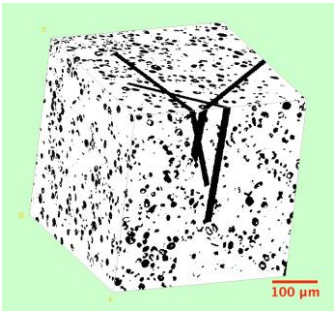

Case B

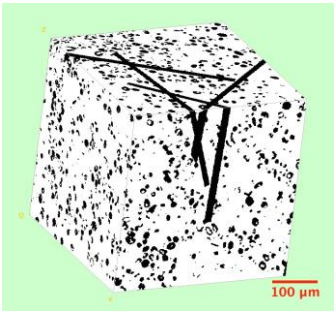

Case C

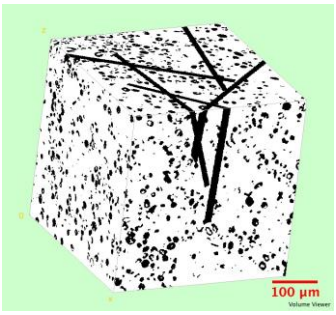

Case D

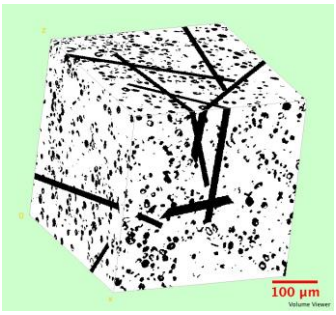

Case E

Figure 2.7 – Pore-scale images of three cases of fractured carbonate rock samples with different amount of planar fractures. The numbers of micro-fractures for Case A to E are 2, 4, 6, 8, and 10, respectively. The square planar fractures are 9 µm in thickness, and 270 µm in length for all cases. The white and black regions represent the rock grains and pore space, respectively. Reprinted with permission from Chi et. al, 2014.

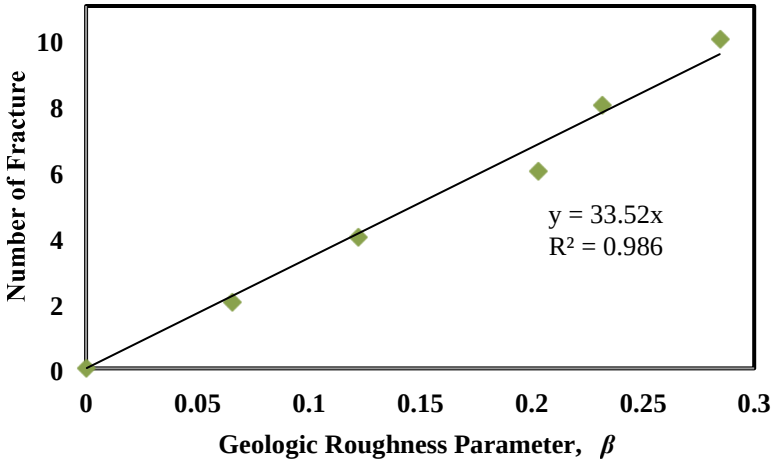

Figure 2.8 – Effect of increased fracture concentration on beta value for a carbonate rock with 9 µm thick planar fractures. Reprinted with permission from Chi et. al, 2014.

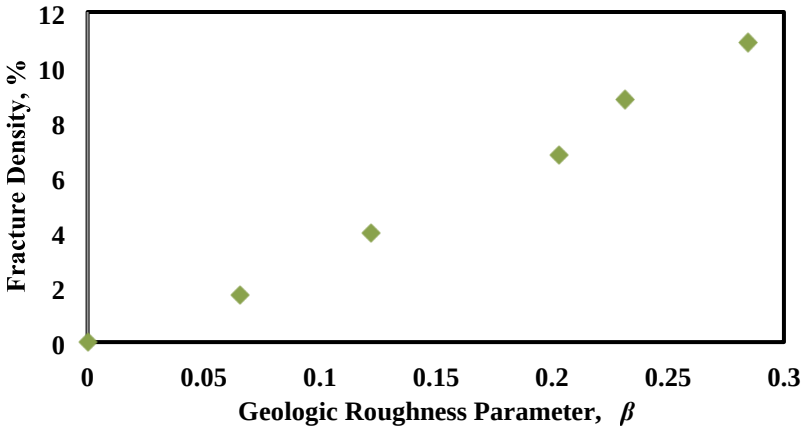

Figure 2.9 – Fracture density and beta value for a carbonate rock with varying numbers of 9 µm thick planar fractures. Reprinted with permission from Chi et. al, 2014.

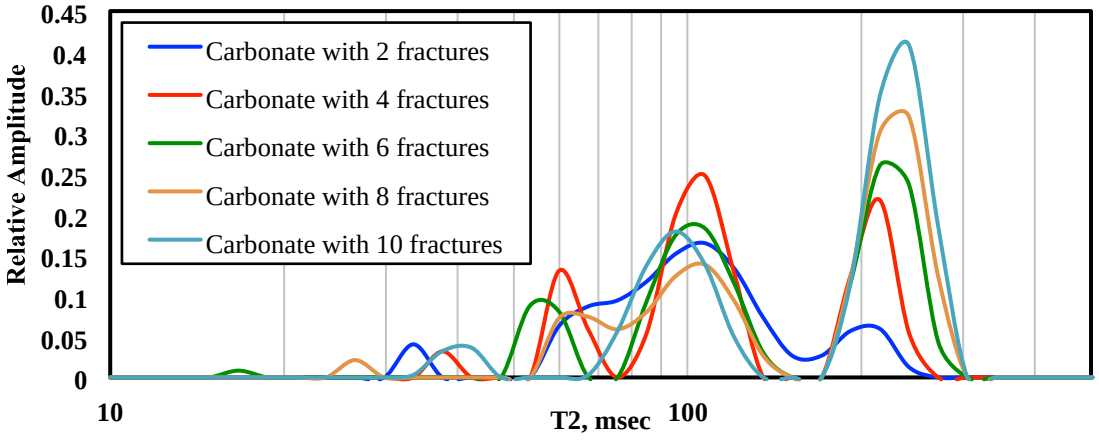

Figure 2.10 – Simulated T_2 distributions for the carbonate rock sample including square planar fractures with thickness (w) of 9 µm, and length (L) of 270 µm. The blue, red, green, yellow, and cyan lines show NMR T_2 distributions of carbonate rock sample with 2, 4, 6, 8, and 10 planar fractures, respectively. Reprinted with permission from Chi et. al, 2014.

Table 2.2 – Carbonate rock samples: NMR T_2 values for coupled pores and fractures, estimated and real fracture density and its relative error, estimated value from EM responses, estimated inter-granular porosity, estimated and real fracture thickness and its relative error, for synthetic example No. 1. Modified from Chi et. al, 2014.

Variable	Case A	Case B	Case C	Case D	Case E
Carbonate Pore T_2, msec	107.2	107.2	107.2	107.2	95.46
Coupled Fracture T_2, msec	215.4	215.4	215.4	242	242
NMR Estimated Fracture Density, %	1.08	3.01	4.96	7.2	9.44
EM Estimated Fracture Density	2.39	4.46	7.41	8.46	10.39
% Real Fracture Density, %	1.74	3.99	6.79	8.82	10.89
NMR Relative Error in Fracture Density, %	-38.02	-24.72	-26.9	-18.38	-13.33
EM Relative Error in Fracture Density	37.46	11.85	9.08	-4.09	-4.58
% Geologic Roughness Parameter, β	0.065	0.122	0.203	0.232	0.285
Estimated Inter-granular Porosity, %	16.2	16.69	17.53	17.32	17.15
Estimated Fracture Thickness, µm	8.79	8.87	9.1	10.25	10.43
Real Fracture Thickness, µm	9	9	9	9	9
Relative Error in Fracture Thickness, %	-2.37	-1.43	1.08	13.9	15.84

2.3.2 Carbonate Formation with Micro-Fractures of Different Thickness

The three synthetic carbonate cases in this example contain planar fractures of different thickness. The square planar fractures are 270 μm in length, and 2 fractures are included in each case. The fracture thickness for Case A, B, and C are 9 μm, 12 μm, and 15 μm, respectively. Figure 2.11 shows the comparison of these three artificially fractured carbonate cases. Figure 2.12 shows the simulated NMR T_2 distribution for these fractured carbonate rock samples. We attributed the T_2 peaks at 215, 242, and 305 msec to the existence of planar fractures. We then calculated the real micro-fracture density using Equation 2.2, and further estimated the fracture thickness using Equation 2.4. Table 2.3 lists the pore and fracture T_2 modes obtained from T_2 distributions, the estimated/real micro-fracture density and relative error, the estimated inter-granular porosity, and the estimated/real micro-fracture thickness and relative error for all three cases. Furthermore, we found that β factor estimated from EM responses doesn't show a proportional relationship with the fracture thickness, i.e. the β factor is not explicitly sensitive to variation of fracture thickness.

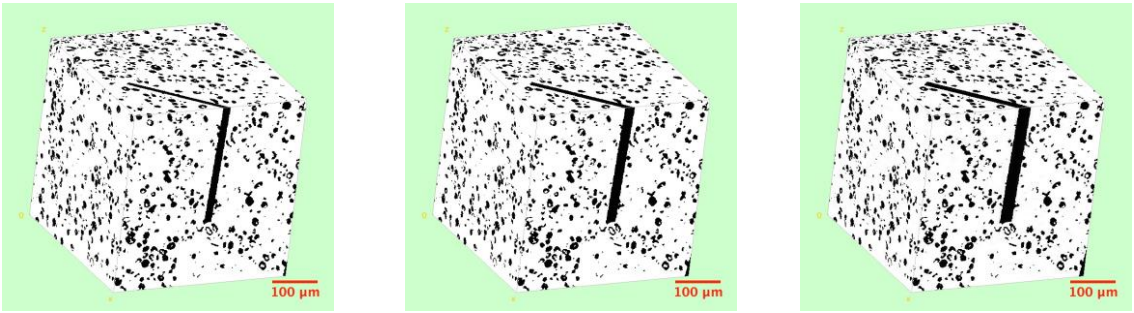

Case A Case B Case C

Figure 2.11 - Pore-scale images of three cases of fractured carbonate rock samples with different thickness of fractures. The fracture thickness for Case A, B, and C are 9 µm, 12 µm, and 15 µm, respectively. The square planar fractures are 270 µm in length, and the number of fractures is 2 for all cases. The white and black regions represent the rock grains and pore space, respectively. Reprinted with permission from Chi et. al, 2014.

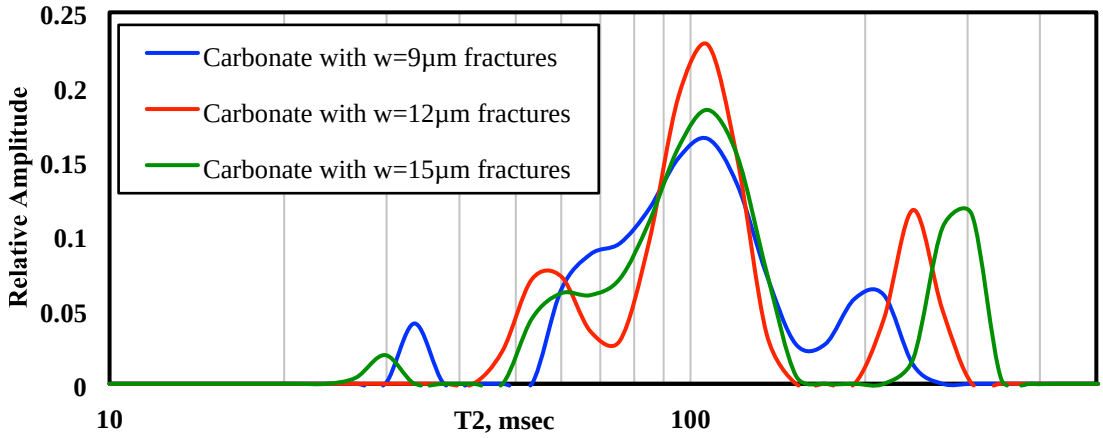

Figure 2.12 - Simulated T_2 distributions for the carbonate rock sample including planar fractures with length (L) of 270 µm and different thickness. The blue, red, and green lines show NMR T_2 distributions of carbonate rock sample with planar fractures of 9-µm, 12-µm, and 15-µm thickness, respectively. Reprinted with permission from Chi et. al, 2014.

Table 2.3 - Carbonate rock sample: NMR T_2 values for coupled pores and fractures, estimated and real fracture density and its relative error, estimated inter-granular porosity, estimated and real fracture thickness and its relative error, for synthetic example No. 1. Modified from Chi et. al, 2014.

Variable	Case A	Case B	Case C
Carbonate Pore T_2, msec	107.2	107.2	107.2
Coupled Fracture T_2, msec	215.4	242	305.3
Estimated Fracture Density, %	1.08	1.74	2.3
Real Fracture Density, %	1.74	2.32	2.9
Relative Error in Fracture Density, %	-38.02	-24.99	-20.76
Estimated Inter-granular Porosity, %	16.36	16.28	16.3
Estimated Fracture Thickness, µm	8.78	9.94	12.83
Real Fracture Thickness, µm	9	12	15
Relative Error in Fracture Thickness, %	-2.39	-17.2	-14.47

2.3.3 Synthetic Organic Shale Formation with Micro-Fractures of Different Thickness

The purpose of this synthetic case is to test the reliability of our introduced fracture density estimation method in fractured organic shale formations. The three synthetic organic shale cases in this example contain planar fractures of different thickness. The square planar fractures are 135 µm in length, and 2 fractures are included in each case. The fracture thickness for Case A, B, and C are 1.5 µm, 4.5 µm, and 7.5 µm, respectively. Figure 2.13 shows the comparison of these three artificially fractured carbonate cases. Figure 2.14 shows the simulated NMR T_2 distribution for these fractured carbonate rock samples. We attributed the T_2 peaks at 17.5, 53, and 82 msec to the planar fractures. We then calculated the real micro-fracture density using Equation 2.2, and further estimated the fracture thickness using Equation 2.4. Table 2.4 lists the

pore and fracture T_2 modes obtained from T_2 distributions, the estimated/real micro-fracture density and relative error, the estimated inter-granular porosity, and the estimated/real micro-fracture thickness and relative error for all three cases. Again, we estimated β factor from EM responses, however, we still observed minimal sensitivity to change in fracture thickness. Thus, there is no explicit relationship between β factor and fracture volume in this case.

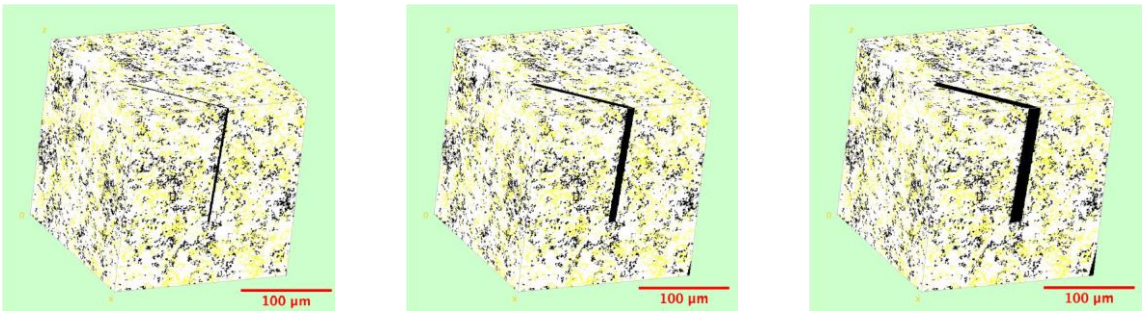

Case A Case B Case C

Figure 2.13 - Pore-scale images of three cases of fractured organic shale rock samples. The fracture thickness for Case A, B, and C are 1.5 µm, 4.5 µm, and 7.5 µm, respectively. The square planar fractures are 135 µm in length, and the number of fractures is 2 for all cases. The yellow, white, and black regions represent the kerogen, rock matrix, and pore space, respectively. Reprinted with permission from Chi et. al, 2014.

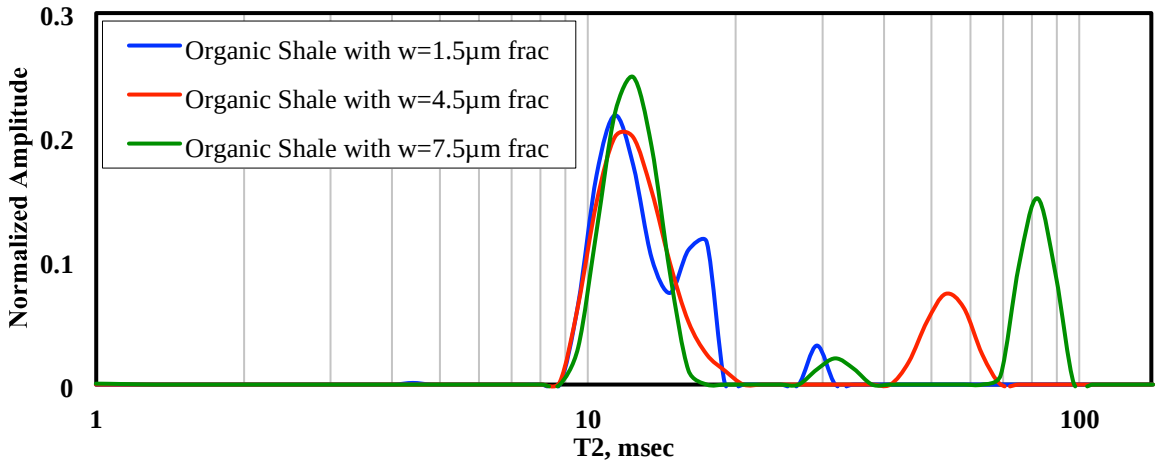

Figure 2.14 - Simulated T_2 distributions for the synthetic organic shale sample including planar fractures with thickness (w) of 1.5, 4.5, or 7.5 µm, and length (L) of 135 µm. The blue, red, and green lines show NMR T_2 distributions of organic shale matrix with planar fractures of 1.5-µm, 4.5-µm, and 7.5-µm thickness, respectively. Reprinted with permission from Chi et. al, 2014.

Table 2.4 - Synthetic organic shale sample: NMR T_2 values for coupled pores and fractures, estimated and real fracture density and its relative error, estimated inter-granular porosity, estimated and real fracture thickness and its relative error, for synthetic example No. 2. Modified from Chi et. al, 2014.

Variable	Case A	Case B	Case C
Organic Shale Pore T_2, msec	11.35	12.37	12.37
Coupled Fracture T_2, msec	17.5	53.4	82.1
Estimated Fracture Density, %	7.1	16.28	27.55
Real Fracture Density, %	6.1	18.4	30.7
Relative Error in Fracture Density, %	16.4	-11.55	-10.26
Estimated Inter-granular Porosity, %	9.9	10.21	10.31
Estimated Fracture Thickness, µm	1.52	4.69	7.33
Real Fracture Thickness, µm	1.5	4.5	7.5
Relative Error in Fracture Thickness, %	1.56	4.27	-2.24

2.4 Conclusions

Characterization of micro-fracture density in multiple-porosity systems is a challenging task that directly impacts completion designs, including placement and number of fracture treatments. NMR measurements in multiple porosity systems have been proven to show sensitivity to the existence of micro-fractures due to fracture-pore diffusional coupling effect. Electromagnetic measurements were also demonstrated as sensitive to fracture density in the formation. We proposed a new method to evaluate volumetric fractions of micro-fractures and pore space by combining the NMR theoretical model and the fractional diffusion modeling of electromagnetic measurements.

We tested the introduced method on a 3-D pore-scale carbonate image and a synthetic organic shale image, both containing artificial micro-fractures. We varied the number and thickness of micro-fractures in each case, and then estimated fracture density using combination of NMR and electromagnetic simulation results; our estimated fracture density showed agreement with the actual values, which confirmed the reliability of our method. The approach helps distinguish between variations in micro-fracture dimensions and density in multiple-porosity systems, while improving micro-fracture density estimation. This research has the potential to increase production from tight carbonate and organic-shale formations by improving our fracturing treatment designs through enhanced reservoir characterization.

CHAPTER III

MODELING ANOMALOUS ELECTROMAGNETIC DIFFUSION EFFECTS ON INDUCTION LOG RESPONSES FOR CHARACTERIZING NATURAL FRACTURE CORRIDORS*

Controlled-source electromagnetic (CSEM) methods, such as induction logging, are commonly used to measure formation resistivity in the near-wellbore region. However, near-wellbore formation damage incurred during the drilling process often obscures well logging measurements making it difficult to differentiate between natural and artificially induced fractures. Combining surface gas readings and downhole measurements with electromagnetic (EM) induction log simulations of the anomalous EM diffusion response can improve natural fracture corridor characterization and detection. Traditional characterization and detection methods depend on high-resolution resistivity imaging and conventional well logs (e.g., induction logs). High-resolution resistivity imaging mitigates fracture characterization uncertainty; however, it is costly and may be inaccurate around near-wellbore formation damage. Meanwhile, induction logs provide reliable fracture detection but lack fracture geometry sensitivity. Our novel approach combines drilling measurements, regional geomechanics, and 3-D finite-element (FE) numerical simulation of EM induction logging (via anomalous diffusion

---

* Part of this chapter is reprinted with permission from "Modeling the Effects of Anomalous Electromagnetic Diffusion on Induction Log Responses: The Next Step in Mapping Natural Fracture Corridors" by Elliott et al., 2014. SPE 170950. Copyright [2014] by Society of Petroleum Engineers.

simulation) to better describe near-wellbore induced fracture geometry and location. Thereby, improving natural fracture detection and mapping for unconventional formation completion plan optimization.

We performed FE numerical simulations to model hydraulic fracturing effects on fractured zone induction log responses. Fractured zones were specified with a geologic roughness parameter, β. Beta represents an anomalous diffusion coefficient within the generalized Ohm's law for fractured media. We then calculated apparent resistivity for resistive fractures placed inside a layered formation. This was accomplished using our in-house FE numerical simulator, *seatem*. The version of *seatem* used in this chapter is an induction logging simulator that solves the diffusive Maxwell equations and plots resulting apparent resistivity distributions within an unstructured cylindrical-cartesian conforming mesh. This improves our understanding of how the targeted zone interacts with varying stimulation factors.

We performed numerical simulations along a multi-zoned reservoir interval for three synthetic cases: a sandstone formation, a carbonate formation, and an organic shale formation. Then, we quantified hydraulic fracturing effects on induction logs and optimized fracture treatment placement. Results suggested fracture corridor depletion and geologic targeting as viable for fractured zones with β values larger than 0.3. Additionally, using the β parameter, we developed a method to high-grade natural fracture corridors to assist in hydraulic fracture placement selection. Our methodology

will improve operational decisions and increase production during field development by increasing natural fracture corridor characterization and detection accuracy.

3.1 Introduction

Unconventional reservoirs retain hydrocarbon reserves often unobtainable through classical production techniques. These formations require enhanced recovery methods to produce those remaining hydrocarbons economically. Standard enhanced recovery methods involve stimulating the rock matrix through various fracturing techniques. However, optimizing fracturing placement remains challenging in the presence of naturally fractured corridors. These high permeability zones increase hydrocarbon production through corridor depletion. However, we often require optimal perforation placement to benefit fully from hydraulic and natural fracture interaction.

Selecting natural fracture corridor stimulation locations requires accurate geomechanical parameter characterization. Some of these parameters, such as natural fracture density and geometry, are costly to obtain. Unconventional formation wells depend on low drilling and completion costs to remain profitable. Thus, operator budget constraints often prevent using specialized logging techniques, such as nuclear magnetic resonance (NMR) and high-definition resistivity imaging, required to accurately characterize geomechanical parameters. This restriction forces companies to rely on basic well-logging methods to extract fracture attributes. Our novel method provides a cost-effective solution to achieve accurate natural fracture corridor detection and

characterization by combining commonly obtained surface gas readings and downhole measurements with electromagnetic (EM) induction log simulations.

3.1.1 Natural Fracture Corridors

Natural fracture corridors are high-permeability zones created by a complex fracture network with varying spatial distribution and conductivities (Ahmed, 2010). These areas typically display a dominant fracture orientation containing a high storativity ratio and a low interporosity flow coefficient. Their parameters provide easier storage and fluid transfer from the matrix to fissures. Additionally, some shale resource plays production, for example the North Dakota Bakken shale, are geologically dominated by natural fracture corridor depletion (Anderson, 2011). Accurately predicting corridor locations and attributes is necessary for field development during infill drilling. Correctly detecting and characterizing these locations remains challenging without heavy formation evaluation investment through specialized logging techniques. Numerical EM simulation of induction log responses provide an alternative economical approach. EM simulations can quantify the degree of heterogeneity within natural fracture corridors by calculating a geologic roughness parameter, β.

3.1.2 Geologic Roughness Parameter

We assume subsurface formation fracture density, i.e. geologic "roughness," can be specified with an isotropic scalar β parameter. This parameter represents charge carrier fractal transport within a geometry whose heterogeneities obey a spatial power

law density distribution. We associate β with the statistical behavior of charge carrier random walk through a disordered medium. Beta describes the non-Gaussian step-length distribution function in a continuous time random walk (CTRW) algorithm. Lower β values indicate shorter step lengths and smaller fracture concentration, while higher β values associate with longer step lengths and an increased concentration of large through-going fractures. Sher and Montroll (1975) originally presented the CTRW approach to electric charge transport. Their applications to induction logging are discussed in Bray (2013).

During induction logging, the tool's transmitter creates an electromagnetic field. This field diffuses out in a classical Brownian motion for an idealized homogeneous formation. We attribute a β value equal to zero for this scenario. However, fractured formations often exhibit spatial heterogeneity characterized by power law distributions. In such cases, the electromagnetic field undergoes anomalous diffusion as it propagates into the surrounding rock. Thus, the formation β value increases with reservoir fracture density. This β parameter is defined within the electromagnetic field solution for a convolutional vector diffusion equation. Everett (2009) derived the governing fractional Maxwell equation based on the time-convolutional form of Ohm's Law. The time-derivative of the generalized Ohm's law is given by (Eq. 1):

$$\frac{\partial}{\partial t}\sigma_\beta * E = \frac{\sigma_\beta}{\Gamma(\beta)}\frac{\partial}{\partial t}\int_0^t \frac{dt'\mathrm{E}(t)}{(t-t')^{1-\beta}} = \sigma_{\beta 0} D_t^{1-\beta} E(t) \tag{3.1}$$

where σβ is a generalized conductivity, E is the electric field, β is the geologic roughness parameter, $Dt^{1-\beta}$ is the fractional derivative, and Γ is the normalizing constant Gamma function. The fractional diffusion equation compact form can be written as:

$$\nabla\times\nabla\times\mathrm{E} = -\mu_0\sigma_{\beta 0}D_t^{1-\beta}E(t) - \mu_0\frac{\partial}{\partial t}J_s \tag{3.2}$$

where Js represents the source current density and $\mu_0=4\pi\times10\text{-}7$ H/m is the magnetic permeability of free space. Ge (2014), Everett (2009), and Weiss et al. (2007) provide a detailed derivation of the fractional diffusion equation. An abbreviated version of the mathematical development for anomalous diffusion is included in Appendix A.

3.1.3 Natural Fracture Detection and Characterization

We propose a new methodology to locate and high-grade natural fracture corridors for optimizing hydraulic fracture placement. Our approach uses available induction logging data combined with other surface and downhole measurements, such as surface-gas reading and offset well fracture pressure data. Norbeck (2012) proposed a similar methodology by combining mud log total gas concentration measurements with mud pit volume. We modified Norbeck's method by including EM induction log response simulations. This improves the accuracy for locating natural fracture corridor boundaries. Previous work in simulated EM borehole measurements is found in Bespalov (2009) and Pardo (2007). Our EM induction logging simulator differs from

Bespalov and Pardo by providing natural fracture corridor representation through a β parameter. This aids in selecting fracture treatment placement to maximize stimulated reservoir volume. We describe our methodology for simulating hydraulic fracturing effects on induction log responses in the following section.

3.2 Method

We optimized hydraulic fracture placement through mapping natural fracture corridors. We used regional geomechanics and surface-gas measurements to define natural fracture locations and corridor boundaries. Dominant fracture orientation was then determined within the fractured zone using surficial basement lineaments, following the approach presented by Anderson (2011). Next, EM logging simulations were used to high-grade the fracture corridor for fracture density. After high-grading, modeling hydraulic fracture interactions with the natural fracture zone was used to optimize stimulation placement. The project workflow is illustrated in Figure 3.1. A detailed description of each process is presented in the following sections.

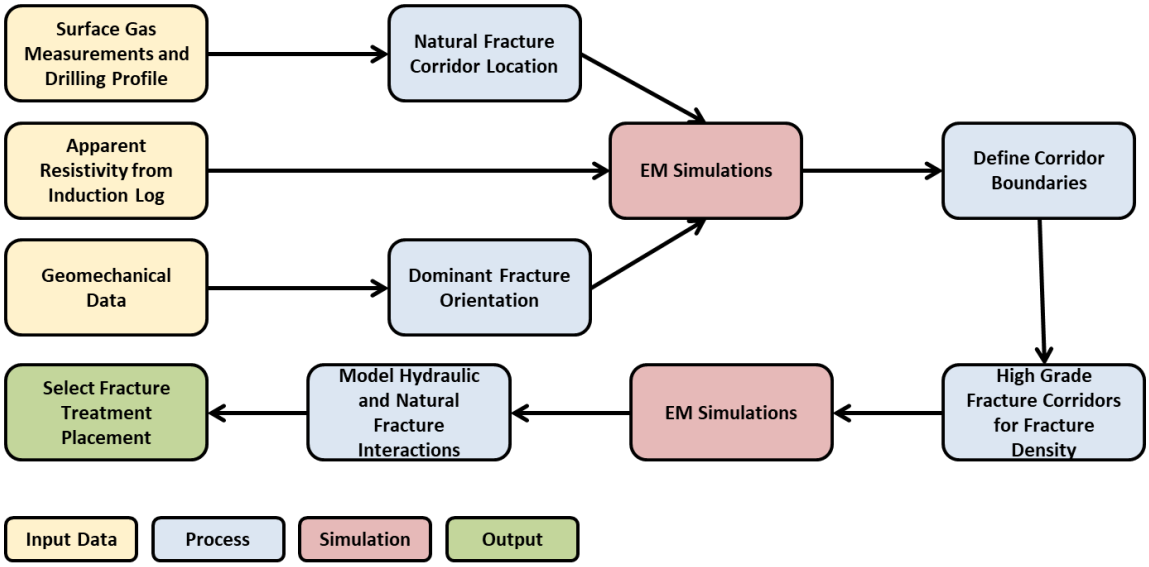

Figure 3.1 – Workflow for selecting fracture treatment placement. Reprinted with permission from Elliott et. al, 2014.

3.2.1 Mapping Natural Fracture Location

The initial natural fracture corridor location was selected using surface-gas readings. Sustained gas measurement spikes generally correlate to high permeability zones during underbalanced drilling (i.e., the Bakken Shale). These spikes indicate gas coming out of solution corresponding to fracture corridors. We then redefined the fracture location using EM logging simulations. Our FE EM simulator, *seatem*, solves the governing fractional-diffusive Maxwell equations formulated as secondary Coulomb-gauge electromagnetic potentials. Next, it calculates 3-D heterogenous electrical conductivity distributions on a tetrahedral mesh. We developed a cylindrical-cartesian conforming mesh for the research in this chapter. The mesh is cylindrical in the near-wellbore region and transitions to cartesian in the far-field by projecting nodes outward from each cylindrical region. Our mesh design includes fine meshing around the

wellbore to more accurately represent the primary field, as high gradients are often present near the source. An example of the mesh design is presented in Figure 3.2. We then generate synthetic induction logs for multi-layered formations and interpreted these new logs to map the natural fracture location.

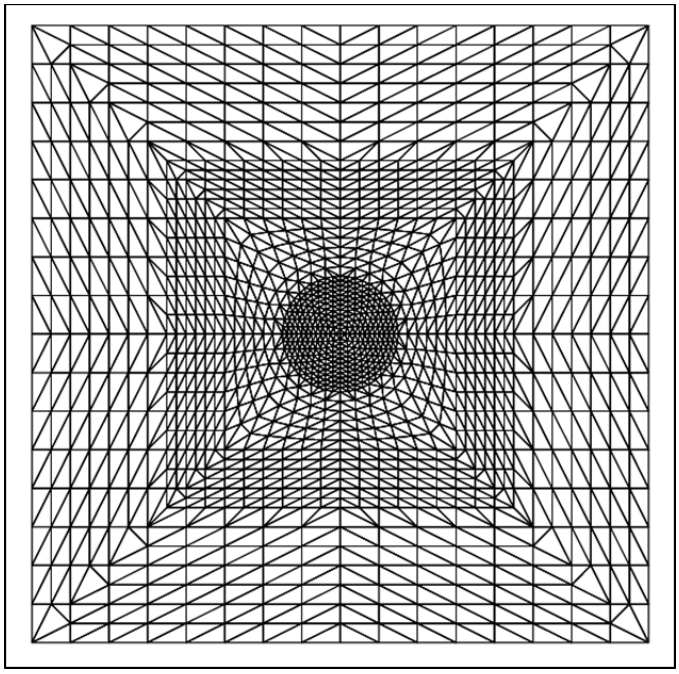

Figure 3.2 – Cylindrical-cartesian conforming mesh design viewed along the borehole.

3.2.2 Determining Dominant Fracture Orientation

We determined dominant fracture orientation with regional geomechanics and available seismic data. Since the methodology varies by region, the focus of this chapter is limited to the Bakken Shale of North Dakota and Canada. The liquids-rich Bakken formation of the Williston basin is a North American Plate interior intracrationic basin.

Since deposition, between the Upper Devonian and Lower Mississippian eras, the Bakken formation remained uninfluenced by tectonic activity. Despite this, it is fractured with the highest hydrocarbon production correlating to higher fracture densities. Moreover, higher fracture density areas occur in roughly linear arrangements defined as fractured lineaments. Anderson (2011) attempts to determine these fracture alignments origins. Anderson found the Precambrian basement contained extensive normal faulting by interpreting 2-D seismic data from Montrail County, ND. These faults extended upward through the overlying strata before tipping out. Despite tipping out, strain accumulation continued above the tip. Rather than macroscopic faulting, a more distributed linear region of fractured rock accommodates strain. Moreover, fractured lineaments within the Willison Basin occurred in two roughly orthogonal orientations. Surficial lineaments orientation is comparable to basement lineaments. Therefore, we inferred the Bakken lineaments likely orient similarly. We then correlated high permeability zones along different wellbores using orientations observed in basement and surficial lineaments. This is just one approach to determining dominant fracture orientation. The particular method to use varies with geological location and is typically well established for the region.

3.2.3 Defining and High Grading Fracture Corridors for Fracture Density

We high-graded natural corridors based on fracture concentration. Zones with higher fracture concentration were assigned a higher β value. Then, using *seatem*, estimated β effects on conductive and resistive fractures electromagnetic response were

obtained. The electromagnetic response represented apparent resistivity measured by a standard 4-meter length 1 kHz coaxial induction tool. Conductive fractures typically correspond to brine-filled fractures, while resistive fractures generally correlate to hydrocarbon-filled fractures. The matrix was assumed to be low-resistivity sandstone, moderate-resistivity carbonate, or high-resistivity organic shale. We selected initial β values based on the methods previously described in chapter two. Then, β was perturbed from β = 0 to β = 0.4 with a 0.01 step size to model conductive and resistive fracture effects on apparent conductivity. The results are shown in Figure 3.3. Resistivity decreases exponentially with increasing β for all three conductive fractures cases. This indicates a shift from classical to anomalous diffusion. The inverse response was observed for resistive fractures.

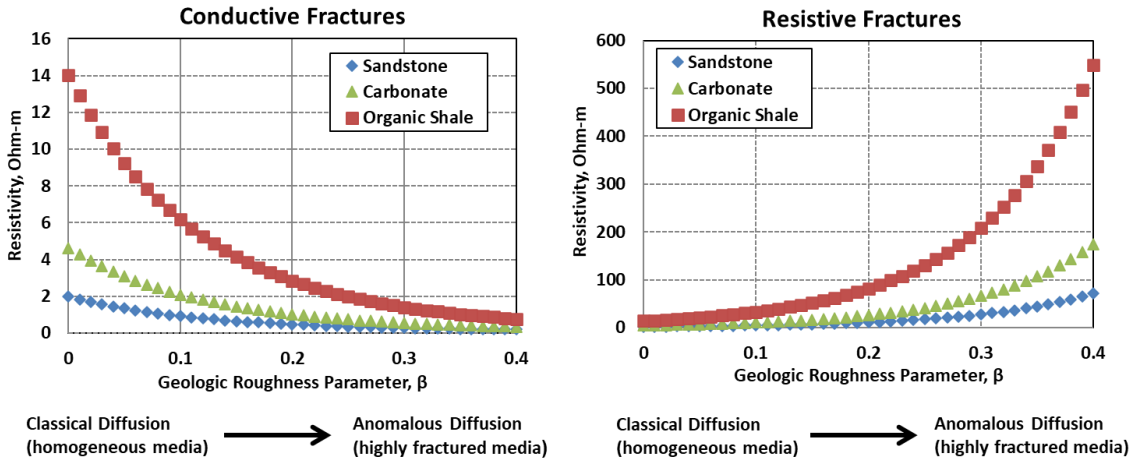

Figure 3.3 – Geologic roughness effects on conductive and resistive fractured zone apparent resistivity. Modified from Elliott et. al, 2014.

We used *seatem* to determined qualitative fracture density to estimate the geologic roughness parameter along the corridor. The fracture corridor was then partitioned into equally sized zones and compared with β parameter values. Zones with higher β values indicated increased fracture density. Minimum and maximum β values, as well as area, were then calculated to select optimal fracture treatment placement. We calculated minimum and maximum β by plotting corridor zone resistivities from Figure 3.3. While area was approximated by numerically integrating each zone using the trapezoidal rule.

3.2.4 Modeling Hydraulic and Natural Fracture Interactions

We modified the numerical logging simulator to calculate induction log response effects for hydraulic and natural fracture interactions. The modified program models a discrete 3-D hydraulic fracture embedded within the tetrahedral mesh (Figure 3.4).

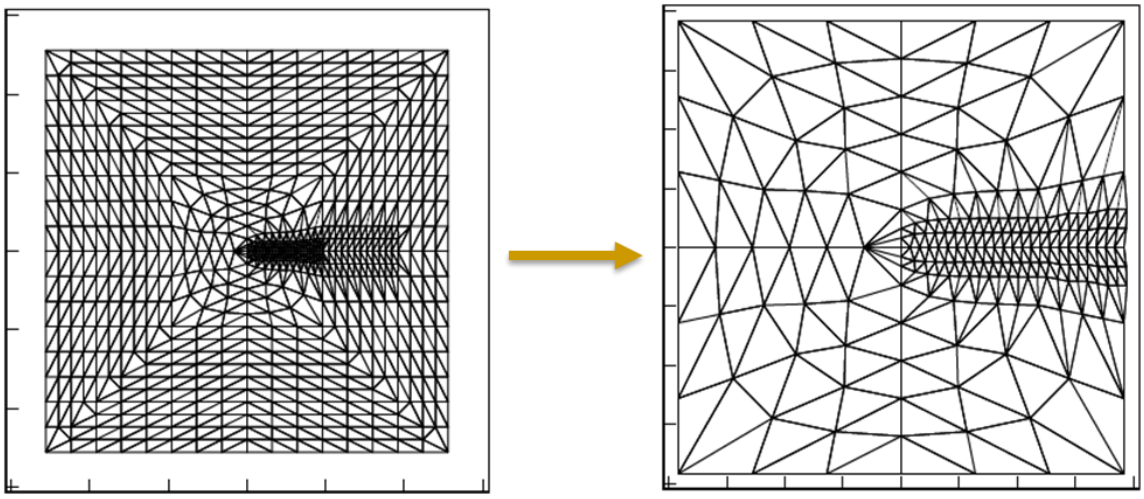

Figure 3.4 – Tetrahedral meshing for the horizontal slice of a hydraulic fracture (left), mesh enlarged 3 times (right).

Parameters including conductivity, length, width, height along the wellbore, location along the wellbore, and orientation were used to define the fracture. The hydraulic fracturing properties were selected based on the work of Hibbs (2014). These properties included a hydraulic fracture area of 20000 m^2 and a conductance (conductivity-thickness product) of 1.5 S. We then inserted this hydraulic fracture into our simulator to model hydraulic and natural fracture interactions. After modeling, we can better optimize fracturing stimulation placement based on the interactions between hydraulic and natural fractures. We then selected the surrounding reservoir properties and ranked the natural fracture corridor with β values. Fracturing treatment effects on induction log responses could then be modeled with and without the effects of natural fractures.

3.2.5 Optimizing Hydraulic Fracture Placement

We partitioned the newly defined fracture corridors into equal length zones along the wellbore and selected the fracture zones with largest β values and area. Then, we modeled the interactions between fracture treatments and our natural fracture corridor using *seatem* with the β values as input parameters. These results aided in determining the most favorable zone for optimizing hydraulic fracture placement. Our methodology was applied to a comprehensive suite of synthetic case studies. Three of these cases are described in the following section.

3.3 Synthetic Cases

We selected three synthetic cases to present: a sandstone formation, a carbonate formation, and an organic shale formation. Each case consists of a 6-layered earth model with relative depths and varying conductivities. The fracture corridor was then identified and partitioned into an arbitrary number of zones based on resistivity. We determined fracture corridor location with surface-gas measurements and regional geomechanics. Next, we applied our methodology to each case to show results for anomalous diffusion calculations, hydraulic and natural fracture interactions, and optimal fracture treatment placement. Tables 3.1-3.3 provide anomalous diffusion calculations for β values and area, while generated induction logs display fracture interactions and optimization. Results for each case are detailed below.

3.3.1 Synthetic Case No. 1: Sandstone Formation

The first case is a sandstone formation with the highest fracture concentration located in the fracture corridor center. The formation contains a 6-layered earth model with 1.97 Ohm-m non-fractured resistivity, and fractured zone resistivities ranging between 6.99 Ohm-m to 64.94 Ohm-m (Figure 3.5, left). We partition this model's fracture corridor into 8 equally spaced zones and display its generated induction log (Figure 3.5, right). The β values and area calculations are given in Table 3.1. Zone 5 was determined to be the most favorable fracture treatment placement location. This zone gives the largest area and highest β values combination.

Next, we insert a 20000 m^2 hydraulic fracture with a 1.5 S conductivity into zone 5 at a relative depth of 1.9 m. Simulation results for the hydraulic fracture's interaction with natural fractures are shown as a generated induction log in Figure 3.6 (left). Zone 5 (Figure 3.6, right) resulted in a 0.4% induction log signature reduction after hydraulic fracture placement. This indicates a poor hydraulic fracturing response for zone 5. Therefore, the zone is determined to not be viable for geologic targeting and corridor depletion.

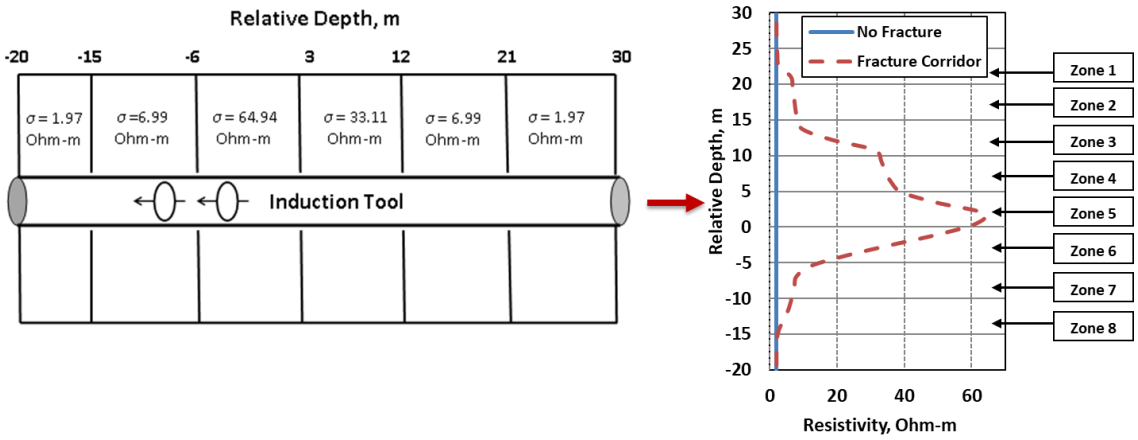

Figure 3.5 – Layered earth model for sandstone formation case (left), generated natural fracture corridor induction log (right). Modified from Elliott et. al, 2014.

Table 3.1 - Fractured zone β values and area for sandstone formation. Modified from Elliott et. al, 2014.

Zone	Min β	Max β	Area, ohm-m2
Zone 1	0.164	0.140	19.92
Zone 2	0.140	0.166	37.57
Zone 3	0.166	0.318	93.24
Zone 4	0.318	0.340	175.10
Zone 5	0.340	0.396	182.99
Zone 6	0.235	0.385	182.38
Zone 7	0.138	0.235	43.89
Zone 8	0.030	0.138	23.37

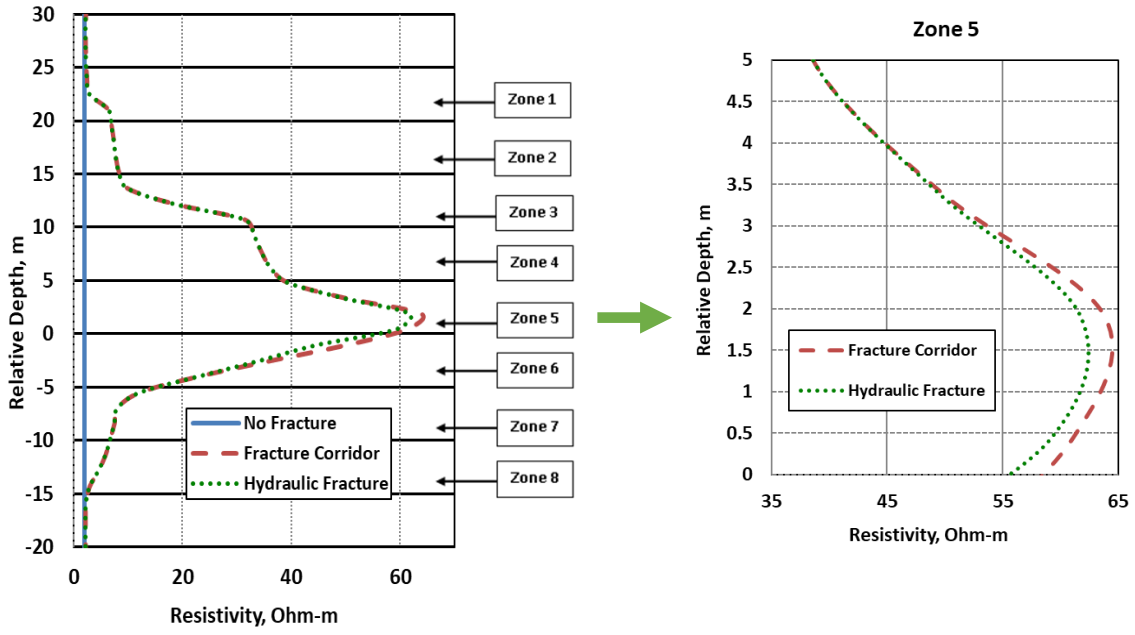

Figure 3.6 – Generated induction log for hydraulic and natural fracture interactions in sandstone formation case. Modified from Elliott et. al, 2014.

3.3.2 Synthetic Case No. 2: Carbonate Formation

Our second case, a carbonate formation, shows the highest fracture concentration on the left side of the fracture corridor. The formation contains a 6-layered earth model with 4.46 Ohm-m non-fractured resistivity, and fractured zone resistivities ranging between 5.93 Ohm-m to 175.44 Ohm-m (Figure 3.7, left). We partition this model's fracture corridor into 8 equally spaced zones and display its generated induction log in Figure 3.7 (right). The β values and area calculations are reported in Table 3.2. We determined zone 2 as the optimal fracture treatment placement location. This zone gives the largest area and highest β values combination.

Next, we insert a 20000 m^2 hydraulic fracture with a 1.5 S conductivity into zone 2 at a relative depth of 18.1m. Simulation results for the hydraulic fracture's interaction with natural fractures are shown as a generated induction log in Figure 3.8 (left). Zone 2 (Figure 3.8, right) results in a 23.9% induction log signature reduction after hydraulic fracture placement. Hydraulic fracturing response improved by 5875% from the sandstone formation case. Zone 2 is determined to be a viable geologic targeting and corridor depletion location.

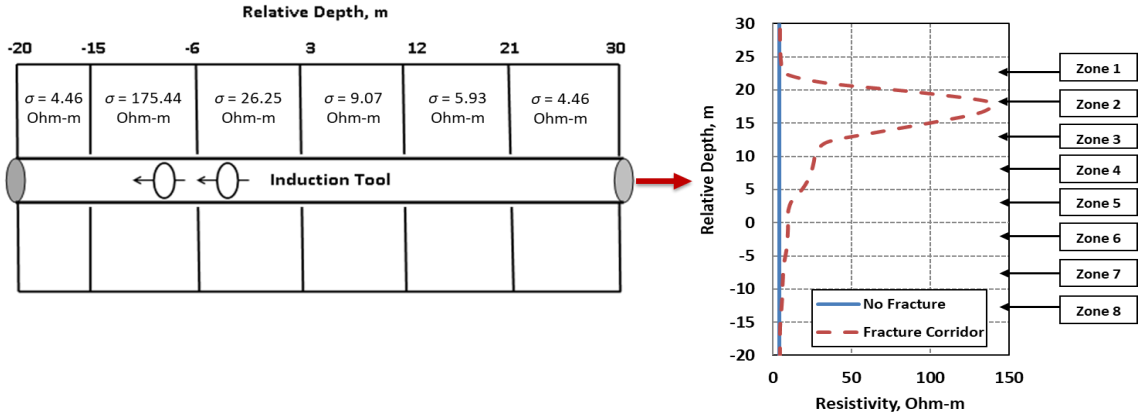

Figure 3.7 – Layered earth model for carbonate formation case (left), generated natural fracture corridor induction log (right). Modified from Elliott et. al, 2014.

Table 3.2 - Fractured zone β values and area for carbonate formation. Modified from Elliott et. al, 2014.

Zone	Min β	Max β	Area, ohm-m2
Zone 1	0.001	0.316	102.56
Zone 2	0.316	0.387	597.16
Zone 3	0.199	0.345	252.75
Zone 4	0.157	0.199	116.48
Zone 5	0.084	0.157	60.49
Zone 6	0.062	0.084	38.08
Zone 7	0.032	0.062	34.03
Zone 8	0.006	0.032	28.09

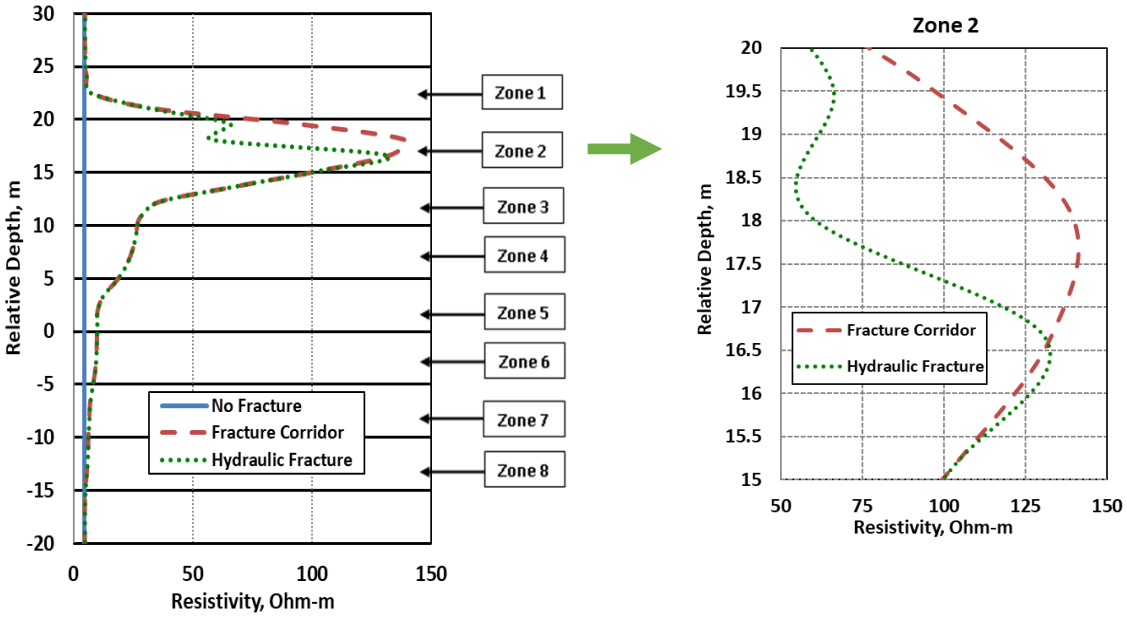

Figure 3.8 – Generated induction log for hydraulic and natural fracture interactions in carbonate formation case. Modified from Elliott et. al, 2014.

3.3.3 Synthetic Case No. 3: Organic Shale Formation

Our third case, an organic shale formation, shows the highest fracture concentration in the fracture corridor sides. The formation contains a 6-layered earth model with 14.04 Ohm-m non-fractured resistivity, and fractured zone resistivities ranging between 28.01 Ohm-m to 555.56 Ohm-m (Figure 3.9, left). We partition this model's fracture corridor into 8 equally spaced zones and display its generated induction log in Figure 3.9 (right). The β values and area calculations are listed in Table 3.3. We determined zones 2 and 7 as viable fracture treatment placement locations. These zones give the largest area and highest β values combination.

Next, we insert a 20000 m^2 hydraulic fracture with a 1.5 S conductivity into zones 2 and 7 at relative depths of 18.1 m and -8.4 m respectively. Simulation results for the hydraulic fracture's interaction with natural fractures are displayed as a generated induction log in Figure 3.10. Zone 2 (Figure 3.11, left) results in a 45.7% induction log signature reduction after hydraulic fracture placement. While zone 7 (Figure 3.11, right) results in a 36.8% reduction. Hydraulic fracturing response improved by 11325% (zone 2) and 9100% (zone 7) from the sandstone formation case. Zones 2 and 7 were determined to be viable geologic targeting and corridor depletion locations.

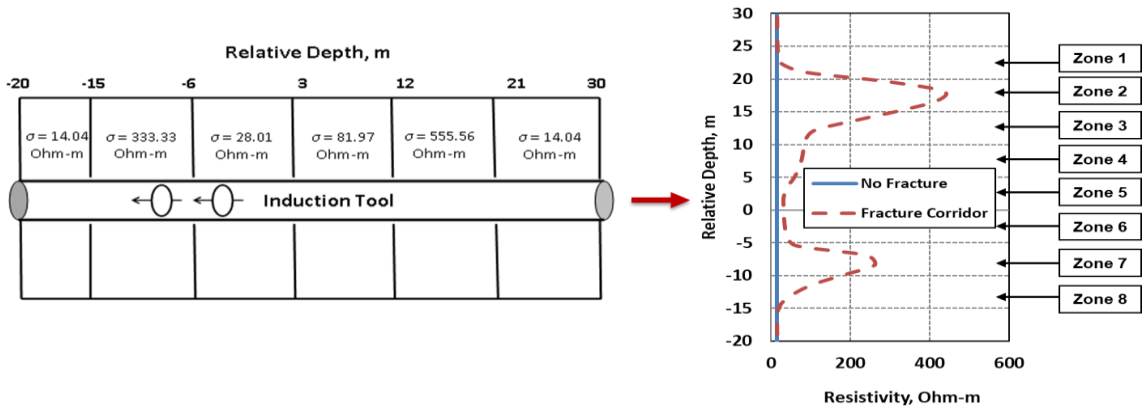

Figure 3.9 – Layered earth model for organic shale formation case (left), generated natural fracture corridor induction log (right). Modified from Elliott et. al, 2014.

Table 3.3 - Fractured zone β values and area for organic shale formation. Modified from Elliott et. al, 2014.

Zone	Min β	Max β	Area, ohm-m2
Zone 1	0.009	0.314	287.84
Zone 2	0.314	0.382	1875.76
Zone 3	0.198	0.344	788.64
Zone 4	0.156	0.198	364.93
Zone 5	0.086	0.156	141.10
Zone 6	0.086	0.152	180.06
Zone 7	0.152	0.325	969.88
Zone 8	0.038	0.282	383.46

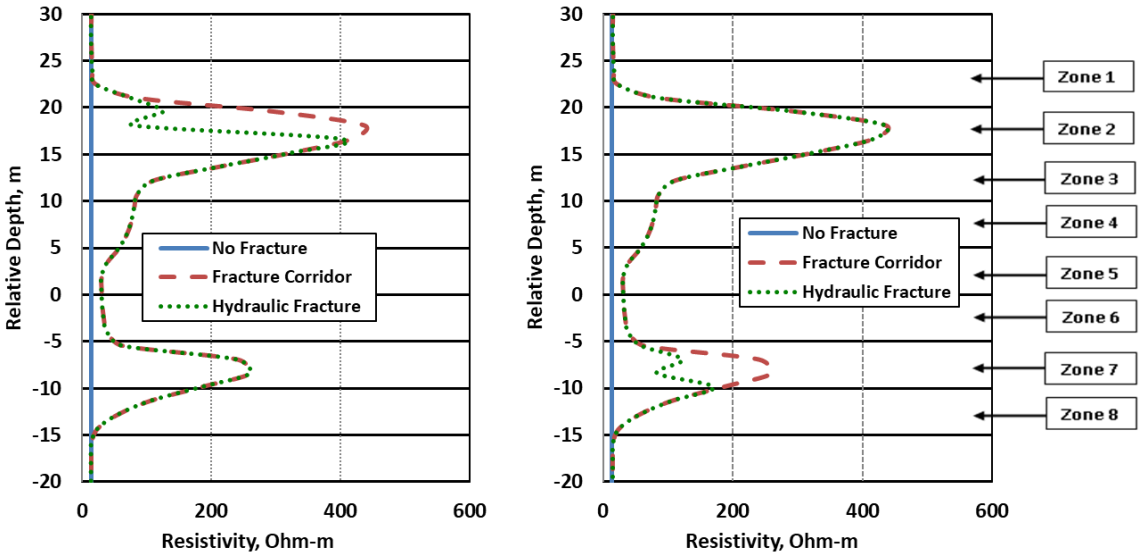

Figure 3.10 – Generated induction log for hydraulic and natural fracture interactions in organic shale formation case. Modified from Elliott et. al, 2014.

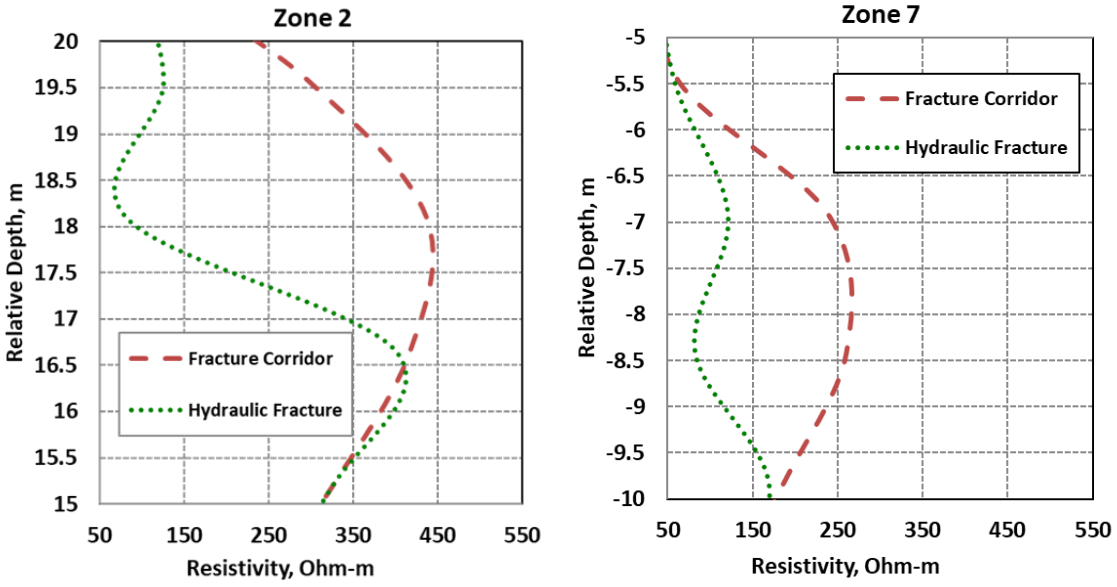

Figure 3.11 – Viable geologic targeting and corridor depletion zones for organic shale case. Modified from Elliott et. al, 2014.

3.4 Conclusions

We combined surface-gas readings and downhole measurements with EM induction log simulations to improve natural fracture corridor detection and characterization. Using these simulations, we described fractured zone degree of heterogeneity with a calculated anomalous diffusion coefficient, β. The β parameter are then used in simulating hydraulic and natural fracturing interactions for three cases: a sandstone formation, a carbonate formation, and an organic shale formation. Conclusions for this chapter are listed below.

1. Combining β values with resistivity measurements to describe fracture roughness normalizes unfractured reservoir conductivity
2. Generating induction logs with β parameters helps differentiate between high and low fracture concentrations
3. The best corridor depletion stimulation zones are carbonate or organic shale formations with β values greater than 0.3
4. Simulating EM measurements with anomalous diffusion improves high-grading of natural fracture corridors and better optimizes hydraulic fracture placement in fractured zones
5. Including anomalous diffusion in EM simulations improves geologic targeting which increases field production through natural fracture corridor depletion

CHAPTER IV

INTEGRAL EQUATION BASED WELLBORE PRECONDITIONER FOR 3-D ELECTROMAGNETIC RESPONSE MODELING

Surface-based controlled-source electromagnetic (CSEM) methods can aid in subsurface characterization and fluid monitoring in the far-field. However, to achieve accurate simulation results, we must first account for the electromagnetic (EM) response of the conductive wellbore casing. Modeling subsurface controlled-source electromagnetic (CSEM) responses using the finite-element (FE) method is challenging in the presence of highly conductive wellbore casing. The very large conductivity contrast between the casing and the host formation leads to increased computation time and potentially unstable solutions. We address this difficulty by preconditioning a FE solver with an integral equation (IE) primary solution that captures the CSEM response of a realistic-sized steel wellbore casing. Our hybrid IE-FE approach solves the primary field solution using 2-D integral-equation forward modeling and then interpolates the IE-computed solution onto the nodes of a FE mesh. Then using an existing FE simulator we solve for secondary electric and magnetic field solutions. This approach removes the need for an ultra-fine FE mesh around the wellbore, thereby improving FE solution stability while greatly reducing FE computation time. Our method is illustrated by modeling the CSEM responses of idealized fluid-bearing zones.

4.1 Introduction

Electromagnetic response modeling techniques have been established for a wide range of industry applications including CO_2 storage and geothermal exploration (Castillo-Reyes et. al., 2022), marine and terrestrial hydrocarbon exploration (Chave et. al. 2017 and Streich 2016), buried pipeline integrity (Couchman and Everett, 2022), energy harvesting (Beskardes et. al. 2019), induction logging (Everett et al., 2001), and hydraulic fracturing fluid flowback (Jones et. al. 2019). A challenging aspect of these applications involves handling the high electrical conductivity between a steel-cased wellbore and the surrounding host formation. Conductivity contrasts can range to 19 orders of magnitude (~10^6 S/m for steel casing to ~10^{-13} for organic-rich shale). Modeling these high contrasts typically requires time-consuming specialized techniques such as ultra-fine meshing around the casing region so there is plenty of room for new and efficient computational algorithms. Some commonly used approaches are described in the following paragraphs.

Patzer et al. (2017) use a 3-D finite-difference (FD) approach wherein the steel casing is included in the primary field as a series of dipoles whose moments are calculated from the primary transmitted field. This approach offers a computational speed improvement but is limited to vertical wellbores in a homogeneous half-space. Additionally, the method requires a structured mesh that does not allow for local refinement around the wellbore. Puzyrev et al. (2017) employ a 3-D FD code based on the curl-curl electric field formulation using parallel direct solvers with automatic grid

refinement. The method provides fast computation times but does require parallelization architecture so that it is not readily accessible to most engineers and geoscientists.

Heagy et al. (2019) used the finite volume (FV) approach to solve Maxwell's equation for cylindrically symmetric 2-D and 3-D geometries. They assign a high conductivity to the annular casing region and employ an ultra-fine mesh. The use of a cylindrical mesh leads to difficulties in accommodating deviated, horizontal, or multi-well casing scenarios. Hu et al. (2022) include steel casing without mesh refinement by using an edge-conductivity technique wherein the electric field is specified on mesh edges, the magnetic flux on mesh faces, and the steel casing is specified by using special mesh elements.

Weiss (2017) developed a hierarchical finite-element method (Hi-FEM) using unstructured tetrahedral meshing. He modified the governing Poisson's equation to include element-stiffness matrices for 2-D facets and 1-D edges. This technique has been proposed for applications such as energy harvesting for charging subsurface micro-sensors (Beskardes et. al. 2019), and casing integrity mapping (Wilt et. al. 2020). Cuevas and Pezzoli (2018) developed a 2-D cylindrical FE solution wherein the conductive casing is approximated by an array of dipole sources. The vertical steel casing is excited by a vertical electric field antenna located in the borehole. Castillo-Reyes et al. (2022) developed a joint 2-D magnetotelluric (MT) 3-D CSEM inverse model using a parallel and high-order vector finite-element algorithm for CO_2 storage and geothermal exploration applications. Couchman and Everett (2022) demonstrate a 3-D FE method

for detection of corrosion effects in near-surface buried pipelines. However, the method requires expensive ultra-fine meshing to be applied to oilfield casing scenarios.

Kohnke et al. (2018) developed a method-of-moments (Harrington, 1968) integral-equation (IE) technique by replacing the casing with small current dipoles. The method is computationally and memory efficient, but there are limitations on the permissible casing geometry. Orujov et al. (2020) describe a similar approach using wedge elements, the latter being used to represent bent sections of a horizontal pipe.

Um et. al. (2020) developed a hybrid FE-FD inversion algorithm that uses an unstructured tetrahedral FE mesh in the simulation domain and a course-structured rectangular FD mesh in the imaging domain. The hollow steel-cased well is modeled as a solid prism of equivalent conductance. Tang et. al. (2015) developed a hybrid IE-FE algorithm. The method of moments is used to calculate the primary field in a uniform half-space that includes an energized steel wellbore casing. The secondary field is then calculated by substituting the primary field, as a source term, into the FE formulation. Yu et. al. (2022) developed a FE method that discretizes the steel casing with triangular prism elements, its surroundings with pyramid elements, and the remaining host formation tetrahedral elements. Lui et. al. (2018) developed a hybrid IE-FE method wherein the FE portion solves the Maxwell equations in the interior domain while electric fields on the boundary are computed by the IE method.

Our method is a hybrid IE-FE algorithm that preconditions a FE simulator with a pre-computed IE primary solution for an infinite grounded wire source energizing a horizontal wellbore casing located in a uniform half-space. The IE solution is adapted

from Hohman (1971) by converting the large uniform rectilinear inhomogeneity he considered to one with a much smaller cross-section that is placed directly below and in alignment with the infinite-wire source. This approach significantly reduces FE computation time by removing the need for ultra-fine mesh around the casing and is fundamentally different from previous hybrid methods. We perform the IE calculations outside of the 3-D forward modeling, and hence do not need to include the casing in the FE formulation. Moreover, the method works with any FE formulation.

The remainder of this chapter is organized as follows. First, we discuss the IE forward modeling code, including benchmarking and validation exercises to test the IE code and solver stability. Then we apply the IE code to a simple oil-field scenario, using it to precondition an FE simulator. We illustrate the hybrid IE-FE method by investigating the EM response of a conductive subsurface fluid zone.

4.2 Methods

The terrestrial controlled-source electromagnetic (CSEM) geophysical method can be applied to critical tasks such as inspection of subsurface infrastructure or monitoring of enhanced geothermal or hydraulic fracturing operations. Terrestrial CSEM surveys typically operate with a grounded dipole transmitter and an array of surface and/or subsurface receivers. The transmitter generates an electromagnetic field that penetrates the underlying geological formation. A secondary magnetic field is produced by the induced eddy currents that are mediated by the migration of mobile charge carriers in the subsurface. Secondary electric and magnetic field CSEM measurements

are diagnostic of spatial variations in formation electrical conductivity caused by geological heterogeneity or the presence of fluids. For a given transmitter operating frequency $\omega = 2\pi f$, the signal amplitude and phase at the receiver are analyzed. We investigate herein a 2.5-D CSEM problem representative of an idealized oilfield scenario (for one embodiment of a terrestrial CSEM survey, see Figure 4.1).

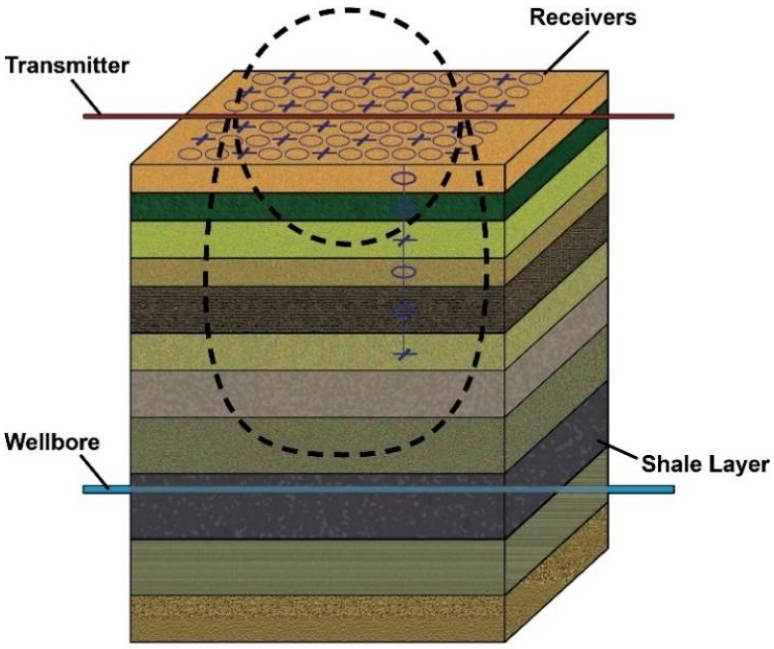

Figure 4.1 – An embodiment of a terrestrial controlled-source electromagnetic (CSEM) survey.

The conversion efficiency of the transmitted electromagnetic energy to kinetic energy for subsurface mobilized charge carriers determines the CSEM investigation depth. Electrical conductivity σ is determined by the product of the number density and mobility of the charge carriers (Everett and Chave 2019). Moreover, a normally incident

plane-wave signal loses $1/e \sim 0.3679$ of its incident amplitude after penetrating one skin depth δ into a uniformly conducting medium. Thus, higher electrical conductivity leads to greater energy conversion and consequently a smaller depth of penetration. The formula for skin depth (e.g. Moran and Kunz 1962) is

$$\delta = \sqrt{\frac{2}{\mu\sigma\omega}} \tag{4.1}$$

where $\mu = 4\pi$ x $10 - 7$ H/m denotes the magnetic permeability of free space. Reducing the transmitter operating frequency increases the depth of investigation at the cost of reducing spatial resolution. For the modeling in this chapter, we select combinations of operating frequency and formation conductivity corresponding to a depth of investigation $d \sim 1.5\delta - 2.0\delta$ to maintain good signal to noise ratio (e.g. Grant and West 1965).

We developed a 2-D integral-equation (IE) forward modeling code (hereinafter termed "simulator") based on the algorithm of Hohmann (1971), see Appendix C. The problem considered is that of an infinite-line source lying on the Earth's surface and aligned with the strike of a 2-D subsurface heterogeneity. The general matrix equation for the scattered electric field E_y inside the body is:

$$[\mathrm{K}] \cdot E_y = -E_y^i \tag{4.2}$$

where [K] represents a complex dense matrix, and E_y^i is the incident (primary) electric field of the line source lying on a uniform half-space. The IE approach requires discretization and calculation of the scattered field only within the inhomogeneous region. Green's functions for a conductive half-space are then used to propagate the effects of the scattered field onto the entire domain. The kernel of the Green's functions for the integral equation was rewritten as a sum of nonsingular and singular terms. The singular term was obtained using an analytical expression with modified Bessel functions. We extracted the modified Bessel function values using a MatLAB code containing 1331201 interpolation points and stored them within a table for the main program. The nonsingular Green's function was calculated numerically using Cosine integration with 2304 integration points. The large number of Bessel function interpolation values and Cosine integration points were required to maintain accuracy when working with high conductivity contrasts at oil-field scenario depths.

We modified Hohmann's (1971; his Figure 4) principal test case by converting the large uniform rectilinear inhomogeneity to one with a much smaller, square cross-section that is placed directly below and in alignment with the infinite-wire source. The converted heterogeneity, endowed with sufficiently high electrical conductivity, is supposed to be representative of a steel wellbore casing. The strong inductive coupling between the infinite-line source and the infinite wellbore casing generates a "casing-as-a-secondary-antenna" effect. The primary current from the wire and the current induced in the casing are nearly equal in magnitude and oppositely directed. Thus, the electromagnetic field

generated by the casing nearly cancels out the current generated by the infinite wire source. This is elaborated further below.

The modifications to the Hohmann test case are shown in Figure 4.2. There is a large uniform rectilinear inhomogeneity set at a distance $X = X_a$ (all distances are measured in skin depths) from the infinite-line source of strength I. The inhomogeneity has height H, width T, burial depth D and it is infinitely extended in the strike direction Y. The electrical conductivity of the conductive inhomogeneity is σ_2, while that of the resistive host formation is $\sigma_1 < \sigma_2$.

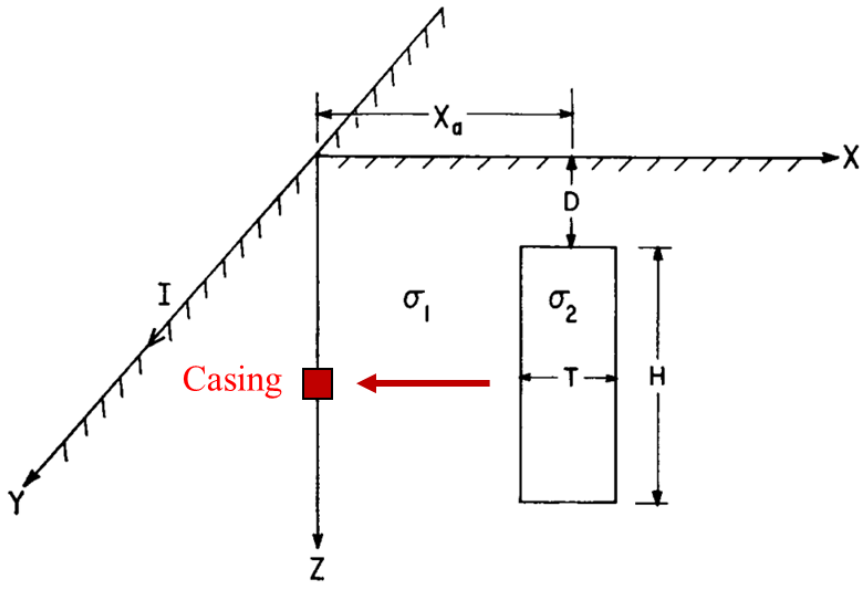

Figure 4.2 - Section view of the original Hohmann two-dimensional conductive inhomogeneity buried in the earth, and its modification to a wellbore casing scenario, shown in red.

4.3 Results

4.3.1 Benchmarking

We validated the IE simulator by comparing its output to that of the Hohmann 1971 test case. The latter consists of a uniform rectilinear inhomogeneity of width $T = 0.03\delta$ and vertical extent $H = 0.3\delta$. The inhomogeneity is set at burial depth $D = 0.05\delta$ and is located at distance $X_a = 0.5\delta$ from the infinite-line source. The line source current is of unit strength $I = 1\ A$. Additionally, there is an electrical conductivity ratio of $\sigma_2/\sigma_1 = 10^3$ between the inhomogeneity and the host formation.

The body of the inhomogeneity is divided into $M \times N$ square cells. The discretizations examined by Hohmann (1971) in his Figure 4 are very modest by today's standard: (*i*) $1 \times 10, \Delta = 0.9\delta_2$; (*ii*) $2 \times 20, \Delta = 0.6\delta_2$ and; (*iii*) $3 \times 30, \Delta = 0.3\delta_2$ where Δ is the individual cell size and δ_2 is the skin depth in the body. The results shown in Figure 3 (left) are presented in terms of the total vertical magnetic field response normalized by the primary portion of the vertical magnetic field (H_z/H_z^{P}) along a skin-depth-normalized surface profile. We find excellent agreement for both the amplitude and phase for the case $\Delta = 0.6\delta_2$ on our finer 10×100 discretization. Note that we adjusted the frequency upward to achieve the much higher mesh resolution permitted by today's computational resources.

Next, we evaluated the effect on the solution by varying the discretization of the mesh from 8×80 to 13×130 cells, with the results shown in Figure 4.3 (right). The figure confirms the stability and convergence of the solution on different mesh sizes.

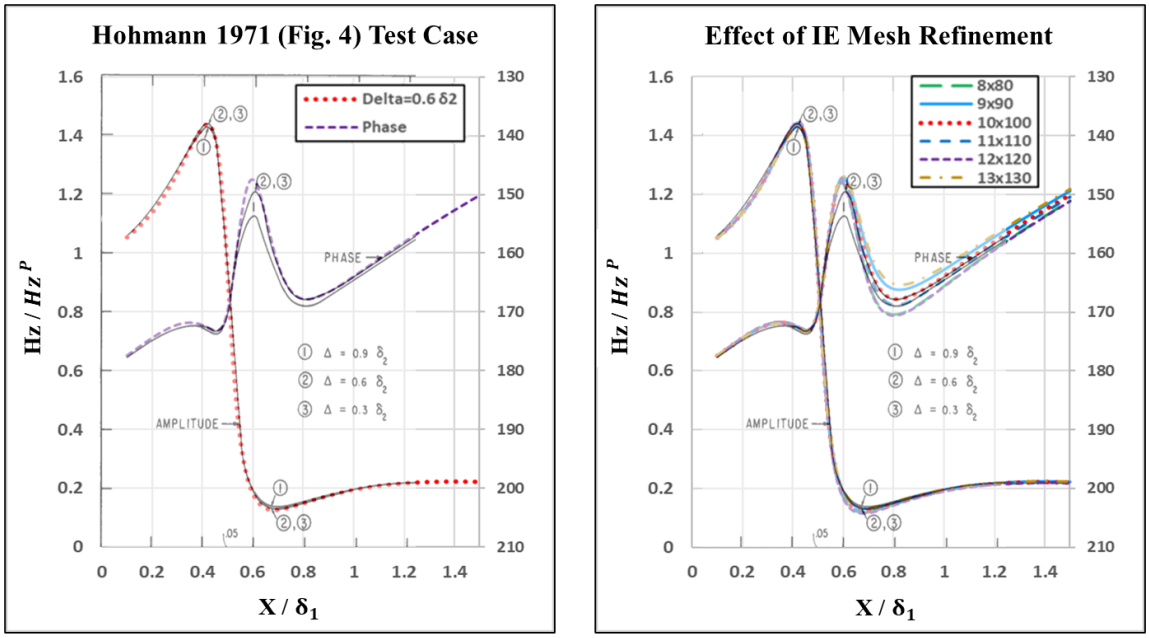

Figure 4.3 – left: comparison of the IE simulator on the Hohmann test case; right: effect of mesh discretization size on IE simulator results.

To further benchmark the IE simulator, we halved the electrical conductivity contrast for comparisons against Figures 5 and 6 of Hohmann (1971), which in turn was previously compared to an equivalent finite-element solution of Coggon (1971). The H_z/H_z^{P} profile is shown in Figure 4.4 (left) whereas the horizontal magnetic field profile H_x/H_z^{P} is shown in Figure 4.4 (right). We selected three mesh discretization sizes $9 \times 90, 10 \times 100$ and 11×110 for the comparisons, each of which exhibit a good match in both phase and amplitude.

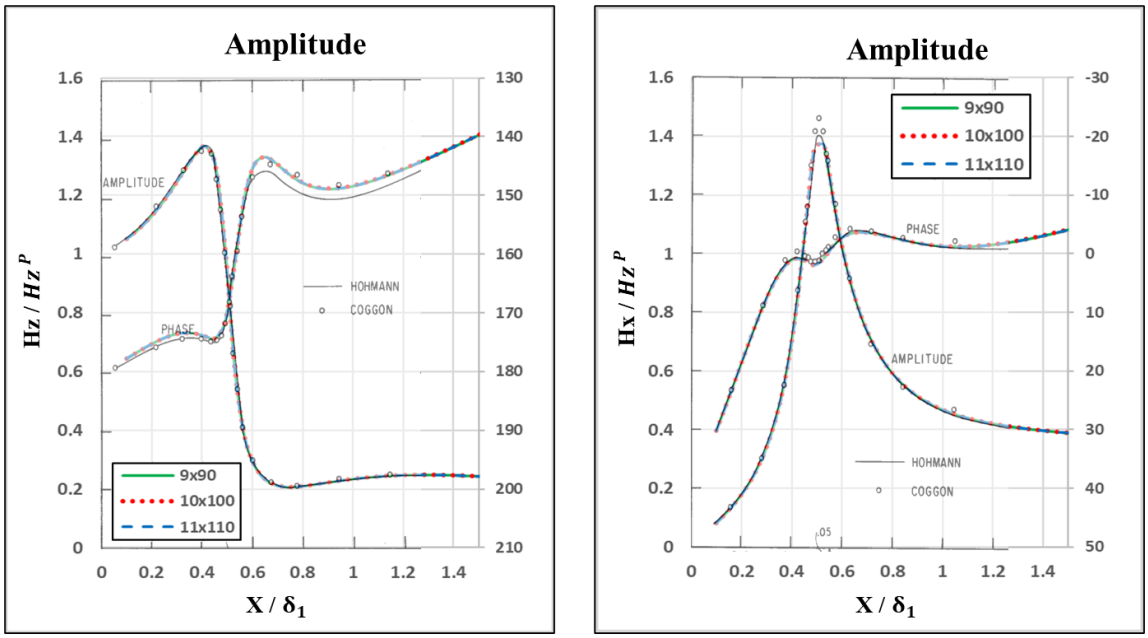

Figure 4.4 – IE simulator benchmarking against Hohmann (1971) and Coggon (1971), left: H_z/H_z^P profile; right: H_x/H_z^P profile.

The final IE-simulator benchmarking case investigated the stability of the solution under varying inhomogeneity burial depth. We simulated H_x/H_z^P profiles for burial depths $D = 0.05\delta, 0.1\delta, 0.2\delta$ and 0.3δ, while the other model parameters were kept the same as the Hohmann Figure-4 test case. Additionally, we included the response of the host formation without the conductive inhomogeneity. It is evident that the IE-simulator results shown in Figure 4.5 compare favorably to Figures 15 and 18 in Hohmann (1971).

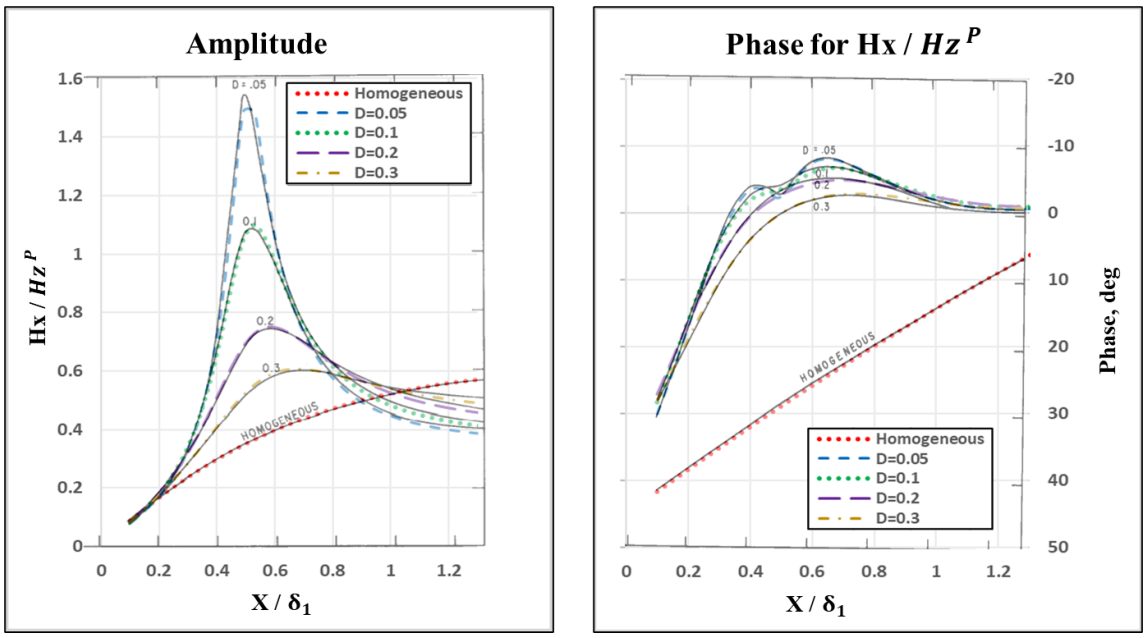

Figure 4.5 – IE simulator benchmarking for variable inhomogeneity burial depth D: left, H_x/H_z^P amplitude; right, H_x/H_z^P phase.

4.3.2 Matrix Solvers

We solved the IE complex dense matrix system (equation 2) using the QR decomposition subroutine `qrdcmp` from Numerical Recipes in Fortran (Press et al. 1992). To validate the QR solver accuracy and efficiency, we compared its performance to an array of different custom and pre-built solvers. Our custom matrix solvers included singular value decomposition (SVD) and conjugate gradient (CG) routines, both written in Python. The pre-built solvers included SciPy Python LU and QR decomposition routines, in addition to MATLAB gaussian elimination, conjugate gradients squared (CGS), bi-conjugate gradient (Bi-CG), stabilized bi-conjugate gradient (BICSTAB), quasi-minimal residual (QMR), and generalized minimal residual (GMRES) routines.

We used each of these solvers in the IE simulator and compared the resulting H_z/H_z^{P} responses to the Hohmann (1971) Figure-4 test case (Figure 4.6). Each solver generates the same solution to within 1 part in 10^{10} or less, with minimal difference in computation time, indicating that [K] is a stable well-conditioned matrix.

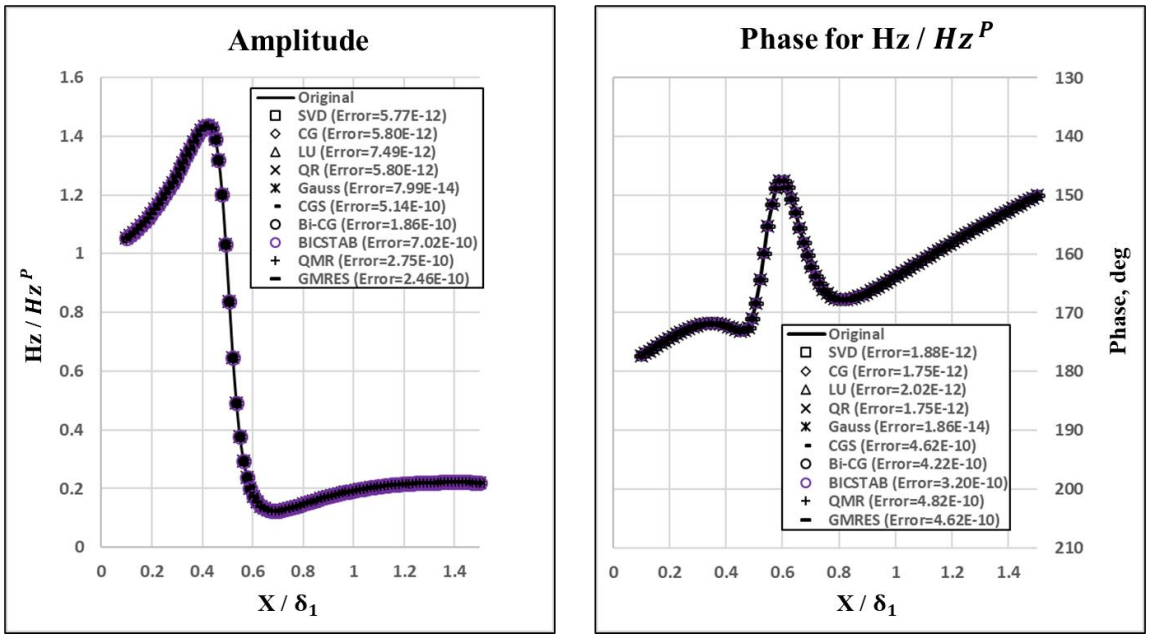

Figure 4.6 – Matrix solver comparison for IE simulator: left, amplitude; right, phase of $\mathbf{H_z/H_z^P}$ response.

4.3.3 Wellbore Modeling

Preparatory to steel-wellbore modeling, we simulated the H_x/H_z^{P} response of the Hohmann Figure-4 test case for a wide range of electrical conductivity contrasts σ_2/σ_1 between the inhomogeneity and the host formation. Contrasts were selected to be higher and lower than Hohmann's test case, which used $\sigma_2/\sigma_1 = 10^3$. As the contrast increases,

the IE solution remains stable and converges uniformly as $\sigma_2/\sigma_1 \rightarrow 10^9$ (Figure 4.7, left). This result suggests that the IE simulator can comfortably handle large electrical conductivity contrasts.

We then converted the Hohmann (1971) rectilinear inhomogeneity to one that is much smaller and of square cross-section. The so-called "pipe" has dimensions $T = H = 0.095\delta$ and is discretized into 40×40 cells. The IE-simulator-calculated H_z/H_z^{P} response is shown at Figure 4.7, right wherein it is noted that a stable, convergent solution has been found, even at very high contrasts.

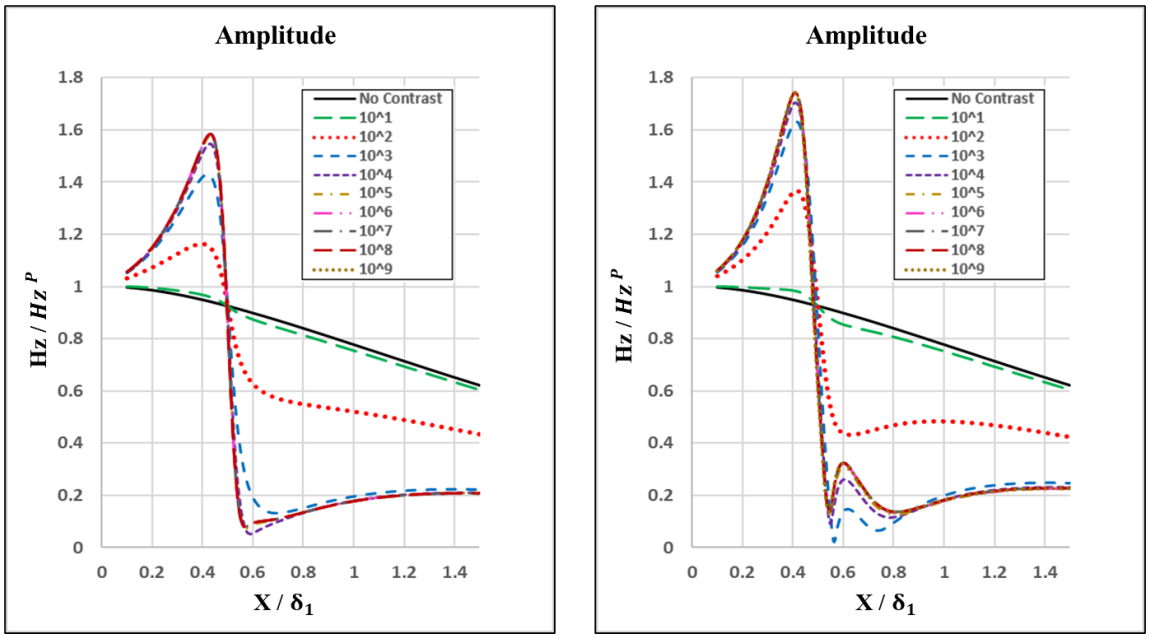

Figure 4.7 – IE simulator results for variable conductivity contrast: left, the Hohmann 1971 test case; right, the smaller square inhomogeneity.

We next use the IE simulator to determine the secondary response H_z^S for various highly conductive "pipe" inhomogenities (40×40 cells) set in a uniform host with conductivity similar to that of organic-rich shale, $\sigma_1 = 0.001$ S/m. The pipe dimension ranged from realistically-sized 5.5 in. (0.14 m) to unrealistically large 40 ft. (12.2 m). The pipe's horizontal location is lowered to 5000 ft. (1524 m) below and in alignment with the infinite-line source, while a 300 Hz operating frequency is used. The results are shown in Figure 4.8**,** left. The principle of equivalent conductance, in the 2-D case considered here, allows that targets of the same conductance (product of electrical conductivity and cross-sectional area) should generate the same response bar a constant scale factor. Accordingly, we scaled the computed H_z^S responses by a consistent scale factor of steel thickness normalized by pipe dimension to obtain equivalent solutions (Figure 4.8, right) down to the 5.5 in.-sized wellbore. Additional, results for the horizontal scattered magnetic field H_x^S amplitude response is shown in Figure 4.9. The scattered magnetic field phase response shows all scaled pipe diameters are in-phase (Figure 4.10). The fact that the IE-simulator obeys the principle of equivalence provides confidence that the simulator can be used to model the 2-D response of a realistic-sized steel wellbore.

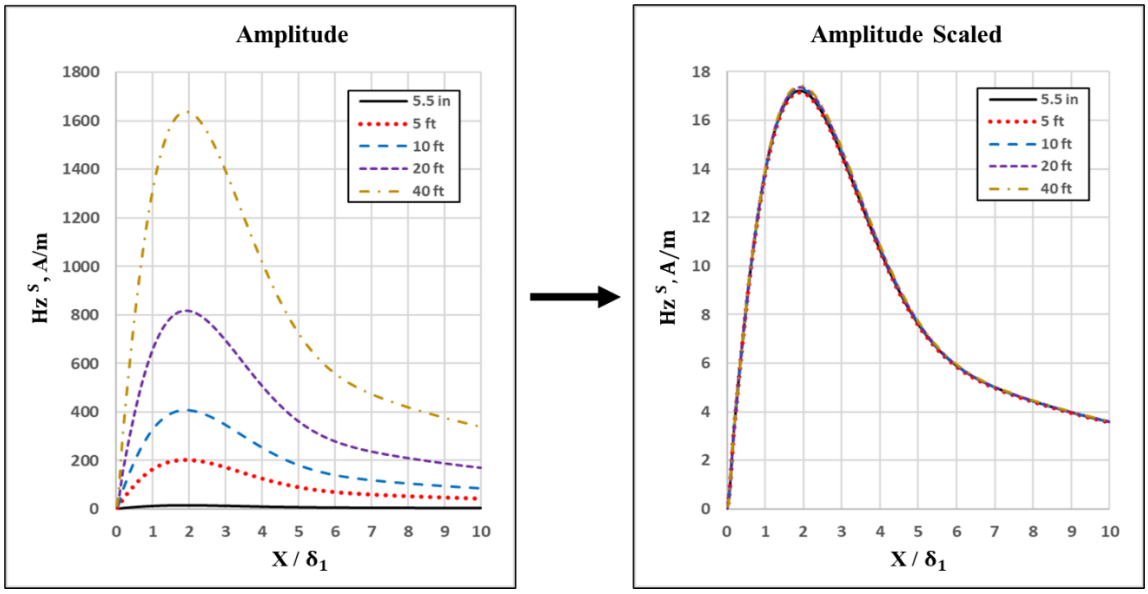

Figure 4.8 –left: IE-simulator scattered vertical magnetic field amplitude responses for varied pipe dimensions; right, scaled responses showing the equivalence of solutions that have the same pipe conductance.

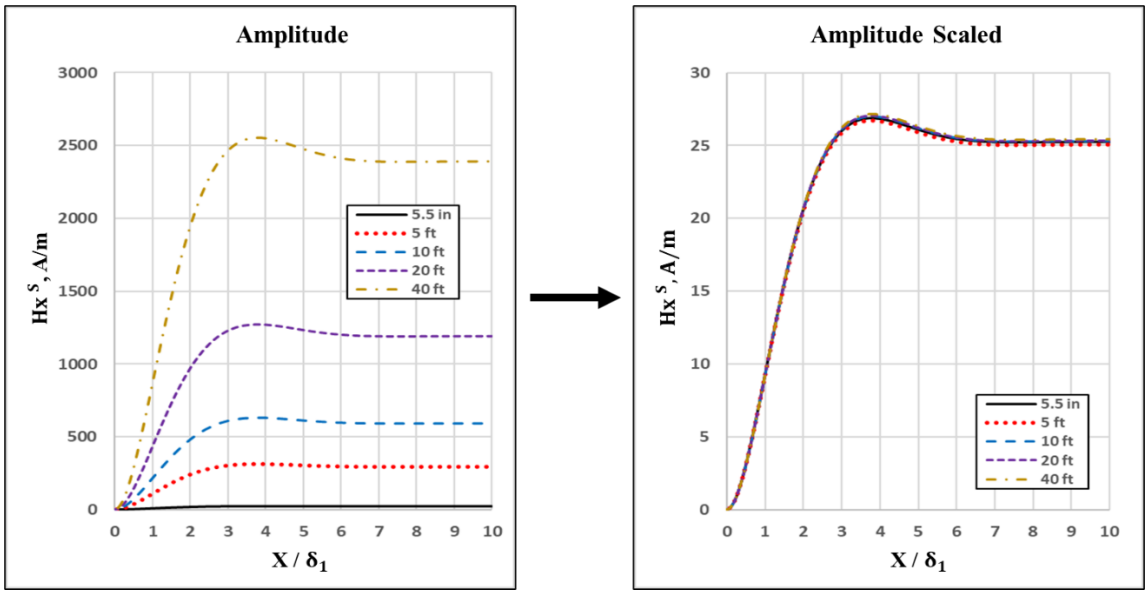

Figure 4.9 –left: IE-simulator scattered horizontal magnetic field amplitude responses for varied pipe dimensions; right, scaled responses showing the equivalence of solutions that have the same pipe conductance.

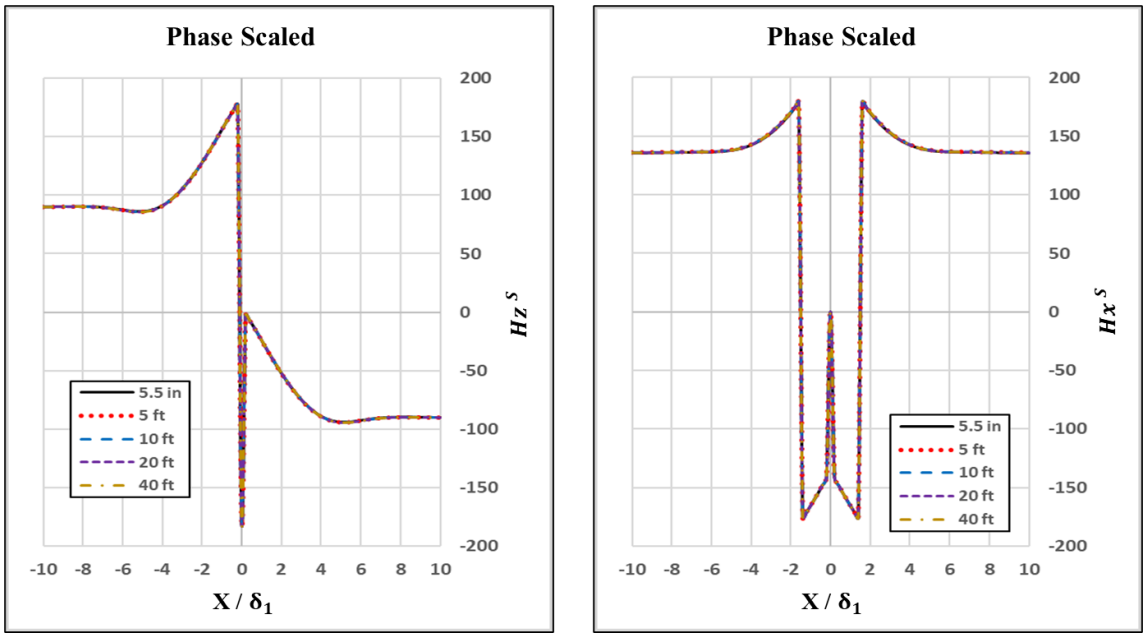

Figure 4.10 – IE-simulator scaled scattered magnetic field phase responses for varied pipe diameters.

We next simulated the H_x and H_z responses for a scenario in which the 5.5-in. steel casing is set in an organic-rich shale host and placed at $X_a = 0$, i.e. directly beneath the infinite wire source. The results, shown in Figure 4.11, indicate that the casing acts as a source of earth return current. The casing current flow is nearly the same strength and exactly opposite in direction to the transmitter current. The secondary electromagnetic response generated by the return current in the casing almost exactly cancels out the primary field at the surface. This is indicated by the near-vanishing of the total signal (black lines) in Figure 4.11. In the scenario under consideration, the host is a uniform half-space. However, if a geological heterogeneity were present, such as a

lithological variation or a subsurface fluid zone, then any appreciable total H_x and H_z response should be almost entirely attributed to that. This occurs since the line source/casing in the parallel alignment configuration generates virtually null response.

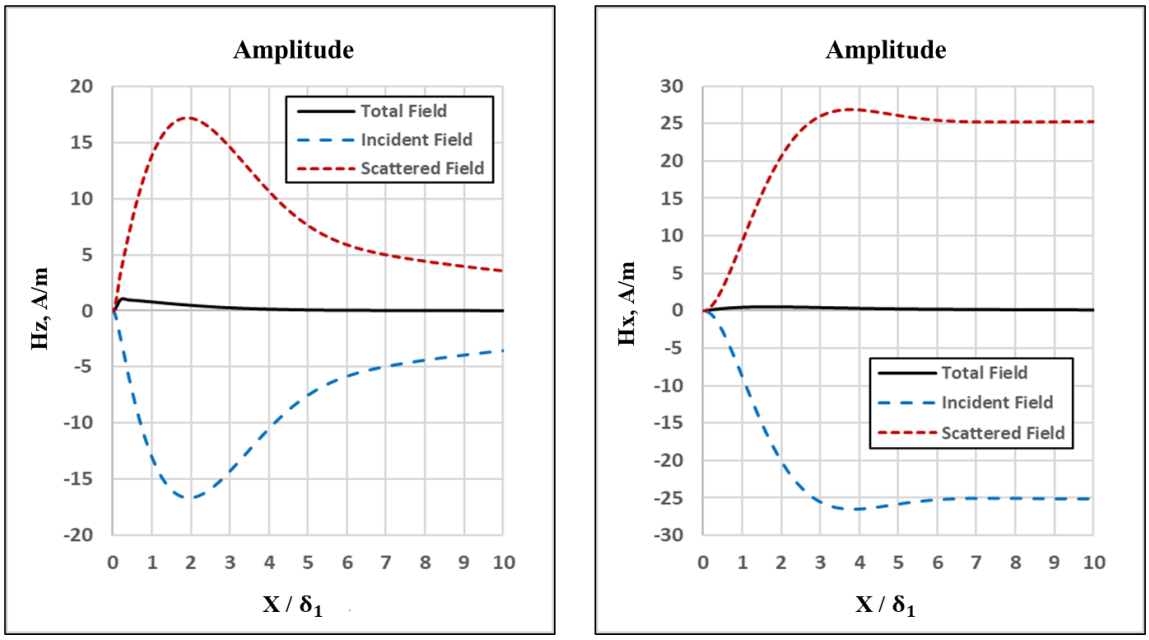

Figure 4.11 - Oilfield scenario surface CSEM response indicating the casing acts as a return current: left, H_z responses; right, H_x responses.

4.3.4 Preconditioning the Finite-Element Simulator

The E_y electric-field along-strike responses (primary and secondary) at the surface, and throughout the modeling domain, are determined within the IE simulator by propagating the scattered electric current outward from the inhomogeneity using the half-space Green's functions. The latter are given in the Hohmann (1971) paper. Note that, in the 2-D case considered herein, the other components of electric field, by

symmetry, are identically zero, $E_x = E_z = 0$. Contours of the primary (incident) and secondary electric field are shown in Figure 4.12, top panel, for the Hohmann Figure-4 test case and in Figure 4.12, bottom panel, for the 5.5-in. steel-casing scenario. The black crosshairs on the right-side plots indicate the position of infinite wire source whereas those on the left-side mark the center of the buried heterogeneity. The contour patterns indicate that the secondary electric field E_y^{S}, as expected, behaves in a similar fashion to the primary electric field E_y^{P}. This behavior occurs insofar as it appears to originate from a source of current, in these two cases the Hohmann Figure-4 heterogeneity (top right) and the buried steel casing (bottom right).

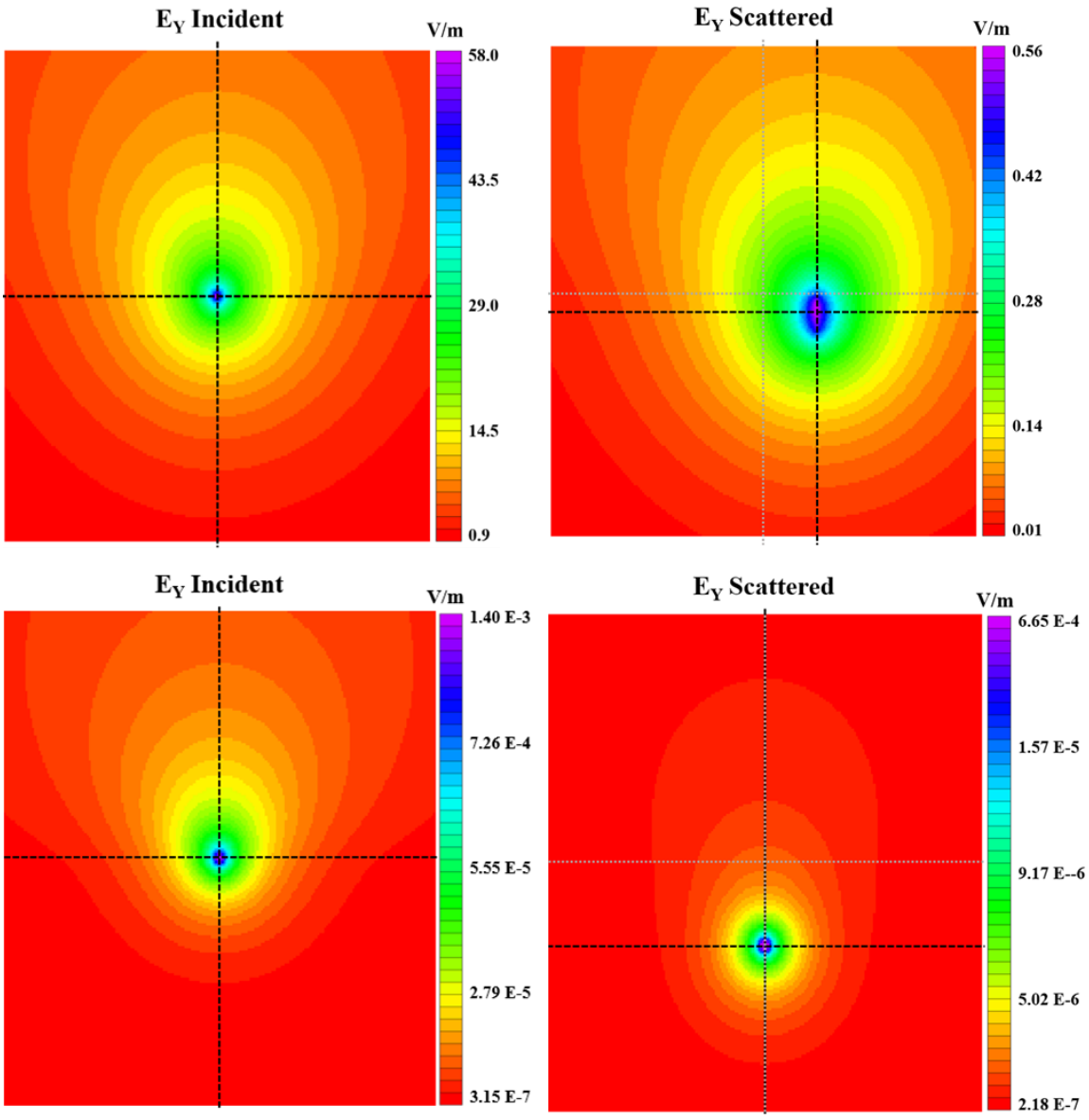

Figure 4.12 – Contours of incident E_y^i and scattered E_y^S electric field response for two models: top, Hohmann 1971 test case; bottom, 5.5-in steel casing.

We envision the IE simulator as an efficient means to generate a primary field that includes the effects of a realistically-sized, highly conductive steel wellbore. The primary field is intended for use in CSEM finite-element computations. Next, we

converted the IE-simulator response into a primary field for a finite-element simulation by interpolating the former onto the nodes of a FE mesh. The procedure is based on MLSI, moving-least squares interpolation (Tabbara et al. 1994), and the results are illustrated in Figure 4.13. Then, using an in-house FE simulator *seatem* (Badea et al. 2001), we computed solutions to subsurface models that include 3-D conductivity anomalies in the presence of a steel wellbore. This version of s*eatem* is a finite-element numerical simulator, containing a rectangular mesh, that solves the governing diffusive Maxwell equations formulated in terms of secondary Coulomb-gauged electromagnetic potentials. It uses the QMR algorithm to iteratively solve the FE linear system. The governing equations, recast in terms of secondary potentials to avoid a mathematical singularity at the transmitter location, are given as follows:

$$\nabla x \nabla x A_s - \nabla(\nabla \cdot A_s) - i\omega\mu_0\sigma(A_s + \nabla\Psi_s) = \mu_0\Delta\sigma\vec{E}_p \tag{4.3}$$

$$\nabla \cdot [i\omega\mu_0\sigma(A_s + \nabla\Psi_s)] = -\nabla \cdot \left(\mu_0\sigma\vec{E}_p\right) \tag{4.4}$$

$$\vec{E}_p = i\omega\left(A_p + \nabla\Psi_p\right) \tag{4.5}$$

where (A_s, Ψ_s) are the secondary potentials, (A_p, Ψ_p) are the primary potentials, and $\Delta\sigma \equiv \sigma - \sigma_0$ is the difference between the required electrical conductivity of the formation σ and the known background electrical conductivity σ_0. Additional details on the original mathematical development for *seatem* are described in Badea et al. 2001. An abbreviated version of the mathematical development for *seatem* is included in Appendix B.

The novel hybrid IE-FE approach described herein enables a preconditioning of the FE simulator with the primary response of the infinite-line source in the presence of the steel casing. The incorporation of such an IE-based primary solution removes the need for an ultra-fine FE mesh around the wellbore. Notice also that the modeling domain size spanned by the FE mesh is smaller than the domain on which the IE solution is computed. The reason for this difference in size is to avoid any edge effects when the IE solution is interpolated onto the FE mesh.

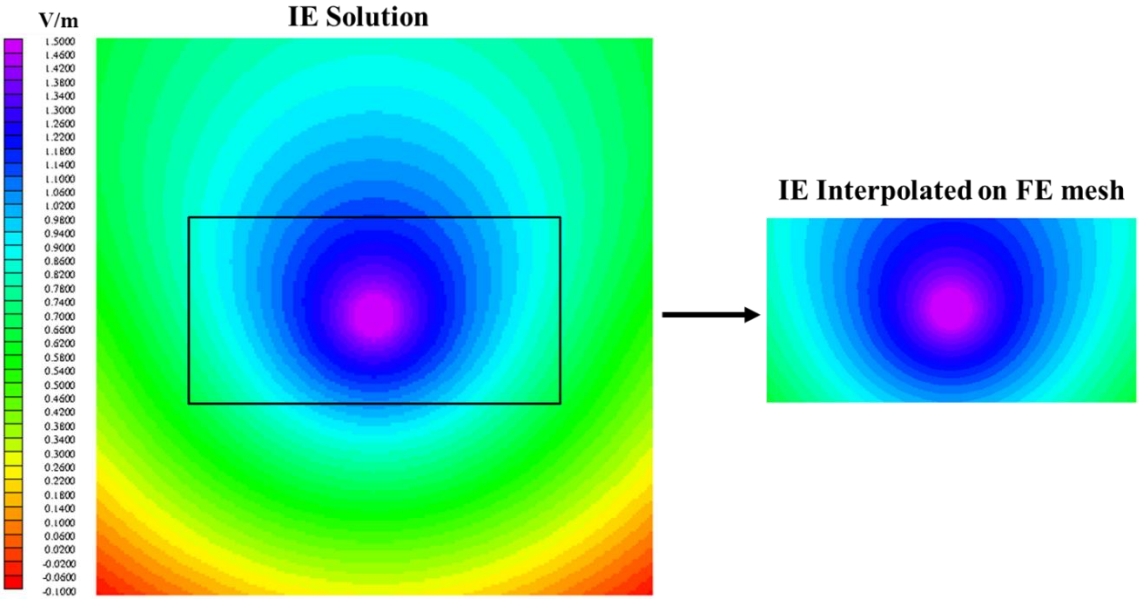

Figure 4.13 – Interpolation of IE-computed primary electric field E_y onto a finite-element mesh.

4.3.5 Finite-Element Modeling with the Integral Equation Preconditioner

We demonstrate our hybrid IE-FE approach by simulating 2.5-D CSEM responses for scenarios that involve a 5.5-inch steel casing set at 5000 ft. depth in an organic-rich shale. The parameters for this scenario match those of the previous 5.5-inch casing tests. For the FE demonstration using *seatem*, two symmetric 3-D conductive zones (left and right) are placed on either side of the wellbore; these zones could represent a fluid-rich zone or any other conductive heterogeneity, hereinafter for convenience they are referred to as "fluid zones". The electrical conductivity of the fluid zones is 0.01 S/m while that of the host formation is 0.001 S/m. Each fluid zone extends 2 km in the x-and z-directions, and 4 km in the y-direction. The latter is aligned with the common strike of the infinite-line source and casing. The problem is termed 2.5-D because a 2-D primary excitation is imposed on a 3-D structure.

We interpolated IE solutions onto the interior nodes of several FE meshes of size 41^3, 65^3, 81^3, 129^3, and 161^3 nodes. The IE-*seatem*-calculated H_z^S responses at the surface are shown in Figure 4.14. For the subsurface model containing both left and right fluid zones, there is a good convergence with increasing FE mesh size and, especially on the larger meshes, the appropriate symmetry is observed, i.e. a mirror reflection of the response about the $x = 0$ axis. Next, we calculated separate IE-*seatem* H_z^S responses on the 129^3 meshing for two models, one containing the left fluid zone only and one containing the right fluid zone only. The results are shown by the blue symbols in Figure 4.14. The responses show the expected left-right symmetry which is a confidence check

that the IE-*seatem* algorithm generates reliable results for asymmetric subsurface models.

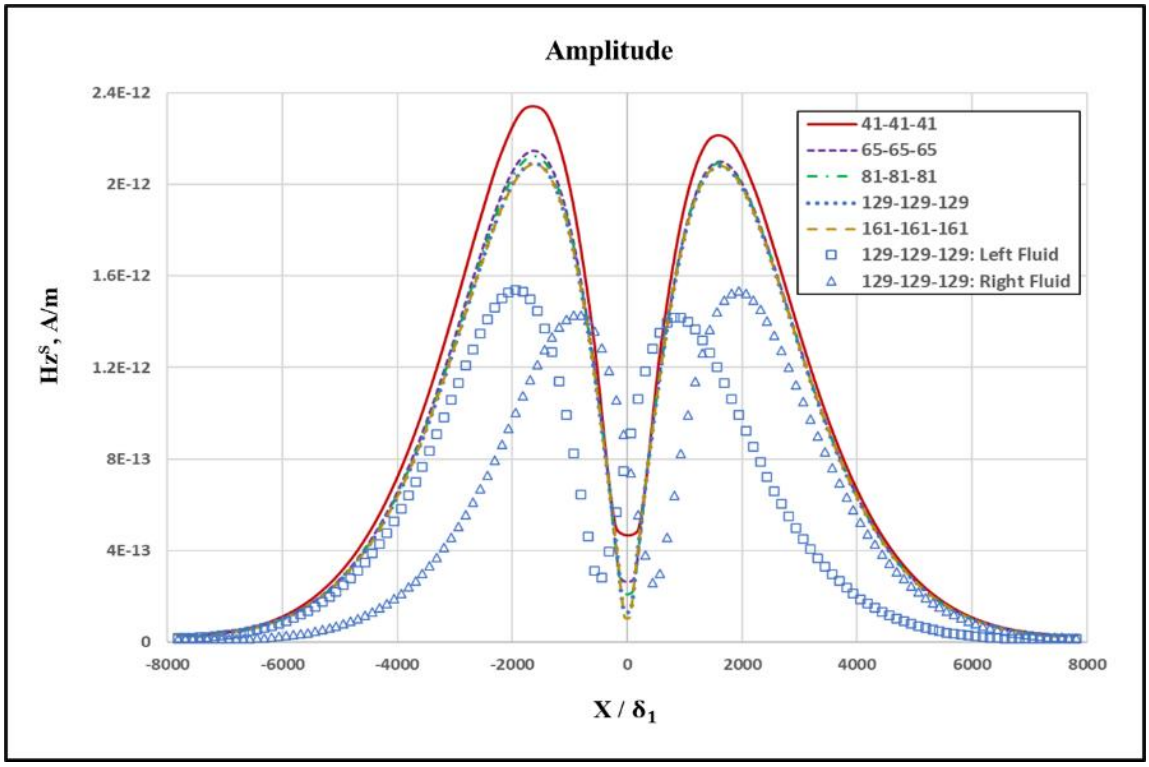

Figure 4.14 – IE-*seatem* responses for models containing left, right, and left+right fluid zones, the latter for different mesh discretizations.

Next, we investigated convergence rates for modeling scenarios including the 5.5-in. steel casing and the left+right conductive fluid zones. We ran the scenario on both the IE-*seatem* and the stand-alone *seatem* (i.e. without the IE preconditioning) codes, and compare the results for mesh sizes ranging from 41^3 to 161^3. All cases used the same QMR tolerance of 10^{-18}. Note that the *seatem*-stand-alone cases use an x-directed horizontal dipole transmitter without the 5.5-in. casing present. This difference

in the subsurface model and its excitation is immaterial since here we are interested only in examining the QMR convergence rate, as a function of mesh size, to determine whether it is affected by the IE preconditioning. Results for each mesh size with and without the IE preconditioning are shown in Figure 4.15. There are similar QMR convergence rates for the IE-*seatem* and the *seatem*-standalone runs, suggesting that IE preconditioning has little effect on the run-time of the FE linear system solver.

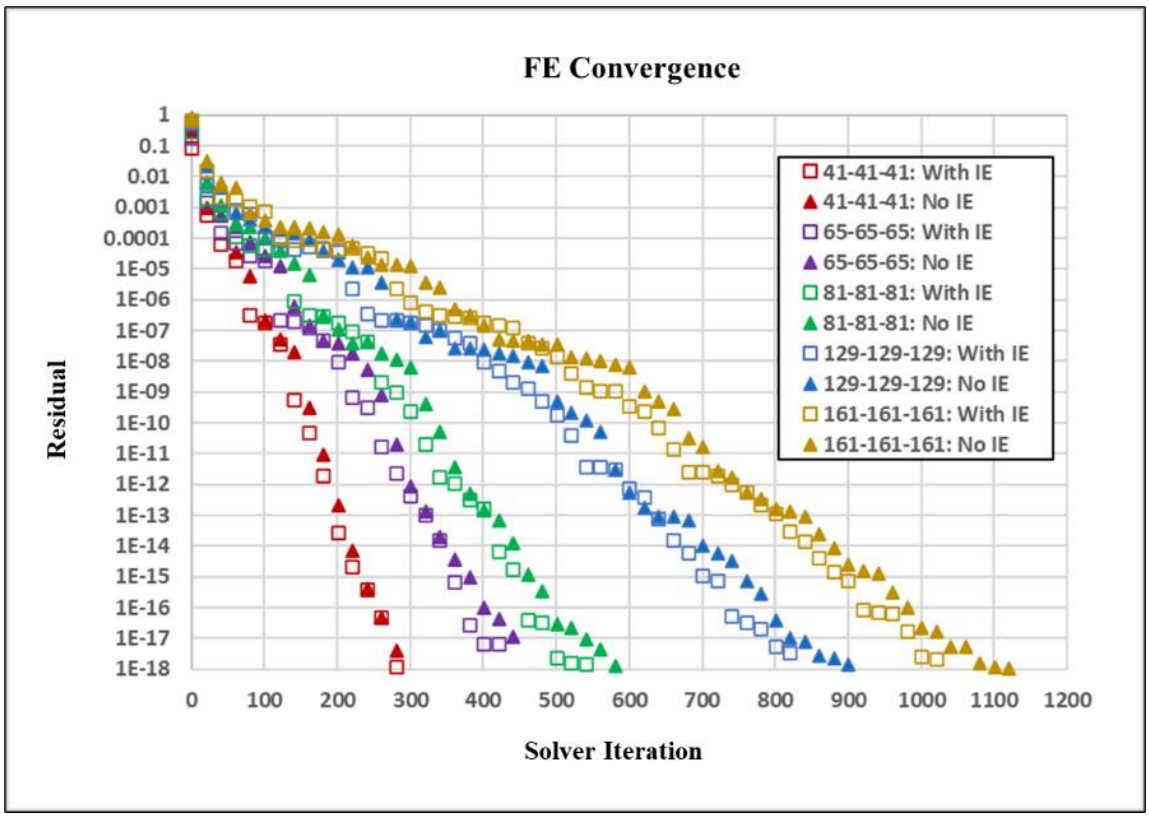

Figure 4.15 – FE convergence rates of IE-seatem and seatem-stand-alone responses with conductive fluid zones.

We compared the simulation times for the previous IE-*seatem* and the *seatem*-stand-alone modeling scenarios with the left+right conductive fluid zones. Recall that the 2.5-D IE-*seatem* code solved for an infinite-wire line source in the presence of the conductive casing whereas the fully 3-D *seatem*-stand-alone code solved for a horizontal electric dipole with no casing. The principal structural difference between the preconditioned and stand-alone codes is how the primary solution is constructed. It is either read in as a pre-computed IE solution or calculated explicitly using analytic equations. Hence, any difference in computational times can be attributed to the primary-solution specification. Table 1 lists the results for a comparison of the two codes. We observed an 85-91% reduction in computation time by implementing the IE preconditioner. Clearly, the largest use of the computer time by the *seatem*-stand-alone code is calculation of the primary field by analytic equations. Moreover, the *seatem*-stand-alone modeling did not include the steel casing in this comparison. Including the casing, with the ultra-fine mesh refinement it entails, would have greatly increased the *seatem*-stand-alone run-time, whereas the casing was already included in the IE-*seatem* modeling.

Table 4.1 – Computation time comparison with and without IE preconditioning.

FE Mesh	Nodes	FE Computation Time		
		With IE, min	No IE, min	% Reduction
41-41-41	68921	3	21	85.71
65-65-65	274625	9	100	91.00
81-81-81	531441	20	190	89.47
129-129-129	2146689	124	867	85.70
161-161-161	4173281	259	1734	85.06

4.4 Discussion

We have developed an IE-based wellbore preconditioner that reduces the computation time of FE-based 3-D CSEM responses by removing the need for an ultra-fine mesh around the wellbore casing. The IE simulator was validated against Hohmann (1971) and Coggon (1971). The first benchmarking scenario (Figure 4.3) found good agreement with Hohmann for vertical magnetic field amplitude and phase responses. We varied the mesh discretization and confirmed that changes in mesh size have negligible impact on the computed response. A second validation scenario (Figure 4.4) also matched well with Hohmann and Coggon for variable electrical conductivity contrast and mesh size. A final benchmarking scenario (Figure 4.5) found good agreement with Hohmann for variable inhomogeneity burial depth.

We used QR decomposition to solve the complex dense matrix in the IE equation. The solver produced essentially identical results as 4 Python and 6 MATLAB algorithms (Figure 4.6). Relative errors ranged from 10^{-10} to 10^{-14} with minimal

differences in computation time. The lack of dependence of the solution on the solver indicates that the matrix is well-conditioned.

Our IE simulator is capable of handling high electrical conductivity contrasts between a very small casing and the surrounding host formation (Figure 4.7). We observed convergence for contrasts to 10^9. Therefore, the IE could calculate all the contrast cases. We simulated vertical and horizontal magnetic field responses for various steel casing diameters (Figure 4.8, Figure 4.9). The principle of similarity permitted scaling the response by the casing size and conductivity to obtain equivalent solutions. This allows for precomputing a single primary field solution for use as a preconditioner to FE computations for different choices of casing size and conductivity. We then simulated the vertical and horizontal magnetic field responses for a scenario representing a 5.5-inch steel casing set in a resistive half-space. The casing behaves as an earth return current (Figure 4.10), i.e. an image source carrying a current nearly equal and opposite to the transmitter current. The field of the return current almost exactly cancels out the primary field at the surface, in which case a subsurface heterogeneity response would be the main contribution measured by receivers.

We developed a novel approach to modeling steel casing in 3-D CSEM simulations by preconditioning a FE method with an IE-computed primary solution. Incident and scattered electric field solutions were shown for both the Hohmann test case and a scenario involving a realistic 5.5-in. oilfield casing (Figure 4.11). The IE method requires discretizing only the domain of the heterogeneity, with the homogeneous area surrounding the casing modeled by half-space Green function propagators. We inserted

the IE-equation response into the FE simulator by interpolating the computed response onto the interior nodes of a FE mesh (Figure 4.12). A version of our FE simulator *seatem* was used to compute the solutions to 3-D subsurface models in the presence of conductive inhomogeneities. However, any secondary-field FE simulator can be used to accomplish this task, the use of *seatem* is not necessary.

We applied our hybrid IE-FE approach to simulate the magnetic and electric field responses for a scenario involving a 5.5-in wellbore casing surrounded by two symmetric conductive fluid zones. We observed the appropriate symmetry in the response of the two fluid zones and found convergence of the magnetic field amplitude with increasing FE mesh discretization (Figure 4.13). Next, we compared the convergence rates for a range of FE mesh sizes with and without the IE preconditioner (Figure 4.14). Convergence rates were similar for both methods, indicating that the IE-preconditioning does not degrade the FE matrix conditioning. FE simulation times with and without the IE preconditioner were then compared (Table 4.1). We observed 85-91% reduction in FE computation time with IE preconditioning. The IE-FE hybrid implementation described herein uses an infinite-wire line source while the FE method alone is based on finite electric dipole excitation. A fully 3-D IE code is required to model the steel casing response due to finite dipole excitation.

4.5 Conclusions

We present a novel method for handling the high electrical conductivity contrast between a slender steel wellbore casing and the enclosing host geological formation. By

preconditioning an FE solver with an IE-computed primary solution, we remove the need for ultra-fine FE meshing of the wellbore and its immediate surroundings. The IE preconditioner provides a stable primary field source solution to the FE solver, improving solution stability while reducing computation time by 85-91%. Our IE-FE hybrid approach is based on an infinite-wire line source while it is desired in future to utilize a 3-D IE code that handles finite dipole excitation. Our research, although currently limited to a 2-D primary excitation imposed on a 3-D structure, provides proof-of-concept for this kind of hybrid IE-FE modeling. Practicing engineers and geoscientists can apply this methodology to an existing FE code for modeling the 3-D response to a conductive or resistive inhomogeneity in the presence of a steel wellbore.

CHAPTER V

DISCUSSION AND FUTURE WORK

This chapter discusses the applicability of my research to the petroleum industry and provides recommendations for continuation and future work.

5.1 Discussion

In Chapters 2 and 3 I discussed simulations for downhole CSEM applications. Chapter 2 described a method for combining nuclear magnetic resonance (NMR) with electromagnetic (EM) measurements to improve micro-fracture density estimation in fractured formations. The key aspect for coupling these two techniques comes from simulating the effects of anomalous EM diffusion in fractured media using the EM finite-element (FE) simulator *seatem*. *Seatem* provides quantitative estimates of the fractured formation geologic roughness, β. We found β to show strong sensitivity to fracture density variation, but little to no sensitivity to changes in fracture dimensions. Meanwhile, NMR shows sensitivity to variation in fracture density, thickness, and width. Knowledge of geologic roughness parameters can therefore aid in distinguishing between NMR fracture responses.

Chapter 3 discussed how the simulated β values from *seatem* are combined with surface gas readings and regional geomechanics to high-grade natural fracture corridors and assist in hydraulic fracture stage placement for optimal geologic targeting. Simulating the EM response between hydraulic and natural fractures interactions can

help in determining stimulation placement that can best achieve the desired natural fracture corridor depletion. Optimal stage placement may provide significant production increase in some organic-rich shale reservoirs.

Future work continuing from Chapters 2 and 3 could involve applying the concept of EM fractional diffusion to surface-based CSEM methods. This would require building anomalous diffusion into the existing *seatem* code. The incorporation of anomalous diffusion effects may provide an improved method for quantifying fracture geometry in the far-field. Results could be compared and combined with other far-field fracture mapping methods, such as microseismic and cross-well distributed acoustic sensing (DAS).

In Chapters 4 I described simulations for surface-based CSEM applications. I developed a 2-D integral equation (IE) forward modeling code for modeling the EM response of conductive wellbore casing in the presence of an infinite-line source laid on the surface in alignment with the horizontal casing. The IE simulator was benchmarked and found to be in agreement with results presented in Hohmann (1971) and Coggon (1970). A hybrid IE-FE method was developed using the IE-computed primary EM field solution to precondition the FE simulator. The hybrid method was tested for a simple geological scenario containing idealized fluid-bearing zones. This approach resolves problems associated with modeling the conductive casing problem by removing the wellbore from the FE matrix formulation and placing its effects on the right-side of the linear system as part of the source term. This procedure eliminates the need for an ultra-fine mesh around the wellbore, leading to improved FE solution stability and greatly

reduced computation time. A stable and efficient method to model the response of the conductive wellbore casing is required to implement CSEM simulations for applications such as monitoring hydraulic fracturing fluid flow.

Future work continuing from Chapter 4 could include: modeling the EM response of hydraulic fracturing-induced fluid flow; development of a 3-D IE forward modeling code as an FE/FD preconditioner; and calibrating microseismic data with CSEM responses to improve discrete fracture models. Further details on these research topics are discussed in Future Work below.

5.2 Future work

5.2.1 Modeling the EM Response of Hydraulic Fracturing Fluid Flow

I plan to test the hybrid IE-FE code for modeling the CSEM response of conductive fluid spreading in a realistic oil-field scenario. Although the hybrid IE-FE method does not require refinement around the wellbore casing, local nested-refinement around the fluid zones should be applied within the FE mesh. An improved mesh design is under development to accurately capture the thin dimensions of hydraulic fracturing-induced fluid flow.

5.2.2 Development of a 3-D Integral Equation Forward Modeling Code

I have provided proof-of-concept for the efficacy of the hybrid IE-FE method. However, my approach is currently limited to a 2-D primary excitation imposed on a 3-D electrical conductivity structure. To overcome this restriction, I recommend

developing a fully 3-D IE forward modeling code for incorporation into the hybrid IE-FE method. Transitioning from a 2.5-D to a fully 3-D IE code is required for modeling the wellbore casing response due to a finite dipole excitation as opposed to excitation by an infinite-wire line source. This advancement would more accurately capture a realistic response of the conductive wellbore casing, eventually providing better implementation in industry applications.

One of the current approaches to developing a 3-D integral equation method for CSEM response calculation is described by Orujov et al. (2020) and was developed from Harrington's (1968) method-of-moments (MoM). The latter discretizes the wellbore casing into smaller sections, each treated as an individual dipole source. The interactions between each section are calculated and combined in a solution for the current distribution along the entire casing. Orujov et al. (2020) describe a special wedge element that represents a bent section of pipe. This feature prevents gaps in the geometry, thereby reducing potentially erroneous numerical results (Figure 5.1).

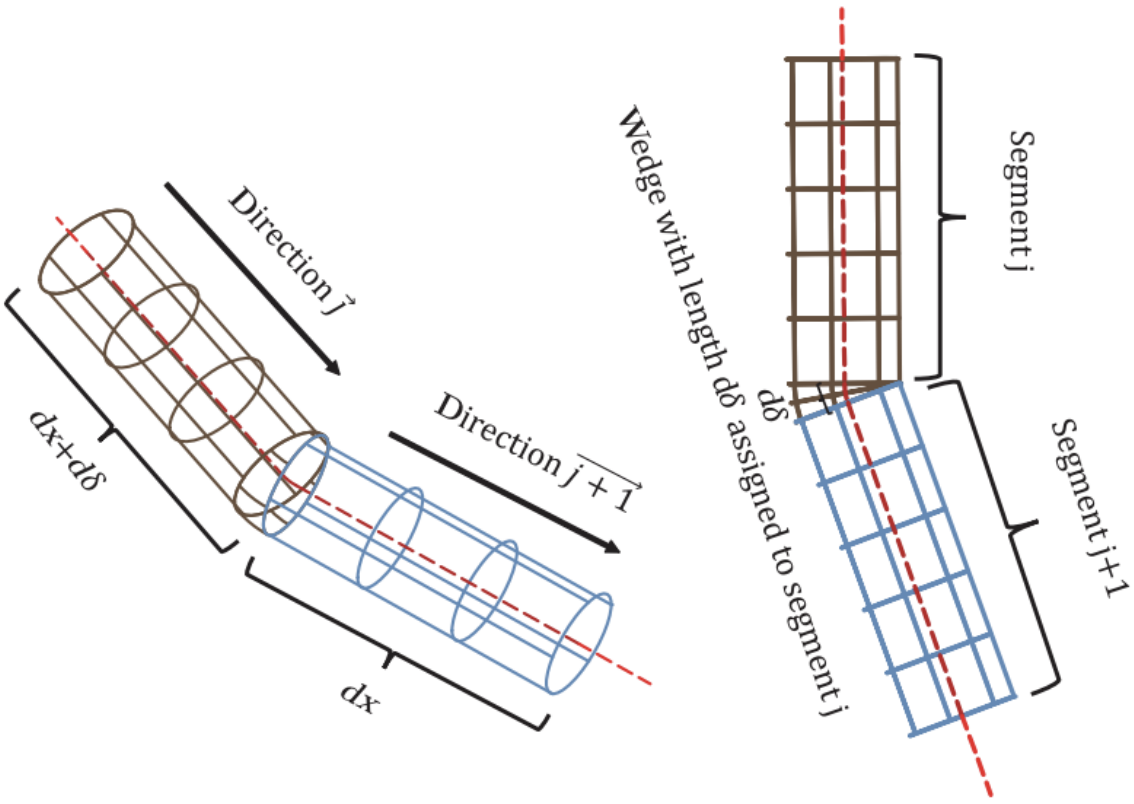

Figure 5.1 – Schematic representation of a bent section of a pipeline with two segments and one wedge. The wedge of length dδ is assigned to segment j and assumed to have the direction j for calculation purposes. Reprinted from Orujov, 2020.

Orujov (2020) tested their method on a 3-m diameter semicircular pipe constructed of alternating straight and wedge elements (Figure 5.2). They found that increasing the number of wedge elements from 60 to 180 reduces the computational memory requirements by a factor of 9, while retaining a solution that closely matches the equivalent solution obtained using COMSOL Multiphysics FE modeling software. A significant limitation of this approach is the restriction of the admissible geometry to a horizontal pipeline system.

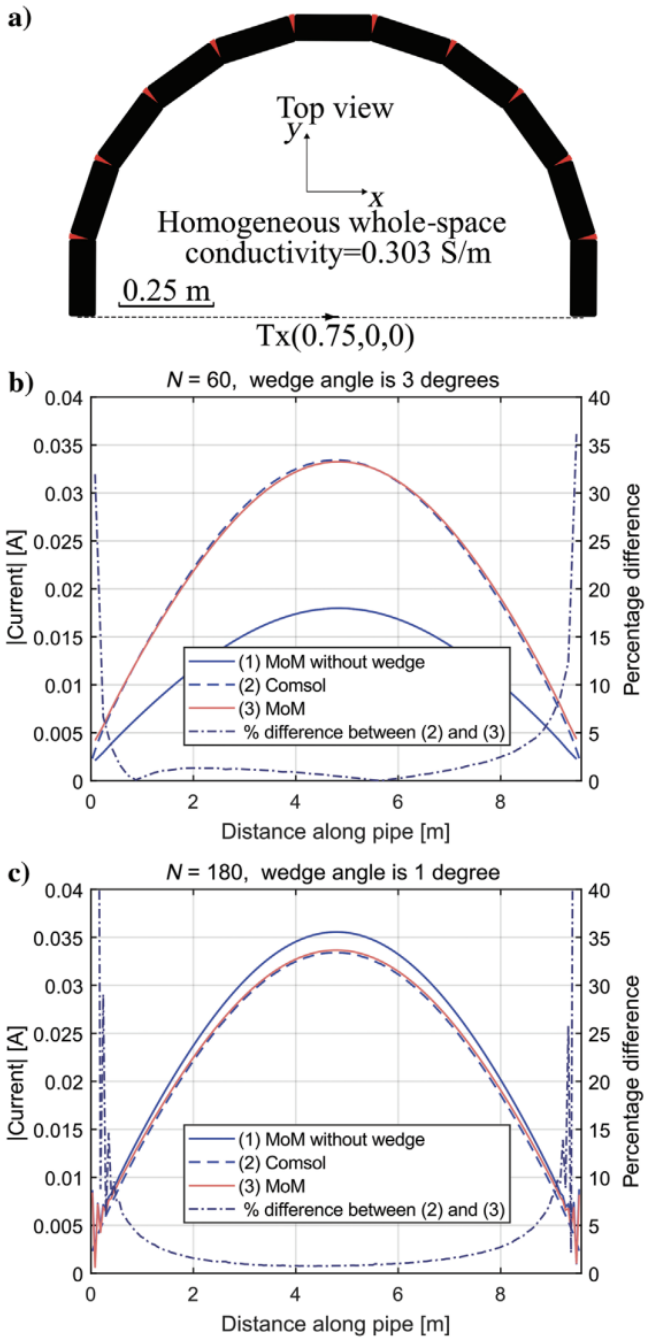

Figure 5.2 – (a) Schematic representation of a semicircular pipe consisting of straight sections (black) and wedge elements (red) buried in a homogeneous space. The transmitter is located at the midpoint of the semicircle and is oriented in the positive x-direction. (b) Current distribution along the pipe obtained using 60 segments, with and without wedge elements (the solid red and blue lines, respectively). (c) Current distribution obtained using 180 segments. Reprinted from Orujov, 2020.

My recommendation is to either reformulate our 2-D IE code into a fully 3-D forward modeling code using the same Hohmann (1971) approach, or expand on the MoM methodology presented by Orujov (2020) to incorporate both vertical and curved sections of the wellbore.

5.2.3 Calibrating Microseismic with CSEM for Discrete Fracture Models

Organic-rich shale reservoirs hold substantial hydrocarbon reserves, but they often require stimulation methods such as hydraulic fracturing to produce at economic rates. Finding effective methods to understand how these types of unconventional formations respond to stimulation is a challenging topic within the oil and gas industry. Modern approaches to simulating the response of unconventional shales include the use of a fully compositional reservoir simulator (Yan et al., 2016), and a quantitative description of the fractures, such as the compartmental embedded discrete fracture model (cEDFM) (Chai et al., 2018). Embedded discrete fracture models (EDFM) are multi-porosity models in which the unfractured porous matrix is fully connected. Rather than conforming the model grid to accommodate a specified fracture geometry, fractures are simply placed in the matrix grid (Figure 5.3).

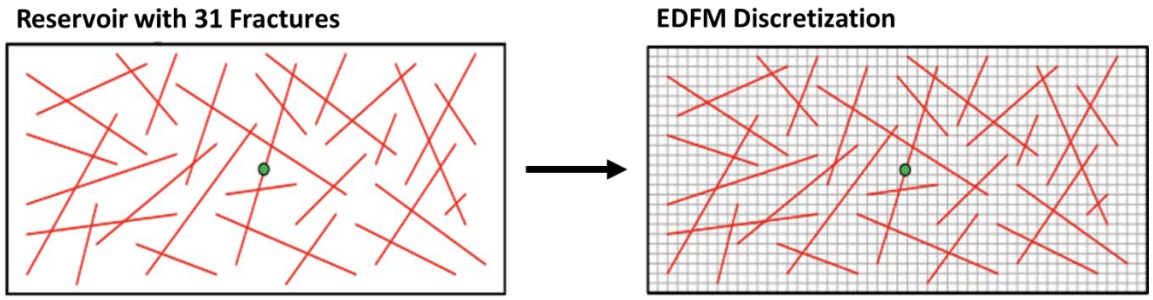

Figure 5.3 – Reservoir with 31 non-orthogonal fractures and EDFM discretization. Modified from Yan, 2017.

The model divides the porous medium into an intact shale matrix and fractures. The former medium is further subdivided into organic matrix "kerogen", an inorganic matrix, and micro-scale "natural fractures" (Figure 5.4).

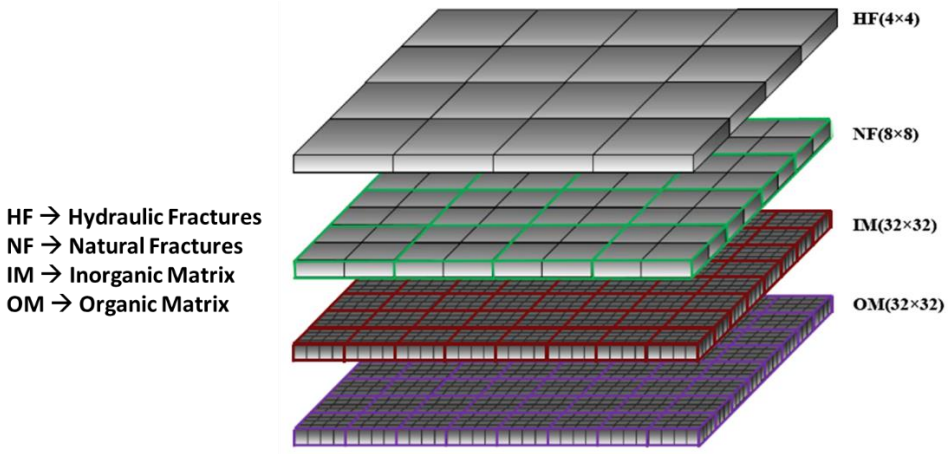

Figure 5.4 – Multi-porosity model with subdivisions. Reprinted from Yan, 2017.

EDFM allows fractures to be easily placed into an existing reservoir geological model. The workflow is first to characterize fracture density and orientation, then populate the grid with fractures and refine the former to capture important features. Next, fine-scale modeling is performed to capture the important physics. Finally, add multiple porosity/permeability media transfer functions for upscaling the physics. The placement of fractures within the EDFM workflow is typically accomplished by either manual input or population from microseismic data. An example of the latter type of fracture placement is shown in Figure 5.5.

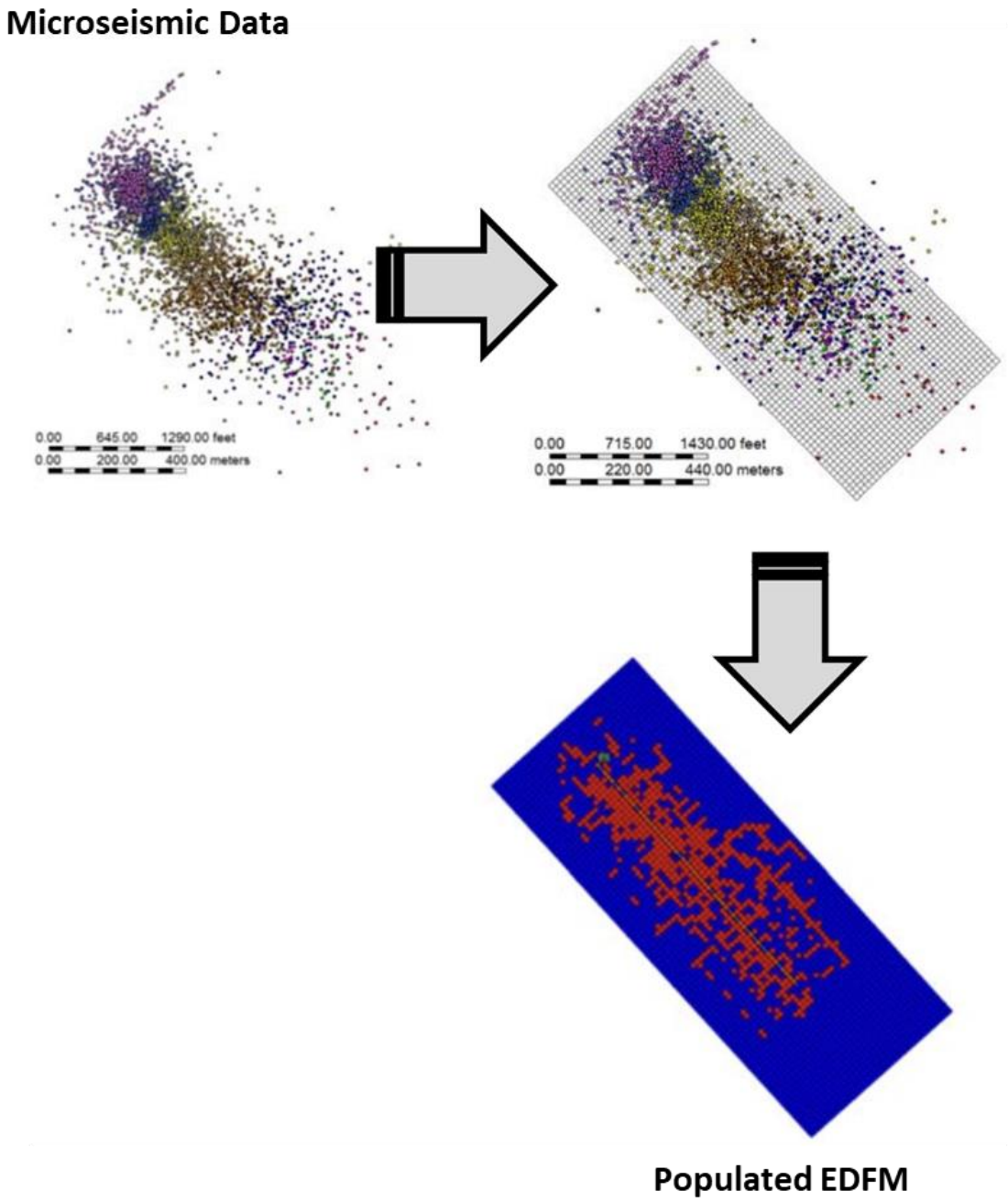

Figure 5.5 – Workflow for populating EDFM from seismic data, seismic events are spatially bounded and overlaid on a frame of structured gridblocks and fracture gridblocks are activated with one or more seismic events located inside. Reprinted from Alfi, 2018.

Stimulated reservoir volume (SRV) calculations using cEDFM or similar methods may be improved by placing fractures according to information provided by microseismic data. However, significant uncertainty accrues to this strategy. Microseismic data convey the location and intensity of fractures after a well completion, but provide limited information about the fluid distribution and production pathway back to the wellbore. Even if production and fiber optic (e.g. DAS) data are available, the results are somewhat inconclusive as to precisely which pathways convey the hydraulic fracturing fluid. Coupling controlled-source electromagnetic (CSEM) data with reservoir simulation may be an important factor to reducing the uncertainties related to hydraulic fracture fluid distribution and flow paths.

Integrating CSEM responses into fracture modeling for unconventional reservoir simulation may help reduce model-parameter uncertainty and improve understanding of the underlying fluid-flow physics. Using a time-lapsed 3-D approach, CSEM responses can be analyzed to reveal information about fluid-flow pathways and locations of fluid-filled fractures. In an oilfield setting, CSEM operations should begin before hydraulic fracturing to calibrate for the largely unknown, complex background noise. CSEM monitoring should continue through the initial flowback period. Using the hybrid IE-FE method, one might be able to evaluate expected CSEM responses during stimulation and compare them to the actual responses acquired during the flowback period. This comparison may yield some information about the pathway of conductive fracturing fluids during the completion and the initial production stage. Additionally, by analyzing the evolution of CSEM responses over time, one may be able to detect areas where the

fracture network has closed off, leaving conductive fluids behind. This information can be used as a constraint for conditioning the microseismic data that is used to populate EDFM. A proposed workflow for combining time-lapse CSEM simulations with microseismic data to improve SRV calculations from discrete fracture models is shown in Figure 5.6. It is hoped that CSEM methods eventually can be developed to enable accurately monitoring hydraulic fracturing fluid-flow.

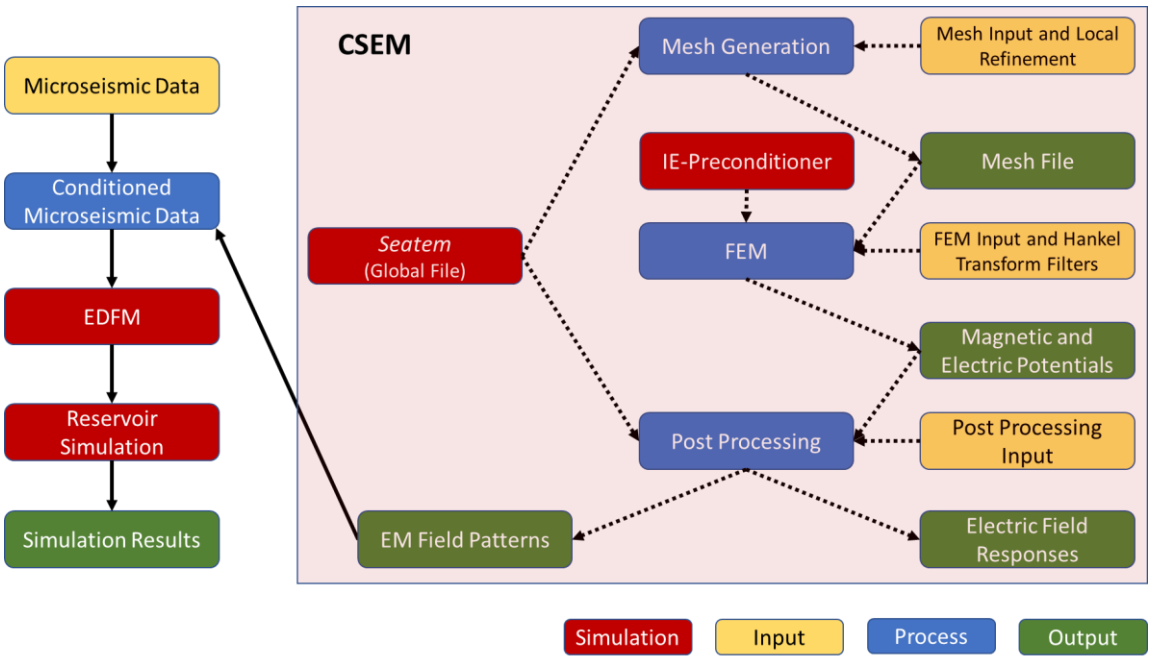

Figure 5.6 – Workflow for improving SRV calculations from discrete fracture model using CSEM.

CHAPTER VI

CONCLUSIONS

This chapter summarizes the major results and conclusions of the work presented in this dissertation.

6.1 Summary

The main technical contributions from this dissertation are summarized below:

1. A method for combining nuclear magnetic resonance (NMR) with controlled-source electromagnetic (CSEM) fractional diffusion simulations was established, and its viability for determining micro-fracture density in fractured formations was investigated.
2. A method for combining surface gas measurement and regional geomechanics with CSEM fractional diffusion simulations was developed, and its application for high-grading natural fracture corridors was investigated.
3. Simulations of the EM response between hydraulic and natural fracture interactions were used in determining hydraulic fracturing stimulation placement for natural fracture corridor depletion.
4. A 2-D integral equation (IE) forward modeling code was developed for simulating the EM response of conductive wellbore casing in simple oil-field scenarios.

5. A hybrid IE-FE method was developed using the IE-computed primary EM field solution to precondition our in-house FE simulator, and its accuracy and computational efficiency was tested in a simple oil-field scenario containing idealized fluid-bearing zones.

6.2 Conclusions

The numerical simulation and theoretical analysis results from this dissertation led to the conclusions listed below:

1. CSEM anomalous diffusion shows significant sensitivity to fracture density with minimal sensitivity to fracture dimensions.
2. Combining CSEM anomalous diffusion with the NMR analytical model for fracture-pore coupling improves micro-fracture density estimation by distinguishing between fracture density and dimensions in NMR T_2 distribution.
3. Quantifying the spatial distribution geologic host-formation roughness through generated induction logs can differentiate between induction log responses of high and low fracture concentrations.
4. Optimal stimulation zones for fracture corridor depletion were observed to be carbonate or organic shale formations having a geologic roughness (β) value greater than 0.3.
5. The developed 2-D IE forward modeling code can comfortably handle high conductivity contrasts between the wellbore casing and surrounding host formation.

6. A consistent scaling argument was found for the computed scattered magnetic field (H_z^S) providing equivalent solutions for varying pipe diameters. This enables precomputing of the primary field solution prior to hydraulic fracturing operations.
7. The conductive wellbore casing acts as a source of earth return current that is nearly the same strength and exactly opposite in direction to the transmitter current. This indicates that the casing cancels out the primary field and subsurface heterogeneity response would be the main contribution measured by receivers.
8. The 2-D IE simulator provides a stable primary source solution to the FE method.
9. Preconditioning the FE method with an IE primary source solution removes the need for an ultra-fine FE mesh around the wellbore, improving FE solution stability and greatly reducing FE computation time (85-91% reduction).
10. Similar solver convergence rates for IE-FE and standalone-FE suggest that the IE preconditioning has little effect on the run-time of the FE linear system solver. Additionally, this indicates that the IE-preconditioning does not degrade the FE matrix conditioning.

REFERENCES

Ahmed, T, 2010. Reservoir Engineering Handbook, fourth edition. Burlington, Massachusetts: Gulf Professional Publishing/Elsevier.

Alfi, M., 2018, Multi Porosity Models in Shales: Flow Behavior and Improved Recovery. PhD dissertation, Texas A&M University, College Station, Texas.

Anderson F. J. 2011. North Dakota Geological Survey. Denver, Colorado: Rocky Mountain Association of Geologists, 576-92.

Badea, E. A., Everett M. E., Newman G. A., Biro O., 2001, Finite-element analysis of controlled-source electromagnetic induction using Coulomb-gauged potentials: Geophysics, 66, 786–799, doi: 10.1190/1 .1444968.

Beskardes, G. D., McAliley, W. A., Ahmadian, M., Chapman, D. T., Weiss, C. J., Heath, J. E., 2019, Power Density Distribution in Subsurface Fractures Due to an Energized Steel Well-casing Source: Journal of Environmental & Engineering Geophysics, 24(2), 285–297, doi: 10.2113/JEEG24.2.285.

Bespalov, A. 2009. 3D induction log simulation with octree fractal grids. Paper presented at the 2009 SEG International Exposition and Annual Meeting, Houston, Texas.

Biro, O., and Preis, K., 1989, On the use of the magnetic vector potential in the finite element analysis of three-dimensional eddy currents: IEEE Trans. Magn., 25, 3145–3159.

Blunt, M. J., Bijeljic, B., Dong, H., et al. 2013. Pore-scale Imaging and Modeling. Advances in Water Resources 51: 197-216.

Bour, O., Davy, P., 1999, Clustering and size distributions of fault patterns: theory and measurement: Geophysical Research Letters, 26(13), 2001-2004. doi: 10.1029/1999GL900419.

Bray, H. 2013. Forward Modeling of the Induction Log Response of a Fractured Geologic Formation. MS thesis, Texas A&M University, College Station, Texas.

Castillo Reyes, O., Queralt, P., Marcuello, A., Ledo, J., 2022, Land CSEM Simulations and Experimental Test Using Metallic Casing in a Geothermal Exploration Context: Vallès Basin (NE Spain) Case Study: IEEE Transactions on Geoscience and Remote Sensing, 60, 1-13, doi: 10.1109/TGRS.2021.3069042.

Chai, Z., Tang, H., He, Y., Killough, J., & Wang, Y, 2018, Uncertainty Quantification of the Fracture Network with a Novel Fractured Reservoir Forward Model. Society of Petroleum Engineers. doi:10.2118/191395-MS.

Chave, A. D., Everett, M. E., Mattsson, J., Boon, J., Midgley, J., 2017, On the physics of frequency-domain controlled source electromagnetics in shallow water. 1: isotropic conductivity: Geophysical Journal International, 208(2), 1026-1042, doi: 10.1093/gji/ggw435.

Chen, S., Georgi, D., Fang, S., Salyer, J., and Shorey, D. 1999. Optimization of NMR Logging Acquisition and Processing. Presented at the SPE Annual Technical Conference and Exhibition. SPE 56766.

Chew, W. C., Barone, S., Anderson, B., and Hennessy, C. 1984. Diffraction of Axisymmetric Waves in a Borehole by Bed Boundary Discontinuities. Geophysics 49 (10):1586-1595.

Chi, L., Elliott, M., Heidari, Z., and Everett, M.E. 2014. Assessment of micro-fracture density using combined interpretation of NMR relaxometry and electromagnetic logs. Paper presented at the 2014 Unconventional Resources Technology Conference, Denver, Colorado, 25-27 August.

Chi, L., and Heidari, Z., 2014, Quantifying the Impact of Natural Fractures and Pore Structure on NMR Measurements in Multiple-Porosity Systems. Paper presented at the International Petroleum Technology Conference, Doha, Qatar, 20-22 January.

Coates, G. R., Xiao, L., and Prammer, M. G. 1999. NMR Logging Principles and Applications. Halliburton Energy Services.

Coggon, J. H., 1971, Electromagnetic and electrical modeling by the finite element method: Geophysics, 36, 132–155, doi: 10.1190/1.1440151.

Couchman, M. J., Everett, M. E., 2022, Feasibility of a Surface-Based Controlled Source Electromagnetic Method for Detection of Buried Pipelines and Corrosion Effects: Journal of Infrastructure Systems, 28(2), doi: 10.1061/(ASCE)IS.1943-555X.0000686.

Cuevas, N., Pezzoli O., 2018, On the effect of the metal casing in surface-borehole electromagnetic methods: Geophysics, 83, no. 3, E173– E187, doi: 10.1190/geo2017-0055.1.

Everett, M. E. 2009. Transient Electromagnetic Response of a Loop Source over a Rough Geological Medium. Geophy. J. Int. 177: 421-429.

Everett, M. E., 2013, Near-Surface Applied Geophysics: Cambridge University Press.

Everett, M. E., Chave, A. D., 2009, On the physical principles underlying electromagnetic induction: Geophysics, 84, no. 5, W21-W32, doi: 10.1190/GEO2018-0232.1.

Everett, M. E., Badea, E. A., Shen, L. C., Merchant, G. A., Weiss, C. J., 2001, 3-D finite element analysis of induction logging in a dipping formation: IEEE Transactions on Geoscience and Remote Sensing, 39(10), 2244-2252, pii: S 0196-2892(01)08127-X.

Ge, J., 2014, Fractional Diffusion Modeling of Electromagnetic Induction in Fractured Rocks. PhD dissertation, Texas A&M University, College Station, Texas.

Grant, F. S., West, G. F., 1965, Interpretation Theory in Applied Geophysics: McGraw-Hill Book Co.

Gupta, A., A. Datta-Gupta, and King, M.J., 2010, Geology-based Reservoir Model Building for Carbonate Reservoirs: A Project Founded by Qatar National Research Found (QNRF), Cycle 4.

Guptasarma, D., and Singh, B., 1997, New digital filters for Hankel transform J0 and J1 transforms: Geophys. Prosp., 45, 745–762.

Harrington, R., 1968, Field computation by moment methods: MacMillan.

Heagy, L. J., Oldenburg, D. W., 2019, Modeling electromagnetics on cylindrical meshes with applications to steel-cased wells: Computers & Geosciences, 125, 115-130, doi: 10.1016/j.cageo.2018.11.010.

Hibbs, A.D. 2014. Evaluation of deep surface resistivity imaging for hydrofracture monitoring. Period report, U.S. Department of Energy, Period Covered: Jan. 1, 2014 to March 31, 2014.

Hohmann, G. W., 1971, Electromagnetic scattering by conductors in the earth near a line source of current: Geophysics, 36, 101–131, doi: 10 .1190/1.1440150.

Hu, Y., Yang, D., Li, Y., Wang, Z., & Lu, Y., 2022, 3-D Numerical Study on Controlled Source Electromagnetic Monitoring of Hydraulic Fracturing Fluid With the Effect of Steel-Cased Wells: IEEE Transactions on Geoscience and Remote Sensing, 60, 1-10, doi: 10.1109/TGRS.2021.3100774.

Jones, D., Pieprzica, C., Vasquez, O., Oberle, J., Morton, P., Santiago, T. III, Hickey, M., 2019, Monitoring Hydraulic Fracture Flowback in the Permian Basin Using Surface-Based Controlled-Source Electromagnetics: URTEC-2019-230-MS, doi 10.15530/urtec-2019-230.

Kaufman, A. A., 1965, Theory of Induction Logging: Novosibersk, Siberian Dept. of Nauka Press.

Kenyon, W. E., Day, P. I., Straley, C., and Willemsen, J. F. 1988. A Three Part Study of NMR Longitudinal Relaxation Properties of Water-saturated Sandstones. SPE Formation Evaluation 3 (3): 622 -636.

Kohnke, C., L. Liu, R. Streich, Swidinsky A., 2018, A method of moments approach to model the electromagnetic response of multiple steel casings in a layered earth: Geophysics, 83, no. 2, WB81–WB96, doi: 10 .1190/geo2017-0303.1, doi: 10.1190/GEO2017-0303.1.

Liu, R., R. Guo, J. Liu, C. Ma, Guo Z., 2018, A hybrid solver based on the integral equation method and vector finite-element method for 3D controlled-source electromagnetic method modeling: Geophysics, 83, no. 5, E319–E333, doi: 10.1190/geo2017-0502.1.

Metzler, R., Klafter, J., 2000, The random walk's guide to anomalous diffusion: a fraction dynamics approach: Phys. Rep., 339, 1-77.

Moran, J. H., Kunz, K., 1962, Basic theory of induction logging and application to study of two-coil sondes: Geophysics, 27, no. 6, 829-858.

Mostaghimi, P., Blunt, M. J., and Bijeljic, B. 2012. Computations of Absolute Permeability on Micro-CT Images. Mathematical Geosciences 45 (1): 103-125.

Norbeck, J., Fonseca, E., Griffiths, D.V., Wong, S., 2012. Natural fracture identification and characterization while drilling underbalanced. Paper presented at the 2012 SPE Americas Unconventional Resources Conference, Pittsburgh, Pennsylvania.

Øren, P. E. and Bakke, S. 2002. Process-based Reconstruction of Sandstones and Prediction of Transport Properties. Transport in Porous Media 46: 311-343.

Orujov, G., E. Anderson, R. Streich, Swidinsky A., 2020, On the electromagnetic response of complex pipeline infrastructure: Geophysics, 85, no. 6, E241–E251, doi: 10.1190/geo2020-0050.1.

Pardo, D., Torres-Verrdin, C., Paszynski, M., 2007. Numerical simulation of 3D EM borehole measurements using an hp-adaptive goaloriented finite element formulation. Paper presented at the 2007 SEG Annual Meeting, San Antonio, Texas.

Patzer, C., K. Tietze, Ritter O., 2017, Steel-cased wells in 3-D controlled source EM modeling: Geophysical Journal International, 209, 813–826, doi: 10.1093/gji/ggx049.

Paulsen, K. D., and Lynch, D. R., 1991, Elimination of vector parasites in finite element Maxwell solutions: IEEE Trans Micro. Theory Tech., 39, 395–404.

Press, W., Teukolsky, S., Vetterling, W., Flannery, B., 1992, Numerical Recipes in Fortran 77: Cambridge University Press.

Puzyrev, V., E. Vilamajó, P. Queralt, J. Ledo, Marcuello A., 2017, Three-dimensional modeling of the casing effect in onshore controlled-source electromagnetic surveys: Surveys in Geophysics, 38, 527–545, doi: 10.1007/s10712-016-9397-8.

Ramakrishnan, T.S., Schwartz, L.M., Fordham, E.J., and Wilkinson, D.J. 1998. Forward Models for Nuclear Magnetic Resonance in Carbonate Rocks. Presented at the SPWLA 39th Annual Logging Symposium. SPWLA-1998-SS.

Ramakrishnan, T.S., Schwartz, L.M., Fordham, E.J., and Wilkinson, D.J. 1999. Forward Models for Nuclear Magnetic Resonance in Carbonate Rocks. The Log Analyst 40 (4): 260-270.

Schlumberger, 1969, Log interpretation principles. Schlumberger Limited, New York, NY: 25-28.

Sher, H. and Montroll, E.W. 1975. Anomalous Transit-time Dispersion in Amorphous Solids. Phy. Rev. B 12: 2455- 2477.

Stalnaker, J., 2004, A finite element approach to the 3D CSEM modeling problem and applications to the study of the effect of target interaction and topography, PhD dissertation, Texas A&M University, College Station, TX.

Streich, R., 2016, Controlled-Source Electromagnetic Approaches for Hydrocarbon Exploration and Monitoring on Land: Surveys in Geophysics, 37, 47-80, doi: 10.1007/s10712-0159-9336-0.

Tabbara, M., T. Blacker, Belytschko T., 1994, Finite element derivative recovery by moving least square interpolants: Computer Methods in Applied Mechanics & Engineering, 117, 211–223, doi: 10.1016/0045-7825 (94)90084-1.

Talabi, O.A. 2008. Pore-scale Simulation of NMR Response in Porous Media. PhD Dissertation, Imperial College London.

Talabi, O., AlSayari, S., Iglauer, S., and Blunt, M.J. 2009. Pore-scale Simulation of NMR Response. Journal of Petroleum Science and Engineering 67 (3-4): 168-178.

Tang, W., Y. Li, A. Swidinsky, Liu J., 2015, Three-dimensional controlled-source electromagnetic modelling with a well casing as a grounded source: A hybrid method of moments and finite element scheme: Geophysical Prospecting, 63, 1491–1507, doi: 10.1111/1365-2478.12330.

Toumelin, E., Torres-Verdín, C., and Chen, S. 2003. Modeling of Multiple Echo-time NMR Measurements for Complex Pore Geometries and Multiphase Saturations. SPE Reservoir Evaluation & Engineering 6 (4): 234- 243. SPE 85635.

Um, E. S., Jihoon K., Wilt M., 2020, 3D borehole-to-surface and surface electromagnetic modeling and inversion in the presence of steel infrastructure: Geophysics 85.5 (2020):E139-E152, doi: 10.1190/GEO2019-0034.1.

Wait, J. R., 1962, Electromagnetic waves in stratified media: MacMillan.

Wait, J. R., 1984, General Formulation of the Induction Logging Problem for Concentric Layers About the Borehole: IEEE Transactions on Geoscience and Remote Sensing, Vol GE-22, No. 1.

Weiss, C., 2017, Finite-element analysis for model parameters distributed on a hierarchy of geometric simplices: Geophysics, 82, no. 4, E155–E167, doi: 10.1190/geo2017-0058.1.

Weiss, C. J., Everett, M.E. 2007. Anomalous diffusion of electromagnetic eddy currents in geological formations. Journal of Geophysical Research 112: B08102.

Wilt, M., E. S. Um, E. Nichols, C. Weiss, G. Nieuwenhuis, MacLennan K., 2020, Casing integrity mapping using top-casing electrodes and surface based electromagnetic fields: Geophysics, 85, no. 1, E1– E13, doi: 10.1190/geo2018-0692.1.

Yan, B., 2017, Development of General Unstructured Reservoir Utility and Fractured Reservoir Modeling. PhD dissertation, Texas A&M University, College Station, Texas.

Yan, B., Alfi, M., An, C., Cao, Y., Wang, Y., Killough, J.E., 2016a. General Multi-Porosity simulation for fractured reservoir modeling. J. Nat. Gas Sci. Eng. 33, 777–791. doi:10.1016/j.jngse.2016.06.016.

Yu, N., Gao, L., Li, R., Wu, X., Wang, E., 2022, A Hybrid Grid-Based Finite Element Approach For 3D Steel Casing Forward Modeling: Advanced Theory & Simulations. Feb2022, Vol. 5 Issue 2, p1-11, doi: 10.1002/adts.202100398.

APPENDIX A

ELECTROMAGNETIC ANOMALOUS DIFFUSION

Appendix A provides a brief overview of the mathematical development of electromagnetic (EM) anomalous diffusion used in this dissertation. See Ge (2014) and Everett (2009) for a more in-depth review of the mathematical formulation. Starting with the vector form of Ohm's law (A-1):

$$J = \sigma \mathrm{E} \qquad (\mathrm{A}-1)$$

where J is the current density, σ is the electrical conductivity, and E is the electric field. The time-convolutional integral form of Ohm's law can then be written as:

$$J = \sigma_\beta * \mathrm{E} \equiv \int_0^t \frac{\mathrm{d}t' \sigma_\beta \mathrm{E}(t)}{(t-t')^{1-\beta}} \qquad (\mathrm{A}-2)$$

where σ_β is a generalized conductivity, E is the electric field, β is the geologic roughness parameter. The β parameter ranges from 0 to 1 where 0 indicates no geologic roughness or Brownian motion, and a value approaching 1 shows a subdiffusion response in the electromagnetic current. Equation (A-2) is derived from the Continuous-time Random Walk (CTRW) approach for a charge carrier undergoing a random walk in a fractal

geoelectrical network. A power law probability density function of $t^{1-\beta}$ is used for the waiting time.

From Maxwell's equations, Faraday's law of induction (Equation A-3) is left unchanged while Ampère's circuital law "with Maxwell's additions" (Equation A-4) is generalized neglecting the displacement current (Equation A-5).

$$\nabla \mathrm{X}\, \mathrm{E} = -\frac{\partial B}{\partial t} \qquad (\mathrm{A}-3)$$

$$\nabla \mathrm{X}\, \mathrm{B} = \mu_0 (J + \varepsilon_0) \frac{\partial B}{\partial t} \qquad (\mathrm{A}-4)$$

$$\nabla \mathrm{X}\, \mathrm{B} = \mu_0 \sigma_\beta * \mathrm{E} + \mu_0 J_s(t) \qquad (\mathrm{A}-5)$$

where E is the electric field, B is the magnetic field, μ_0 is permeability of free space, ε_0 is the permittivity of free space, and $J_s(t)$ represents the source term.

The generalized Ampère's law is combined with Faraday's law to eliminate the magnetic field, B. This results in a fractional vector diffusion equation with an analytic solution for a uniform rough half-space or stack of rough layers.

$$\nabla\times\nabla\times\mathrm{E} = -\mu_0 \sigma_\beta \, {}_0D_t^{1-\beta} E(t) - \mu_0 \frac{\partial}{\partial t} J_s \qquad (\mathrm{A}-5)$$

where *E* is the external electric field, μ_0 represents magnetic permeability of free space, σ_β is the generalized conductivity, D_t is the fractional diffusion operator, β is the waiting

time distribution for the CTRW model (geologic roughness parameter), and J_s indicates the source current density.

Equation (A-5) contains the Riemann-Liouville fractional operator as introduced by Metzler and Klafter (2000) and can be expressed as:

$$ {}_0\mathrm{D}_t^{1-\beta}\mathrm{E}(t) = \frac{1}{\Gamma(\beta)}\frac{\partial}{\partial t}\int_0^t \frac{\mathrm{E}(t')dt'}{(t-t')^{1-\beta}} \qquad (\mathrm{A}-6) $$

where Γ is the Gamma function serving as a normalizing constant.

APPENDIX B

COULOMB-GAUGED POTENTIAL FORMULATION FOR CSEM INDUCTION

Appendix B provides a brief overview of the coulomb-gauge formulation for the finite-element method used in this dissertation. See Badea et. al (2001) for a more in-depth review of the mathematical formulation. The diffusive Maxwell equations for electric and magnetic fields at low frequencies can be written as:

$$\nabla \mathrm{X}\, \mathrm{E} = \mathrm{i}\omega\mu_0 \mathrm{H} \qquad (\mathrm{B}-1)$$

$$\nabla \mathrm{X}\, \mathrm{H} = \mathrm{J} = \mathrm{J_s} + \sigma \mathrm{E} \qquad (\mathrm{B}-2)$$

where ω is the angular frequency, μ_0 is the permeability of free space, $\sigma(r)$ is the spatially varying electrical conductivity of the geological formation under investigation, J is the electric current density, J_s is an electric current density source term, and σE is an ohmic conduction term.

Expressing equations (B-1) and (B-2) in EM field (E, H), we get the coupled vector-scalar potential formulation (A, Φ) for conductive non-magnetic geomaterials with $\sigma=\sigma(r)$ and $\mu=\mu 0$:

$$\mathrm{B} = \nabla \mathrm{X}\ \mathrm{A} \qquad (\mathrm{B}-3)$$

$$\mathrm{E} = -\mathrm{i}\omega \mathrm{A} - \nabla\Phi \qquad (\mathrm{B}-3)$$

where $\Phi \equiv -i\omega\Psi$ is the reduced scaler potential.

Recasting equation (B-2) in terms of EM potentials and adding the term $-\nabla(\nabla \cdot A)$ to the left-hand side of the equation gives the curl-curl equation:

$$\nabla X \nabla X A - \nabla(\nabla \cdot A) - i\omega\mu_0\sigma(A + \nabla\Psi) = -\mu_0 J_s \qquad (B-4)$$

The added term is included to avoid numerical difficulties following the approach described in Biro and Preis (1989). Applying the vector identity $\nabla X \nabla X A - \nabla(\nabla \cdot A) = -\nabla^2 A$ shows that equation (B-4) is equivalent to the Helmholtz equation.

$$\nabla^2 A + i\omega\mu_0\sigma(A + \nabla\Psi) = -\mu_0 J_s \qquad (B-5)$$

Equation (B-4) is replaced by the following axillary equation to maintain a divergence free current density.

$$\nabla \cdot [i\omega\mu_0\sigma(A + \nabla\Psi)] \qquad (B-6)$$

Equations (B-5) and (B-6) are solved simultaneously and valid within the solution domain Ω. This constitutes the incompletely gauged (A, Ψ) coupled vector-scalar potential formulation of Maxwell's equations. Taking the divergence of equation (B-4) reveals that the divergence of vector potential A satisfies the Laplace's equation

everywhere within the solution domain Ω. The governing equations (B-5) and (B-6) are then defined with their secondary potentials to become:

$$\nabla^2 A + i\omega\mu_0\sigma(A_s + \nabla\Psi_s) = i\omega\mu_0\sigma\left(A_p + \nabla\Psi_p\right) \qquad (B-7)$$

$$\nabla \cdot [i\omega\mu_0\sigma(A_s + \nabla\Psi_s)] = -\nabla \cdot \left[i\omega\mu_0\sigma\left(A_p + \nabla\Psi_p\right)\right] \qquad (B-8)$$

Next, a boundary condition is applied such as the homogeneous Dirichlet boundary condition:

$$(A_s + \nabla\Psi_s) \equiv (0,0) \text{ on } \Gamma \qquad (B-9)$$

where Γ is the outer boundary.

The primary potentials (A_p, Ψ_p) are then given by the Hankel transform:

$$A_p(r) = A_p(\rho, z)\hat{\emptyset} = \frac{\mu_0 I A \hat{\emptyset}}{2}\int_{\alpha_0}^{\infty}\frac{1}{\alpha_0}\exp(-\alpha_0|z - z_S|)J_1(\lambda a)J_1(\lambda\rho)\lambda d\lambda \qquad (B-10)$$

where $\hat{\emptyset}$ is the unit vector in the azimuthal direction, z is the vertical position on the cylindrical solution domain Ω, $\alpha_0^2 = \lambda^2 - i\mu_0\sigma_0\omega$, J_1 is the Bessel function of order one. Hankel transforms can be calculated using the digital filter method proposed by Guptasarma and Singh (1997). Finite-element analysis is performed in Cartesian coordinates and the vector Laplacian operator decomposes into three scalar

Laplacian operators to simplify assembling the finite-element matrix. The secondary magnetic vector potential A_s can then be written as:

$$A_s = A_{sx}\hat{x} + A_{sy}\hat{y} + A_{sz}\hat{z} \qquad (B-11)$$

The governing equations (B-7) and (B-8) then become the weak formulation of the coupled potential boundary value problem:

$$\begin{aligned}
&\nabla^2 A_{sx} + i\omega\mu_0\sigma\left(A_{sx} + \frac{\partial \Psi_s}{\partial x}\right) = i\omega\mu_0\Delta\sigma A_{px} \\
&\nabla^2 A_{sy} + i\omega\mu_0\sigma\left(A_{sy} + \frac{\partial \Psi_s}{\partial x}\right) = i\omega\mu_0\Delta\sigma A_{py} \qquad (B-12) \\
&\nabla^2 A_{sz} + i\omega\mu_0\sigma\left(A_{sz} + \frac{\partial \Psi_s}{\partial x}\right) = i\omega\mu_0\Delta\sigma A_{pz} \\
&i\omega\mu_0\sigma\left(\frac{\partial \sigma A_{sx}}{\partial x} + \frac{\partial \sigma A_{sy}}{\partial y} + \frac{\partial \sigma A_{sz}}{\partial z}\right) + i\omega\mu_0\sigma\nabla\cdot[\sigma\Psi_s] = -i\omega\mu_0\sigma\nabla\cdot\left[\sigma A_p\right]
\end{aligned}$$

Equation (B-12) is then multiplied by the test function $\eta(r)$ and integrated by parts over the solution domain Ω using Green's formula and a related identity.

$$-(\Delta\eta, A_{sx})_\Omega = i\omega\mu_0\left(\sigma\eta, A_{sx} + \frac{\partial\Psi_s}{\partial x}\right)_\Omega = -i\omega\mu_0(\Delta\sigma\eta, A_{px})_\Omega$$

$$-(\Delta\eta, A_{sy})_\Omega = i\omega\mu_0\left(\sigma\eta, A_{sy} + \frac{\partial\Psi_s}{\partial x}\right)_\Omega = -i\omega\mu_0(\Delta\sigma\eta, A_{py})_\Omega \qquad (B-13)$$

$$-(\Delta\eta, A_{sz})_\Omega = i\omega\mu_0\left(\sigma\eta, A_{sz} + \frac{\partial\Psi_s}{\partial x}\right)_\Omega = -i\omega\mu_0(\Delta\sigma\eta, A_{pz})_\Omega$$

$$i\omega\mu_0\sigma\left(\eta, \frac{\partial\sigma A_{sx}}{\partial x} + \frac{\partial\sigma A_{sy}}{\partial y} + \frac{\partial\sigma A_{sz}}{\partial z}\right)_\Omega - i\omega\mu_0(\sigma\nabla\eta, \nabla\Psi_s)_\Omega = i\omega\mu_0(\sigma\nabla\eta, A_p)_\Omega$$

APPENDIX C

INTEGRAL EQUATION METHOD

Appendix C provides a brief overview of the Integral Equation method used in this paper. See Hohmann (1971) for a more in-depth review of the mathematical formulation. The frequency dependent Maxwell's equations in mks units can be written as:

$$-\nabla \mathrm{X}\, \mathrm{E} = \hat{z}\mathrm{H} + \mathrm{M_i} \qquad (\mathrm{C}-1)$$

$$\nabla \mathrm{X}\, \mathrm{H} = \hat{y}\mathrm{E} + \mathrm{J_i} \qquad (\mathrm{C}-2)$$

where E is the electric field, H is the magnetic field, $\mathrm{M_i}$ describes the impressed magnetic current, $\mathrm{J_i}$ describes the impressed electric current, $\hat{z}$ is the impedivity, and $\hat{y}$ is the admittivity. Impedivity and admittivity can be described through the inductivity (μ), conductivity (σ), and permittivity (ε) as follows:

$$\hat{z} = i\omega\mu;\ \hat{y} = \sigma + i\omega\varepsilon$$

Equations (C-1) and (C-2) can then be rewritten to obtain the integral equation solutions for electromagnetic scattering as follows:

$$-\nabla \mathrm{X}\, \mathrm{E} = \hat{z} * \mathrm{H} + \mathrm{M_s} + \mathrm{I_i} \qquad (\mathrm{C}-3)$$

$$\nabla \mathrm{X}\, \mathrm{H} = \hat{y} * \mathrm{E} + \mathrm{J_s} + \mathrm{I} \qquad (\mathrm{C}-4)$$

where the scattering currents are described by

$$M_s = (\hat{z} - \hat{z}_*)H;\ J_s = (\hat{y} - \hat{y}_*)H$$

given $\hat{z}_*$ and $\hat{y}_*$ to be the normal values of impedivity and admittivity in each region.

Next, a line source carrying current I is placed along the surface y-axis. A uniform half-space with constant conductivity and permittivity is assumed, except within the inhomogeneity region, and magnetic scattering currents are neglected. The electric field then exists everywhere within the y-direction. By combining Equations (A-5) and (A-6) the Helmholtz equation in E_y is obtained:

$$(\nabla^2 + k^2)E_y = i\omega\mu_0(J_s + J_i) \qquad (C-5)$$

where

$$k^2 = -\hat{z}_*\hat{y}_* = \omega^2\mu_0\varepsilon_* - i\omega\mu_0\sigma_*$$

In the air above the half-space, the permittivity $\varepsilon_* = \varepsilon_0$ and the conductivity $\sigma_* = 0$, while throughout the half-space to be the normal values of $\varepsilon_* = \varepsilon_1$ and $\sigma_* = \sigma_1$.

The incident and scattered electric fields then satisfy the following differential equations in each region:

$$(\nabla^2 + k^2){E_y}^i = i\omega\mu_0 J_i \qquad (C-6)$$

$$(\nabla^2 + k^2){E_y}^s = i\omega\mu_0 J_s \qquad (C-7)$$

where ${E_y}^i$ and ${E_y}^s$ represent the incident and scattered electric fields respectively.

A solution for the first differential equation (C-6) can be described by the electric field due to a line source of current at the surface of a homogeneous half-space (Wait, 1962). While a solution for the second differential equation (C-7) is obtained by multiplying the current density by Green's functions and integrating over the inhomogeneity cross-section. The Green's function can be described as the electric field due to a line current in the earth (Wait, 1962). Electric and magnetic fields are then calculated for E_y in the inhomogeneity while scattering fields are found by integrating over scattering currents at points outside of the inhomogeneity. After normalizing all distances by skin depth, the following integral equation is obtained:

$$E_y(X,Z) = E_y^i(X,Z) - \frac{i(K-1)}{\pi}$$

$$\cdot \int_{X_a-\frac{T}{2}}^{X_a+\frac{T}{2}} \int_{D}^{H} E_y(X',Z') \cdot G(X,Z,X',Z') dX' dZ' \qquad (C-8)$$

where K represents the electrical conductivity contrast between the inhomogeneity and surrounding host formation, G is the conductive half-space Green's function, X_a is the distance between the inhomogeneity center and line source current, and the limits T, D, and H are the skin depth normalized inhomogeneity width, height, and burial depth respectively.

Green's functions for a conductive half-space are used to propagate the effects of the scattered field onto the entire domain. The kernel of the Green's functions for the integral equation can be rewritten as a sum of nonsingular and singular terms. The

singular term is obtained using an analytical expression with modified Bessel functions, while the nonsingular Green's function is calculated numerically using Cosine integration. The inhomogeneity is divided into a body of M cells along the width and N cells along the height (Figure C-1).

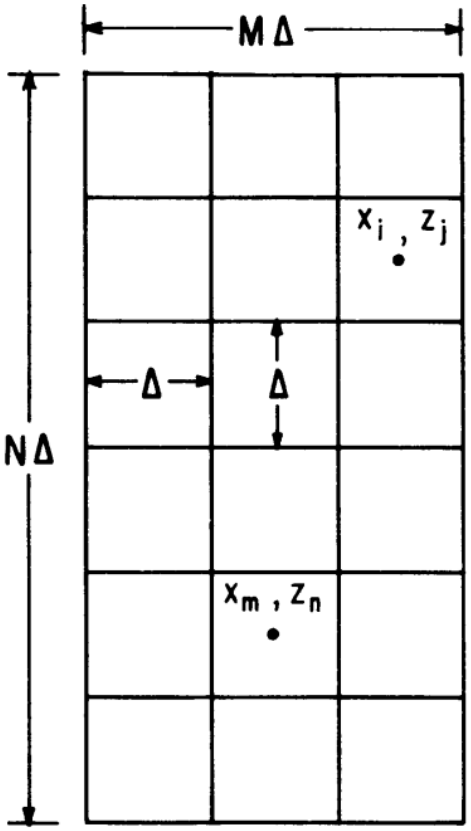

Figure C1 – Division of body into M X N cells for numerical solution. Reprinted from Hohmann, 1971.

By assuming a constant electric field in each cell, Equation A-5 can be solved numerically using the following:

$$E_y^{ij} = E_y^{i\ ij} + \lambda \sum_{mn=1}^{MN} E_y^{mn} G_{mn}^{ij} \qquad (C-9)$$

Letting

$$\lambda = \frac{i(1-K)}{\pi}$$

$$ij = (i-1)N + j$$

$$mn = (m-1)N + n$$

$$MN = M \cdot N$$

where

$$G_{mn}^{ij} = \Delta^2 G_s(X_i - X_m; Z_j + Z_n) + \int_{x_m-\frac{\Delta}{2}}^{x_m+\frac{\Delta}{2}} \int_{Z_n-\frac{\Delta}{2}}^{Z_n+\frac{\Delta}{2}} G_p(X_i - X'; Z_j - Z')dX'dZ'$$

From there, a system of MN linear equations can be obtained to solve for the inhomogeneity electric field. The general matrix equation for the scattered electric field E_y inside the inhomogeneity body becomes:

$$[K] \cdot E_y = -E_y^i \qquad (C-10)$$

where matrix [K] is defined as:

$$K_{mn}^{ij} = \lambda G_{mn}^{ij} - \delta_{mn}^{ij}; \quad \delta_{mn}^{ij} = \begin{cases} 0 \text{ for } ij \neq mn \\ 1 \text{ for } ij = mn \end{cases}$$

Next, the electric field can be found at a point (X, Z) outside the inhomogeneity using the following equation:

$$E_y(X,Z) = E_y^i(X,Z) - \frac{i(K-1)\Delta^2}{\pi} \cdot \sum_{m=1}^{M}\sum_{n=1}^{N} E_y(X_m,Z_n) \cdot \left[G_s(X-X_m;Z+Z_n) + G_p(X-X_m;Z+Z_n)\right] \qquad (C-11)$$

The following expressions are then obtained for the normalized electric and magnetic fields at the surface of the earth:

$$\frac{E_y}{E_y^p} = \frac{E_y^i}{E_y^p} - \frac{i(K-1)\Delta^2}{\omega\mu_0 I} \cdot \sum_{m=1}^{M}\sum_{n=1}^{N} E_y(X_m,Z_n) \cdot \left[{G_s}^E(X-X_m,Z_n) + {G_p}^E(X-X_m,Z_n)\right] \qquad (C-12)$$

$$\frac{H_x}{H_z^p} = \frac{H_x^i}{H_z^p} - 2X\frac{(K-1)\Delta^2}{\omega\mu_0 I} \cdot \sum_{m=1}^{M}\sum_{n=1}^{N} E_y(X_m,Z_n) \cdot \left[{G_s}^{HX}(X-X_m,Z_n) + {G_p}^{HX}(X-X_m,Z_n)\right] \qquad (C-13)$$

$$\frac{H_z}{H_z^p} = \frac{H_z^i}{H_z^p} - 2X\frac{(K-1)\Delta^2}{\omega\mu_0 I} \cdot \sum_{m=1}^{M}\sum_{n=1}^{N} E_y(X_m, Z_n) \cdot \left[{G_s}^{HZ}(X - X_m, Z_n) + {G_p}^{HZ}(X - X_m, Z_n)\right] \quad (C-14)$$

Finally, expressions for calculating the normalized homogeneous-earth fields (C-15 to C-17) and the Green's functions for fields at the surface (C-18 to C-23) can be found in the following equations:

$$\frac{{E_y}^i}{{E_y}^p} = -i\int_0^\infty \frac{1}{g+u}\cos(gX)dg \quad (C-15)$$

$$\frac{{H_x}^i}{{H_z}^p} = -2X\int_0^\infty \frac{g}{g+u}\cos(gX)dg \quad (C-16)$$

$$\frac{{H_z}^i}{{H_z}^p} = -2X\int_0^\infty \frac{g}{g+u}\sin(gX)dg \quad (C-17)$$

$$G_s^E = \int_0^\infty \frac{u-g}{u+g}\frac{e^{-uZ}}{u}\cdot\cos[g(X - X_m)]dg \quad (C-18)$$

$$G_p^E = K_0\left[(1+i)\left((X-X_m)^2 + {Z_n}^2\right)^{1/2}\right] \quad (C-19)$$

$$G_s^{HX} = \int_0^\infty \frac{u-g}{u+g}e^{-uZ_n}\cdot\cos[g(X - X_m)]dg \quad (C-20)$$

$$G_p^{HX} = \frac{(1+i)Z_n}{\left[(X-X_m)^2 + {Z_n}^2\right]^{1/2}}K_1\left[(1+i)\left((X-X_m)^2 + {Z_n}^2\right)^{1/2}\right] \quad (C-21)$$

$$G_s^{HZ} = \int_0^{\infty} \frac{u - g}{u + g}\, e^{-uZ_n} \frac{g}{u} \cdot \sin[g(X - X_m)]dg \qquad (C - 22)$$

$$G_p^{HZ} = \frac{(1 + i)(X - X_m)}{\left[(X - X_m)^2 + {Z_n}^2\right]^{1/2}}\, K_1\left[(1 + i)\left((X - X_m)^2 + {Z_n}^2\right)^{1/2}\right] \qquad (C - 23)$$

For additional details on the development of Equations (C-12 to C-23) see Hohmann (1971) equations 32 - 48.